Forschungszentrum Jülich
in der Helmholtz-Gemeinschaft

Institut für Kernphysik

Threshold Hyperon Production in Proton-Proton Collisions at COSY-11

Tomasz Rożek

Jül-4184

Threshold Hyperon Production in Proton-Proton Collisions at COSY-11

Tomasz Rożek

Berichte des Forschungszentrums Jülich ; 4184
ISSN 0944-2952
Institut für Kernphysik Jül-4184
(Diss., Kattowitz, Schlesische Univ., 2005)

Zu beziehen durch: Forschungszentrum Jülich GmbH · Zentralbibliothek
D-52425 Jülich · Bundesrepublik Deutschland
☎ 02461 61-5220 · Telefax: 02461 61-6103 · e-mail: zb-publikation@fz-juelich.de

Abstract

For the first time the $pp \to nK^+\Sigma^+$ reaction has been measured in the threshold region and the cross section was determined. The measurement was performed at the COSY–11 detection system at two beam momenta $P_{beam} = 2.6$ GeV/c and 2.74 GeV/c, corresponding to excess energies $Q = 13$ MeV and 60 MeV.

COSY–11 is an internal magnetic spectrometer experiment at the **CO**oler **SY**nchrotron and storage ring COSY in Jülich, Germany. It is equipped with scintillator hodoscopes and drift chambers for charged particle detection and a scintillator/lead sandwich detector for neutrons.

Experimentally, the Σ^+ hyperon was identified via the missing mass technique, by detecting the remaining reaction products – K^+ meson and neutron. Extensive background studies in the missing mass spectra have been performed and the possible influence of the the higher partial waves on the detection efficiency discussed.

The investigation on the Σ^+ production is a part of the long ongoing studies of the hyperons production performed by the COSY–11 collaboration. In the previous analysis of the Λ and Σ^0 hyperon production in the $pp \to pK^+\Lambda$ and $pp \to pK^+\Sigma^0$ reactions, respectively, the unexpectedly high cross section ratio $\sigma(\Lambda)/\sigma(\Sigma^0)$ in the close to threshold region was observed. To explain this behavior, various theoretical scenarios were proposed, but although they differ even in the dominant basic reaction mechanism, all more or less reproduce the data. In order to get more information for disentangling the contributing reaction mechanisms, data from an other isospin channel were taken, namely $pp \to nK^+\Sigma^+$.

Within this thesis the method of the measurement and the data analysis is given. The total cross section is presented and the results are discussed in view of available theoretical models.

Streszczenie

Po raz pierwszy w obszarze energii przyprogowych zmierzona została reakcja $pp \to nK^+\Sigma^+$ i wyznaczony jej przekrój czynny. Pomiar ten został przeprowadzony przy użyciu układu detektorów COSY–11 dla dwóch wartości pędu wiązki P_{beam} = 2.6 GeV/c i 2.74 GeV/c, co odpowiada energii nadprogowej Q = 13 MeV i 60 MeV.

COSY–11 jest eksperymentem którego integralną część stanowi zainstalowany na akceleratorze COSY (**CO**oler **SY**nchrotron) w Centrum Badawczym Jülich w Niemczech spektrometr magnetyczny. W skład układu detekcyjnego COSY–11 wchodzą detektory scyntylacyjne i układ komór dryfowych do detekcji cząstek naładowanych oraz detektor neutronów.

W wykonanym eksperymencie hiperony Σ^+ były identyfikowane na gruncie metody masy brakującej poprzez detekcję produktów reakcji: mezonów K^+ i neutronów. W tym celu przeprowadzono intensywną analizę tła w widmach masy brakującej. Zbadano też wpływ wyższych fal parcjalnych na wydajność detekcji.

Pomiary przekroju czynnego dla reakcji $pp \to nK^+\Sigma^+$ są kontynuacją prowadzonego od wielu lat w COSY–11 programu badania przyprogowej produkcji hiperonów. We wcześniejszych pomiarach hiperonów Σ^0 i Λ w reakcjach $pp \to pK^+\Lambda$ i $pp \to pK^+\Sigma^0$ zauważono, że zmierzona warość stosunku przekrojów czynnych $\sigma(\Lambda)/\sigma(\Sigma^0)$ dla energii nad progiem $Q < 15$ MeV jest nieoczekiwanie wysoka. Stworzono kilka modeli teoretycznych próbujących opisać to zachowanie, ale pomimo tego, iż bazują one na zupełnie różnych założeniach co do mechanizmu produkcji hiperonów, wszystkie w podobnym stopniu opisują dane eksperymentalne. Aby rozstrzygnąć, które z mechanizmów produkcji hiperonów rozważanych w modelach teoretycznych, są dominujące, zebrano dane eksperymentalne w innym kanale izospinowym, mianowicie w reakcji $pp \to nK^+\Sigma^+$.

W pracy opisana została metoda pomiaru reakcji $pp \to nK^+\Sigma^+$ oraz analiza zebranych danych. Uzyskane wartości całkowitego przekroju czynnego na reakcję $pp \to nK^+\Sigma^+$ przedyskutowano pod kątem dostępnych przewidywań teoretycznych.

Contents

Chapter 1

Introduction

1.1 Hadron structure

In the history of science many times it was believed that the smallest – *elementary* – indivisible part of matter was found. In 585 BC, Democritus innovate a concept of $\alpha\tau o\mu o\sigma$ (*atomos* = indivisible), but the idea of atom, as it is understand today, was formulated by J. Dalton at the beginning of the XIX century. Later works of Becquerel and Rutherford showed that the atom is not the smallest building-block of matter. In the 20s and 30s of the XXth century the definitions of the proton, the neutron and the electron was established and the concept of neutrinos (Pauli's explanation of the β decay) as well as the Dirac's idea of antimatter appeared. At the beginning of the 40s in the XXth century the list of elementary particles includes the heavy proton and neutron and the light electron and neutrino (and their antiparticles). At this time some scientists were predicting "end of physics", since this set of elementary particles – they were saying – was sufficient to describe the properties of known "micro-world".

During the next decades the fast development of experimental tools of particle physics (e.g. accelerators) resulted in the discovery of many particles which did not fit to the simple model of four elementary building-blocks. The first attempt to classify the increasing number of known particles was based on the fact that different particle decays were conducted by different kind of interactions. **Hadrons** are effected by the strong nuclear force, whereas **leptons** by the weak one. Leptons (i.e. electron, muon, taon and corresponding neutrinos) have no structure, whereas with hadrons it is different. In 1964 Gell-Mann and Zweig [1] proposed that the large variety of hadrons can be explained by the existence of smaller building-blocks called **quarks**. All known hadrons were divided into **baryons** which consist out of three quarks, and **mesons** build out of a quark-antiquark pair. Quarks (three pairs of quarks: *ud, sc, tb* and three pairs of corresponding antiquarks) and leptons (three pairs of leptons: $e\nu_e$, $\mu\nu_\mu$, $\tau\nu_\tau$ and three pairs of corresponding antileptons) form three families (generations) of elementary particles. Experiments performed in 1989 at CERN and SLAC confirm, that there are no more than three generations of fundamental particles. Such conclusion results from investigations of the decay modes of the boson $\mathbf{Z}^0$.

The particles built out of quarks or $q\overline{q}$-pairs can be grouped in multiplets of special symmetry groups. With three light quarks: *up, down* and *strange*, a classification with respect to the representation of the unitary group SU(3), and with all six quarks with

respect to the SU(6) group is possible. The symmetries of these groups are conserved in the strong interaction. In figure 1.1a the fundamental SU(3) representation of three light quarks is presented. In nature quarks are not observed as single objects, but only as a combination of quarks. This phenomenon is called **confinement**. The quarks carry a quantum number called **color**, with three possible orientations: red, green and blue. Only color singlet objects are observed. They can be built out of a quark-antiquark i.e. color-anticolor pair (known as meson) or out of three quarks with different colors (i.e. baryons). The strong interaction between quarks results from the exchange of so-called **color charges** carried by the **gluons**. The theory of the strong interaction (thus color charge exchange) is called **quantum chromodynamics (QCD)**.

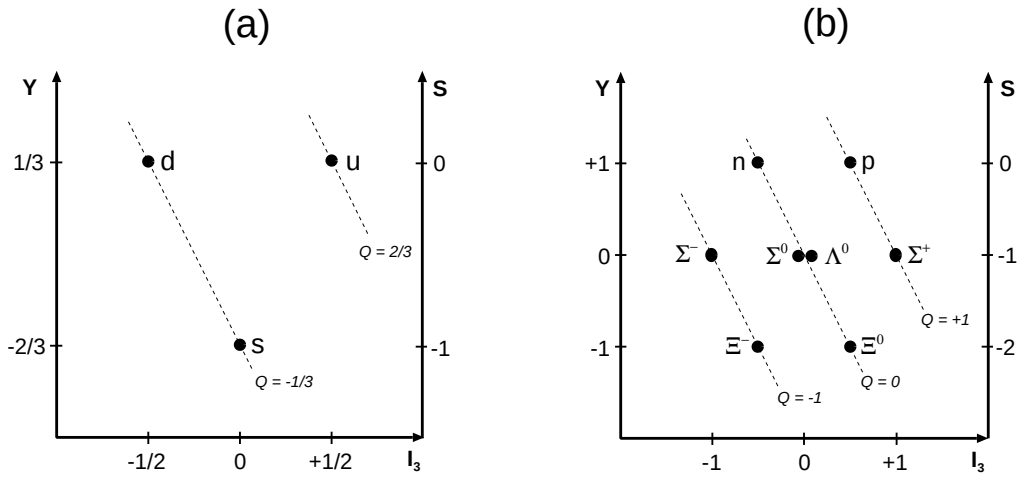

Figure 1.1: (a) SU(3) symmetry group of three light quarks. (b) SU(3) $1/2^+$ multiplet (octet) of baryons made of *u, d, s* quarks. *Y, I_3, S* and *Q* stands for hypercharge (defined as the sum of baryon number and strangeness), third component of isospin, strangeness and charge, respectively.

Baryons and antibaryons have assigned the baryon number $B = 1$ and $B = -1$, respectively. This is a consequence of the fact that baryons are **qqq states** and each quark (antiquark) has a baryon number $B = 1/3$ ($B = -1/3$). Mesons are $\mathbf{q\overline{q}}$ **states** and therefore their baryon number is $B = 0$. The baryon number is conserved in all interactions. Further additive quantum numbers of the three generations of quarks are given in table 1.1.

Table 1.1: Nonzero additive quantum numbers (besides the baryon number) of the quarks, where *Q, I_3, S, B^*, C* and *T* stands for charge, third component of isospin, strangeness, bottomness, charm and topness, respectively [2].

$Q = -1/3e$		$Q = +2/3e$	
d	$I_3 = -1/2$	u	$I_3 = +1/2$
s	$S = -1$	c	$C = +1$
b	$B^* = -1$	t	$T = +1$

In 1947 Rochester and Butler published in *Nature* results of cloud chamber observations with tracks of unknown particles [3]. They were seen relatively often, what suggested the production under strong interaction, but their extremely long life time was suggesting a weak interaction origin. Observed by Rochester and Butler were **kaons** and **hyperons**, which because of their unexpected behavior, were called **strange** particles. Strangeness as an attribute of hadrons is conserved in the strong interaction. As a consequence, particles with nonzero strangeness can not be produced via a strong interaction as a single object, but as a pair, one particle with $S = -1$ is always produced together with a second particle containing an antistrange quark ($S = 1$). This is called the **associated strangeness production**, a type of the reaction investigated within this thesis, namely the $pp \to nK^+\Sigma^+$ reaction, where the K^+ meson is built out of u and $\overline{s}$ quarks (so it has $S = 1$) and the Σ^+ hyperon contains together with two u quarks the s quark and has $S = -1$.

The Σ^+ hyperon is a hadron with baryon number $B = 1$ and spin $J = 1/2$. It is a member of an isospin triplet. The Λ hyperon is a singlet and it is the lightest hyperon. The heaviest hyperons in the baryon octet with spin and parity $J^P = 1/2^+$ are cascades (Ξ), forming an isospin doublet. In figure 1.1b the baryon octet with spin parity $J^P = 1/2^+$ is shown.

1.2 Theoretical motivation

In general, the study of hyperon (Y) production includes several aspects. The hyperon-nucleon interaction can be extracted which is important for a better understanding of the strong interaction including the strange quarks. Due to the lack of hyperon-nucleon data, models describing the YN interaction rely on SU(3) symmetry taking the coupling constants from SU(3) relations. Experimental data of the YN interactions will allow to test the degree of SU(3) symmetry which is very important for questions concerning the mechanism of symmetry breaking and will allow to develop more accurate hyperon-nucleon potentials.

The reaction mechanisms leading to hyperon production have to be clarified for the interpretation of the data. For example Dalitz plot analysis of hyperon production by the TOF collaboration [4] at excess energies above 50 MeV have clearly shown a dominant contribution of nucleon resonance excitations in the Λ production [5].

Another aspect in the investigation of hyperon production due to subsequent decay of an excited nucleon resonance is the extraction of information about the structure of the relevant resonance.

At the experimental facility COSY–11 [6] hyperon production studies are mainly devoted to the YN interaction which is enhanced in near threshold measurements. In a three-body exit channel like $pp \to pK^+\Lambda$ the $p\Lambda$ subsystem can be studied in a range of very low relative energies which is not accessible with conventional scattering experiments.

The production of the Σ^0 and Λ hyperons via the $pp \to pK^+\Sigma^0$ and $pp \to pK^+\Lambda$ reaction was extensively studied at the COSY–11 detection system. Data points, 16 for the Λ and 13 for the Σ^0 channel, were taken in the excess energy range between 0.68 MeV and 59.3 MeV for the Λ hyperon and between 2.8 MeV and 59.1 MeV for Σ^0 [7–9]. In figure 1.2 the excitation functions for these two channels are shown. Additionally, the three

body phase space (PS) (dotted line) and PS plus proton-hyperon final state interaction (pY FSI) are presented.

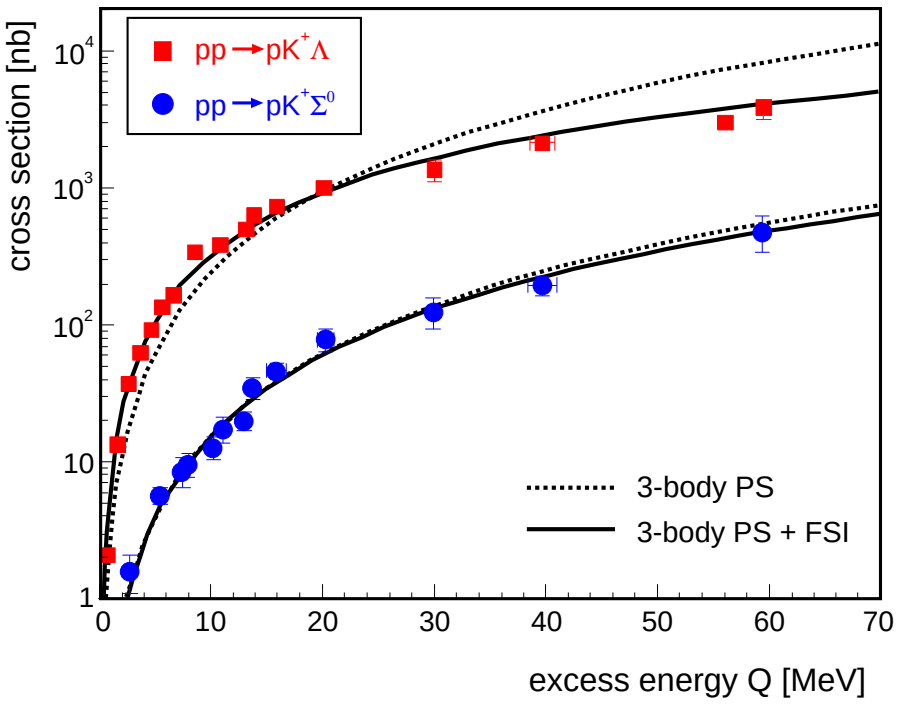

Figure 1.2: Cross section as a function of the excess energy for the $pp \to pK^+\Lambda$ and $pp \to pK^+\Sigma^0$ channels is shown. The data points presented by squares and dots were measured at the COSY–11 detection system [7–9]. The $pp \to pK^+\Lambda$ data point at $Q = 54.6$ MeV was measured at TOF [10].

The $pp \to pK^+\Lambda$ excitation function close to threshold shows a clear deviation from the pure phase space distribution and a proton-hyperon FSI has to be included in order to describe the data [9,11]. On the contrary in the $pp \to pK^+\Sigma^0$ channel the pY FSI seems to be negligible and the pure phase space calculation fairly well follows the data points. This effect is more drastically seen in the cross section ratio $\sigma(pp \to pK^+\Lambda)/\sigma(pp \to pK^+\Sigma^0)$, which below excess energies of ~ 20 MeV was found to be in the order of 28 in contrast to the value of about 2.5 determined for excess energies higher than $Q = 300$ MeV [12] (see figure 1.4). The latter value is in good agreement with the Λ/Σ^0 isospin relation. The question arises if these drastic cross section increase close to threshold is a pure effect of the ΛN FSI or if it is partly due to the reaction mechanisms in the YN channels. To explain the rather unexpected increase of the Λ/Σ^0 cross section ratio in the close-to-threshold region, different scenarios were proposed.

In figure 1.3 Feynman graphs of possible production mechanisms which may contribute to the hyperon production are presented. The simplest direct production mechanism, namely the π- and K-exchange (figure 1.3a and b) must at least be present and its strength can be derived e.g. from experimental data of πN and KN scattering. In figure 1.3c the indirect production via a resonance excitation which is taken into account in the *effective Lagrangian model* [13,14] and the *resonance model* [15] is shown.

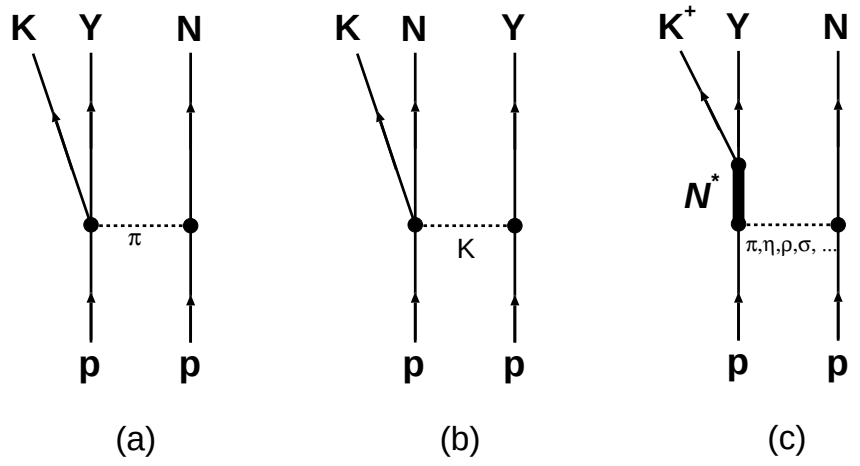

Figure 1.3: Feynman graphs for hyperon ($Y-$) K^+ production in pp collisions. N stands for nucleon, N^* for the resonance state and Y for hyperon ($\Lambda, \Sigma^0, \Sigma^+$). In (a) and (b) the direct production via pion or kaon exchange, respectively, is sketched and in (c) the indirect production via a baryonic resonance excitation resulting from meson exchange.

Incoherent π/K exchange model

Calculations of the strangeness production by pure π- and K-exchange added incoherently have been performed by Sibirtsev et al. [15]. The $\pi N \to YK$ and $KN \to YK$ scattering amplitudes in case of pion and kaon exchange, respectively, were taken from existing data at the higher energy region [12] and were added incoherently. These model calculations show very good agreement with both higher (Q >100 MeV) and lower energy $pp \to pK^+\Lambda$ cross section data. For the $pp \to pK^+\Sigma^0$ channel the *incoherent π/K exchange model* reproduces the higher energy data, but overestimates the cross section in the close-to-threshold region. The ratio of the Λ/Σ^0 cross section is therefore too low close to threshold (curve (1) in figure 1.4. The trend of a ratio increase towards the threshold is reproduced but a factor of about 2 is missing [15].

Resonance model

An improvement in shape is achieved by adding other exchange mesons and resonance excitation as it is done in the *resonance model* (curve (2) in figure 1.4) [13,15–17]. Nonresonant direct contributions like π- or K-exchange were not included in this model because it turned out that they are rather small. Here the π, η and ρ meson exchange with the excitation of intermediate baryonic resonances $N(1710)$, $N(1720)$ and $\Delta(1920)$ are taken into account in both $pp \to pK^+\Lambda$ and $pp \to pK^+\Sigma^0$ reactions and additionally the $N(1650)$ resonance in the Λ production case. In this *resonance model* the close-to-threshold region of the experimental Λ/Σ^0 cross section ratio seems to be better reproduced than higher energy data ($Q \geq 10$ MeV), although for excess energies $Q \geq 100$ MeV model predictions are in good agreement with the ratio of about 3 observed for the high energy data [12]. It should be stressed that the parameters in these calculations were fixed on the basis of

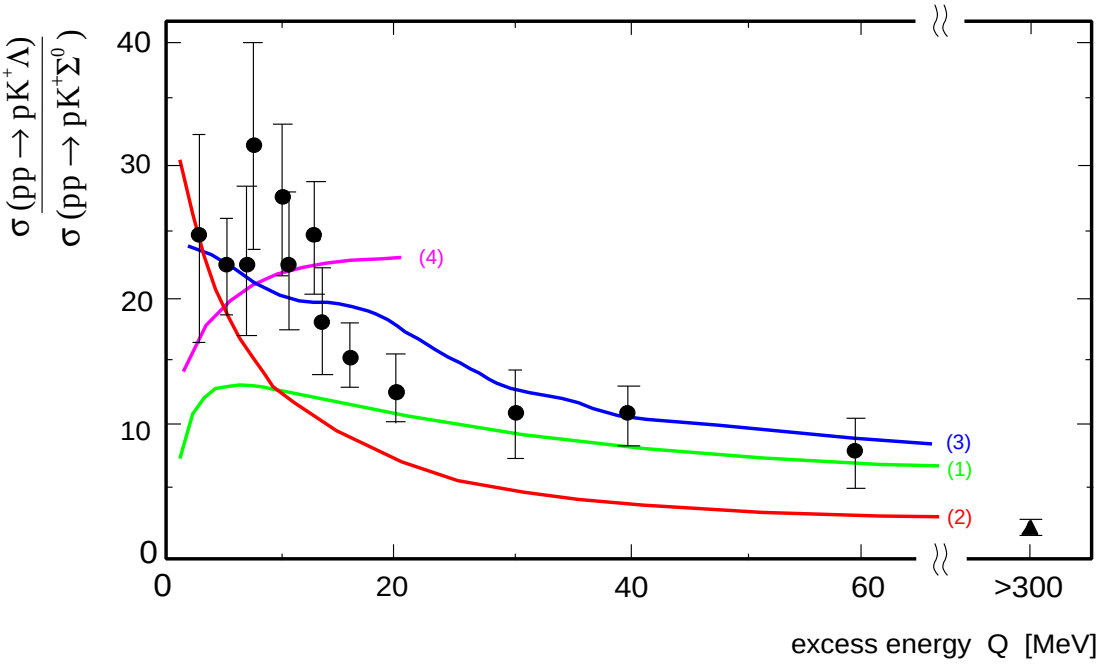

Figure 1.4: Cross section ratio for Σ^0 and Λ production in the threshold region. High energy data point comes from [12]. The data are compared to different models descriptions. For details see text.

high energy data, before the close-to-threshold Λ and Σ^0 data were available. Therefore the model predictions were not adjusted or normalized to the low energy data points. The excitation function of the $pp \to pK^+\Sigma^0$ reaction channel is reproduced very well by the model predictions, but the cross section for the $pp \to pK^+\Lambda$ channel in the excess energy region $Q \leq 100$ MeV is slightly underestimated. With the same parameters (i.e. those for the $pp \to pK^+\Lambda$ or $pp \to pK^+\Sigma^0$ reactions calculations), the *resonance model*, however, can not reproduce data with a neutron in the entrance channel (like $pn \to p\Lambda K^0$ or $pn \to p\Sigma^- K^+$). It results in an overestimation of the calculated cross section by a factor from 2 to 7 [17]. The same behavior in the $pn \to p\Lambda K^0$ reaction channel was observed in [11], where the calculated cross section for this reaction differs by a factor from 5 to 10.

Effective Lagrangian model

Other calculations by Shyam et al. [13, 14] based on the *effective Lagrangian model* for the strangeness production include meson exchanges (π, ρ, σ and ω) with the intermediate excitation of resonances: $N(1650)$, $N(1710)$ and $N(1720)$. In contrast to the *resonance model*, the $N(1650)$ resonance was also taken into the account in the calculations for the $\Sigma^0 K^+$ production. The coupling constants were determined by fitting available data of the $\pi^+ p \to \Sigma^+ K^+$, $\pi^- p \to \Sigma^0 K^0$ and $\pi^- p \to \Sigma^- K^+$ reaction channels. The contribution of the $N(1650)$ resonance to the $pp \to pK^+\Sigma^0$ production is by an order of magnitude higher than contributions of the higher baryon resonances (contributions of $N(1710)$ and $N(1720)$ are comparable). It is not the case in the $pp \to pK^+\Lambda$ reaction, where the

considered resonances have comparable contributions [14]. Concerning the exchange of mesons, the largest contribution is due to pion exchange. The contribution of σ meson exchange is about one order of magnitude smaller and for both ω and ρ mesons exchange it is negligible [13,14]. This coherent sum of resonant states and meson exchange processes describes the available experimental data points for the $pp \to pK^+\Lambda$ and $pp \to pK^+\Sigma^0$ channels very well. The cross section ratio calculated from *effective Lagrangian model* is depicted by the curve (3) in figure 1.4.

Jülich meson exchange model

The Jülich theory group has performed calculations for the $pp \to pK^+\Lambda$ as well as for the $pp \to pK^+\Sigma^0$ reaction channels including π- and K-exchange [18, 19]. In their approach the interaction between the hyperons (Λ, Σ) and the nucleon is described by a microscopic ($\Lambda N - \Sigma N$) coupled channel model [20]. A suppression of the Σ production due to the coupling to the Λ channel proposed in Ref. [8] as a possible explanation for this large cross section ratio at threshold is excluded from this model calculations. The $\Lambda\Sigma$ coupling is by far not sufficient to result in such drastic Σ suppression. Model predictions show that the interference between π- and K-exchange amplitudes could be responsible for this effect. The Λ production is dominated by the K-exchange and therefore the influence due to an interference between π- and K-exchange is negligible in this hyperon channel. On the other hand, the π-exchange gives a comparable contribution to the cross section of the Σ^0 production. An interference between π- and K-exchange amplitudes act very differently on the two channels. When adding the amplitudes coherently for the two extreme cases with a relative phase of 0° or 180°, the cross section for the Λ production does not change significantly, but the cross section for the Σ^0 production is much lower for the destructive interference. Within the *Jülich meson exchange model* the large cross section ratio can be described by a destructive interference of the π- and K-exchange amplitudes. Absolute cross section normalization factors for the Λ and Σ^0 channel of 0.25 and 0.3, respectively, are needed and can be explained by the initial state interaction (ISI) [18, 21] which was not taken into account in the *Jülich meson exchange model*. Such a normalization is not necessary for the Λ/Σ^0 cross section ratio predictions since the threshold energies for the Λ and Σ^0 production via the considered reaction channels are very close to each other and the effect of ISI is very similar. In figure 1.4 the *Jülich meson exchange model* is shown by curve (4). For excess energies above 20 MeV the model is not valid, why the curve stops at 20 MeV but qualitatively the cross section ratio given by the model stays at a nearly constant level. This might be the effect of the strongly increasing contribution of higher partial waves [22].

Although the various descriptions of the cross section ratio differ even in the dominant basic reaction mechanisms, all reproduce the trend of an increase in the Λ/Σ^0 cross section ratio in the threshold region (see figure 1.4). The present data are not sufficient to definitely exclude any of the sugested reaction models. Further data are needed where especially other isospin channels should allow to extract information about the production mechanisms. For example data on the reaction channel $pp \to nK^+\Sigma^+$ would serve as a further step to disentangle the contributing reaction mechanisms in the near threshold hyperon production. With the installation of a neutron detector, the reaction channel $pp \to nK^+\Sigma^+$ became accessible at the COSY–11 installation.

This work extends the experimental information about various NK^+Y reaction channels observed in proton-proton collisions near threshold. For the first time the absolute cross section for the reaction $pp \to nK^+\Sigma^+$ at the two excess energies $Q = 13$ MeV and $Q = 60$ MeV were determined. These data are compared with previously measured reactions $pp \to pK^+\Lambda$ (Σ^0) at the COSY–11 installation and with predictions of theoretical models, as well.

This thesis consists of three main parts. Besides the theoretical motivation which is given in *Chapter 1*, in the experimental section (*Chapter 2*) the COSY–11 detection system, off-line events selection, and data analysis are described. In *Chapter 3*, the experimental results obtained within this thesis are discussed and compared with available theoretical predictions.

Chapter 2

Experiment

2.1 COSY accelerator

The COoler SYnchrotron and storage ring [23] COSY operates at the Institute for Nuclear Physics (IKP) [24] of the Forschungszentrum Jülich (FZJ) in Germany [25]. COSY delivers polarized and unpolarized protons and deuterons in the momentum range from 0.3 GeV/c to 3.65 GeV/c. The 180 meters long acceleration pipe of the COSY accelerator is filled with up to 10^{11} particles. The beam particles with the demanded energy – depending on the experimental needs – are available for internal and external experiments (see figure 2.1).

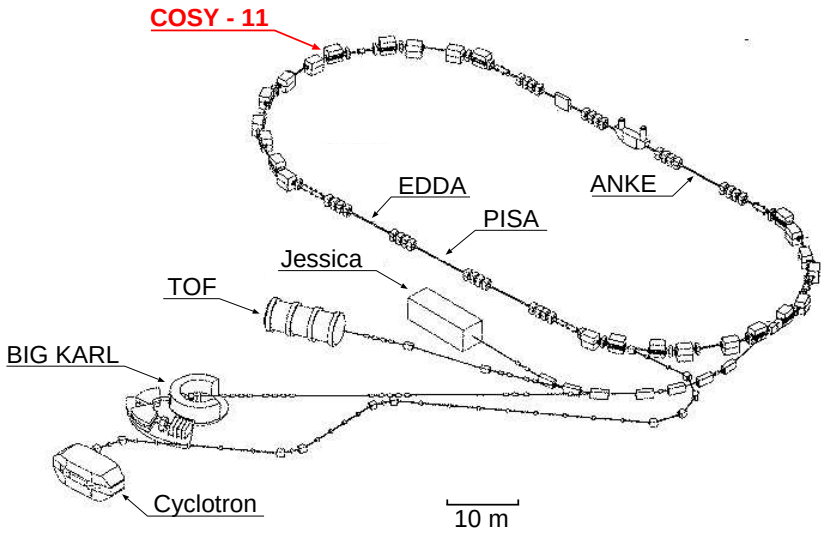

Figure 2.1: The COSY accelerator complex with external (BIG KARL, TOF, Jessica) and internal (EDDA, ANKE, PISA and COSY–11) experiments.

The measurement of Σ^+ hyperon production via the $pp \to nK^+\Sigma^+$ reaction with the two proton beam momenta (P_{beam} = 2.6 GeV/c and P_{beam} = 2.74 GeV/c corresponding to excess energies of 13 MeV and 60 MeV, respectively) was performed in March 2003 [26]. The experiment lasted ten days whereof the lower energy data were taken for more than six days.

2.2 COSY–11 detection system

The COSY–11 detection system makes use of one of the regular COSY dipoles as a magnetic spectrometer in order to separate reaction products from the circulating beam [27]. In figure 2.2 the COSY–11 experimental set-up is shown. Only the detectors relevant for this work are marked, and in the following subsections these detectors are described in more details.

The Σ^+ hyperon was identified via the missing mass technique by detecting the remaining reaction products, i.e. the K^+ and the neutron. Assuming a hit in the neutron detector (see section 2.2.5) being due to a neutron, the four-vector of the neutron is given by the measured direction and velocity of the neutron and its known mass. Kaon identification was performed via its invariant mass determined from the measured velocity and its reconstructed momentum. To get the velocity of a second particle (while a neutron is the first one) the time of flight between S8 and S1 scintillators is needed (see subsection 2.2.4). The momentum vector of the K^+ meson was established by tracking the K^+ trajectory reconstructed from signals registered in the drift chambers DC1 and DC2 (see subsection 2.2.3) through the known magnetic field back to the target point.

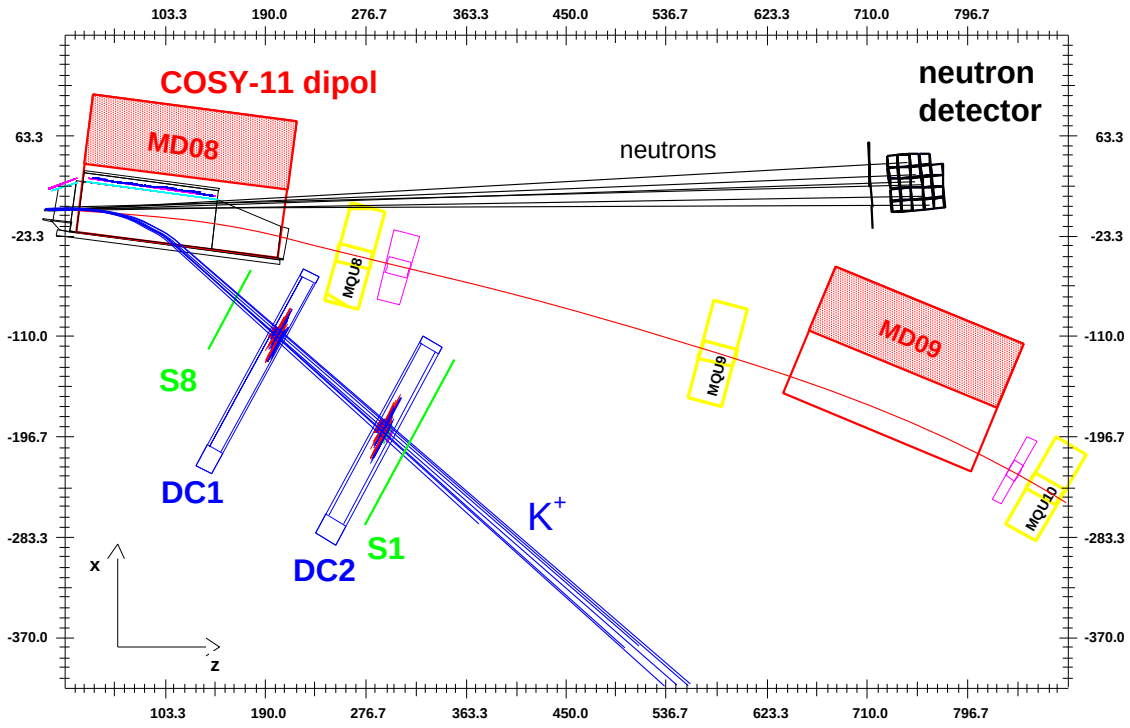

Figure 2.2: COSY–11 detection se-tup [27] with the superimposed tracks of kaons and neutrons from the $pp \to nK^+\Sigma^+$ reaction.

2.2.1 Cluster target

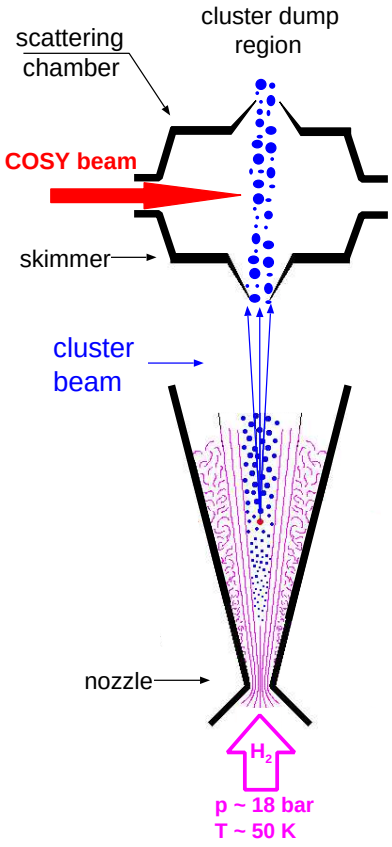

Figure 2.3: Schematic view of the internal COSY–11 cluster target [28].

COSY–11 is an internal experiment and this fact requires special features for the target. It must be thin enough in order not to decrease the beam intensity significantly, but it must be thick enough to provide the reasonable number of interactions in the target region. These conditions are fulfilled by the cluster target where pre-cooled gas is pressed through a Laval nozzle. By expansion in the nozzle the gas is further cooled (so called adiabatic cooling) and therefore clusters of frozen molecules (up to 10^6 hydrogen molecules per cluster under the working conditions) are created [27]. The skimmer and two further collimators cut out of the cluster flow the required homogeneous target beam which enters the COSY beam pipe. The clusters travel through the scattering chamber as a jets with a diameter of about 9 mm and do not very much affect the COSY vacuum. A typical cluster density in the interaction region is about 10^{14} atoms/cm^3 [27]. This value is not fixed and the density of the target can be easily reduced by changing the nozzle temperature or the gas input pressure [29]. Besides hydrogen also deuterium can be used as an input gas in the COSY–11 cluster target system. With the proton spectator detector it provides the possibility to use neutrons as a target in quasi-free scattering experiments [30].

2.2.2 Silicon detectors

The two silicon detecting systems in the COSY–11 detection set-up are built from the same type elements containing four separate pads each [27]. In figure 2.4 the position of these detectors and their internal structure is shown.

The silicon pad detector (called *dipole silicon detector*) which is positioned in the dipole gap is used to detect negatively charged mesons, i.e. π^- and K^-, bent in the magnetic field into the inner part of the dipole. It consists of 180 elements with 4 pads each, divided into three rows. Each single pad has dimensions of 22.0 x 4.5 x 0.28 mm^3 [27]. The second silicon detector (*S4*) was built in order to detect the recoil protons from *pp* elastic scattering (see also subsection 2.4.4). It consists of 36 elements with 4 pads each, divided into three rows (see also figure 2.38). All together in the COSY–11 detection set-up there are 864 silicon pads.

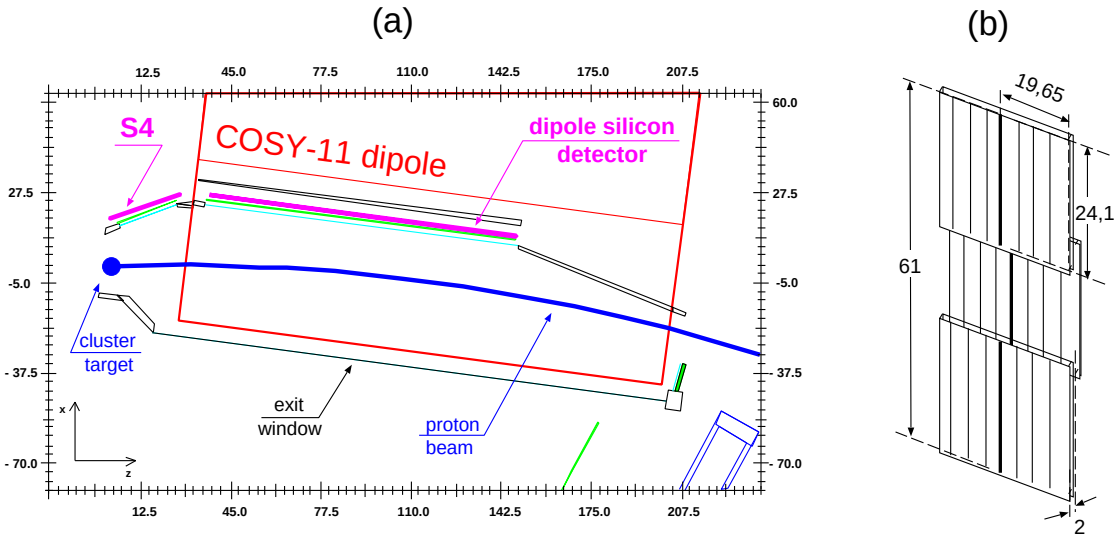

Figure 2.4: The COSY–11 dipole magnet with two silicon pad detectors (a) and sketch of their internal structure with three overlapping rows (b), (dimensions are given in millimeters).

2.2.3 Drift chambers

Trajectories of positively charged particles produced in the target point are registered by two drift chambers DC1 and DC2 containing 6 and 8 detection planes [27], respectively. The distance between these chambers is 70 cm, and their active areas are: 1680 mm (width) and 433 mm (height).

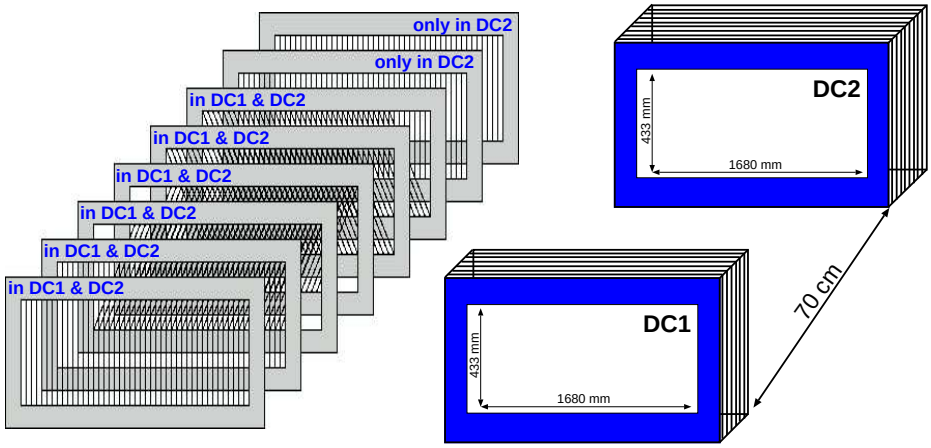

Figure 2.5: Sketch of two drift chambers and the orientation of their wires.

The DC1 contains six detection planes. The first two planes have vertically oriented wires, the next two have wires inclined by $+31^\circ$ and the last two have wires inclined by -31°. The second chamber (DC2) has two additional planes with vertical wires. This geometry allows to measure with high accuracy the coordinates of particles passing through the drift chambers.

A single cell of the drift chamber planes is 40 mm wide and 10 mm thick. It consists of two rows of cathode wires (there are 20 wires in each row) and two field wires in between with the voltage -2000 V and one sense wires with the voltage $+2200$ V. Charged particles traversing between the cathode wires invoke an ionization of the gas mixture (50 % of argon and 50 % of ethane at atmospheric pressure). The positively charged ions drift to the field wires and cathode wires with negative potential, while free electrons drift to the sense wire with the positive potential. The measurement of the smallest drift time of free electrons allows the determination of the distance between the sense wire and the particle track. Each of the drift planes gives the coordinates of the particle crossing point. To resolve the left-right ambiguity the neighboring planes of each pair are shifted by half of the cell size. The reconstruction procedure fits a straight line to those points, which is assumed to be the particle trajectory. For this the relation between the drift time and the drift path is needed, which, in turn, requires the time and space calibration of the DC1 and DC2 system. The detailed description of the necessary procedures can be found in Ref. [31].

When the particle trajectory is reconstructed, it is traced back to the target point through the known magnetic field in the dipole. Thereby, it gives the information about the momentum of the reconstructed particle. For a sufficient accuracy of the momentum determination, good position resolution is needed. In the optimal case, i.e. when 1 GeV/c proton trajectories are perpendicular to the drift chamber planes, the position resolution amounts to about 100 μm [27] in the x direction. In the data analysis, however, not only mono energetic protons but also pions and kaons with different momenta are used for the calibration procedure. Their momenta are in majority below 1 GeV/c. Since small angle scattering effects are rising when the momentum of a charged particle traversing a medium is decreasing [2] the typical value of the resolution in x direction for the COSY–11 drift chambers is about 250 μm [31]. In the experiment described in this work, mainly kaons were selected for the calibration procedure. Their energy is relatively low, and this cause an additional deterioration of the position resolution. The average space resolution in x is about 350 μm for the present experiment [1].

The efficiency of the track reconstruction is very important for the proper interpretation of the data. The reconstruction efficiency for the set of two drift chambers (with signals in all 14 planes) is very close to 100 % [27]. Nevertheless the track reconstruction is also possible even if not all planes give a signal [27]. For example simulation studies show that without two planes, the reconstruction efficiency is close to 90 %, and without four layers it is around 60 % [33].

[1] The influence of the temperature and humidity oscillations of the air surrounding the drift chambers on the drift time is described in [32]. In order to avoid the drift velocity fluctuation, the space-time calibration was done for each data file separately.

2.2.4 Scintillators

When a charged particle interacts with matter its electrons are raised to excited levels directly or by secondary interactions of primary electrons. In scintillation materials the de-excitation energy is released in a small part as light [2]. This light can be converted into an electric charge by a photomultiplier. The signal of the photomultiplier is proportional to the energy deposition in the scintillator and gives the time signal of the scintillator which is important for the particle velocity determination.

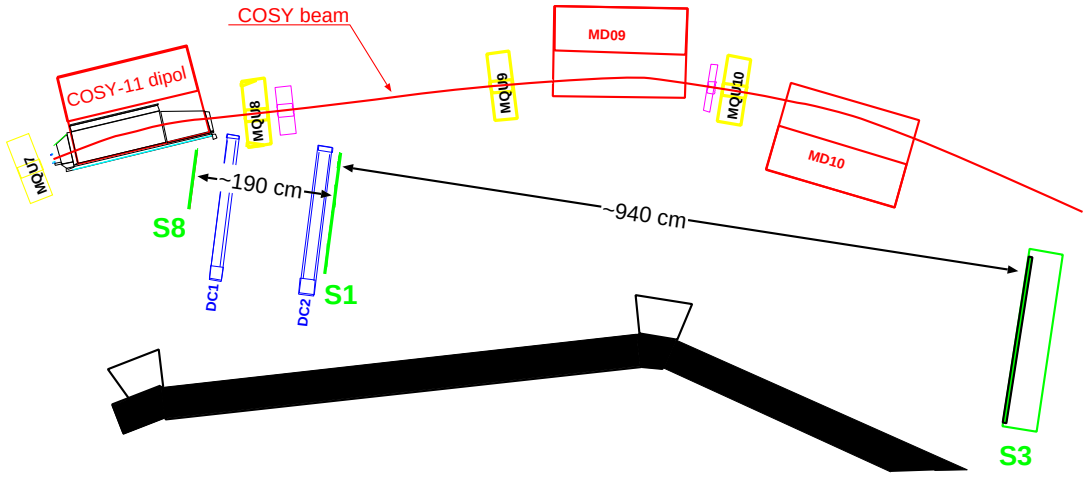

Figure 2.6: The COSY–11 detection set-up. The three scintillation hodoscopes (S8, S1 and S3) are marked in green and the distances between them are given.

Since in the COSY–11 set-up scintillator detectors are mainly used for fast timing measurements, a good time resolution of the scintillation material is needed. For all scintillators at COSY–11, which is dedicated for fast counting purpose [34] Bicron BC 404 plastic scintillator material is used [27, 35].

In reactions with at least one proton in the exit channel, its velocity is measured between the S1 and the S3 hodoscopes (START and STOP signal, respectively). In the present experiment, however, the START signal is given by the S8 scintillator, installed very close to the COSY–11 dipole magnet, and the STOP signal is provided by the S1 hodoscope (see figure 2.6). The S3 hodoscope couldn't be used, because a large fraction of kaons decay before they reach the S3 detector. For K^+ mesons the $c\tau$ value is given to be $c\tau = 3.713$ m [2], which means that e.g. for a velocity ~ 0.8 c (relevant for the studied reaction) 90 % of the particles would decay before traversing a distance of 10 m. The path length from the target point to the S3 hodoscope is about 14 m.

The S1 (S8) hodoscope consists of sixteen (four) scintillation modules read out on both sides by photomultipliers. The S8 and S1 modules are arranged vertically with an overlap of about 1 mm. The scintillation material as well as photomultipliers in case of S8 and S1 detector are the same [27]. The construction of the S3 scintillation wall differs significantly from the arrangement of the rest of COSY–11 scintillation detectors. More details about this detector can be found in [27, 31, 36].

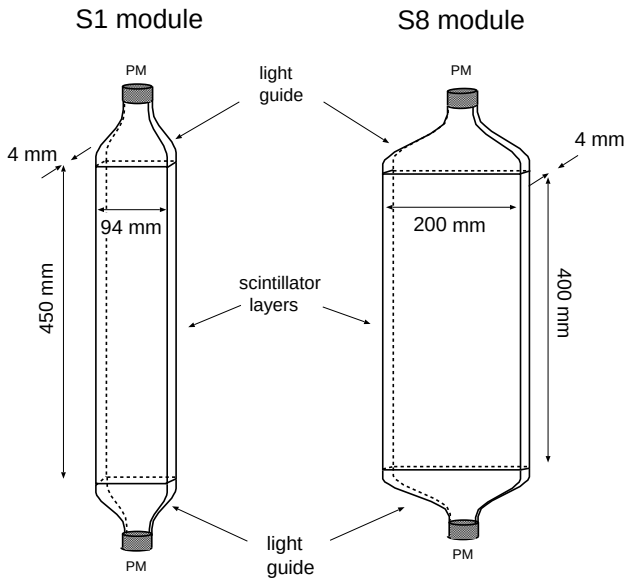

Figure 2.7: The sketch of the single S1 detector scintillation module and S8 detector module. The plexiglass light guides allow to collect and guide light produced in the scintillation layers, onto the photocathode of a photomultiplier (denoted as PM).

2.2.5 Neutron detector

Detection of neutral particles is one of the most challenging tasks in experimental physics. A direct detection of a neutron is impossible because they do not interact electromagnetically and therefore do not produce ionization events in the detector material. That is why neutrons must be detected through hadronic interactions which result in charged particles or electromagnetic radiation which subsequently can be detected by their electromagnetic interaction in the radiation detectors. This "indirect detection" in case of neutrons strongly depends on their energy. *Slow (thermal) neutrons* with kinetic energies of up to some eV are detected via nuclear capture reactions. Since the cross section of these reactions decrease with increasing neutron energy very radically [34], for *intermediate energy neutrons* (namely neutrons with energy in the order of keV) the nuclear conversion detector is inefficient. In this case the slow neutrons detector can be surrounded by a hydrogen rich material acting as a moderator, which slows down neutrons (so-called thermalization process) to the energy range where the neutron capture reaction cross section is high enough [34]. Using so-called loaded scintillators or moderators for *high energy neutrons* detection is unpractical. For an efficient detection one would need a total thickness of several nuclear interaction lengths (the mean free path of a particle before undergoing an interaction) which amounts to about 80 cm for the high energy neutrons in the plastic scintillation material [37]. Therefore for an efficient detection and at the same time rather compact installation, a high density of interaction centers is needed. For particles ranging from a few MeV up to the GeV kinetic energy region different kinds of calorimeters are used. Most of them consist of *passive*, i.e. scintillator plates, interlayed by *active* interaction material plates. The most commonly used active converter materials are: iron, uranium and lead [38].

In a simple explanation, a calorimeter is a block of matter which stops the primary particles by causing interactions with the medium, where secondary fast particles are generated, which subsequently generates again new particles in a cascade or *shower* [39]. The energy of the shower particles is reduced and for sufficiently large detector volumes the whole energy could be absorbed. Depending on the type of the primary particle, there are two kind of cascades. High energy neutrons generate a *hadronic shower* producing typically, i.e. via hadronic interactions, pions and kaons. Photons or electrons initiate an *electromagnetic cascade* generating electrons and/or photons with lower energy than the primary particle. The main differences between electromagnetic and hadronic showers are:

- the mean free path between collisions is shorter in an electromagnetic cascade than in a hadronic one,
- the mean number of particles produced in one collision is higher in an electromagnetic shower than in a hadronic one,
- the minimum particle energy in the shower (after which the shower development stops) for the hadronic cascade amounts roughly to 140 MeV, which is the mass of the lightest hadron, namely pion. In case of an electromagnetic cascade the process stops shortly after the energy of "higher generation" particles is lower than the critical energy $E_c \approx 800$ MeV$/(Z + 1.2)$, where Z is the atomic number. For a lead converter with $Z = 82$ the critical energy is: $E_c \approx 9.6$ MeV [2],
- the energy resolution is about two times better for electromagnetic cascade than for hadronic one [40, 41] (compared at the same kinetic energy).

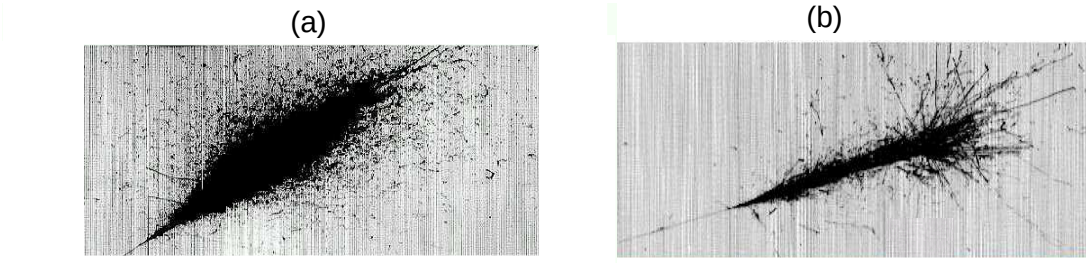

Figure 2.8: Electromagnetic (a) and hadronic (b) showers observed in the ICARUS LAr drift chamber with cosmic rays. Given pictures are $\sim$ 180 cm wide and $\sim$ 75 cm high.

If the detector is designed to measure the total energy of a primary particle (i.e. as a calorimeter), a sufficient thickness (dependent on the energy of the primary particle) of the detector and detailed energy resolution Monte Carlo simulation studies are necessary. However, as long as the detector is in a significant distance from the target, the particle energy determination is easier achievable in a time of flight measurement. In this case the full energy of a neutron does not have to be deposited in the detector and only the first generated signal in the scintillator is needed. Therefore the detector can be much smaller and the analysis is less complicated. At COSY–11 the energy of the neutron is determined from the time of flight – assuming a hit in the detector being due to a neutron. A segmentation of the detector allows to determine the hit position of the neutron within the module size and the *sandwich* structure classify it as a *sampling calorimeter*. In such a device the function of energy degradation and energy measurement are separated in

alternating layers of different substances. This gives a freedom in the optimization of detector (passive absorber material and dimensions as well as the readout method) for specific experimental needs.

In 1996, for first test, a prototype of the neutron detector (consisting of two modules) was included into the COSY–11 detection set-up [42]. In 1997 the neutron detector was extended to 12 and in 2001 to 24 modules [43]. During these years the position as well as the arrangement of the detector modules were changed [44] according to the experimental needs. In the set-up used for the Σ^+ production studies the first row of modules (front) of the neutron detector is positioned at a distance of 7.36 m from the target and consists of 24 modules (see figure 2.2). Each module is built of eleven lead plates interlayed by eleven scintillator plates with dimensions of 270 x 90 x 4 mm^3 (see figure 2.9). The detector covers the neutron laboratory angular range of $\pm$ 1.84° in x and $\pm$ 1.1° in y direction.

In the current arrangement the modules are coupled at both ends to plexiglass light guides, which reduce smoothly the rectangular cross section at the detector side to a circle. This shape allows to collect and guide light produced in the scintillation layers, onto a round photo cathode of a photomultiplier. There, the light pulse is converted into an electric signal, which is provided to ADC and TDC converters.

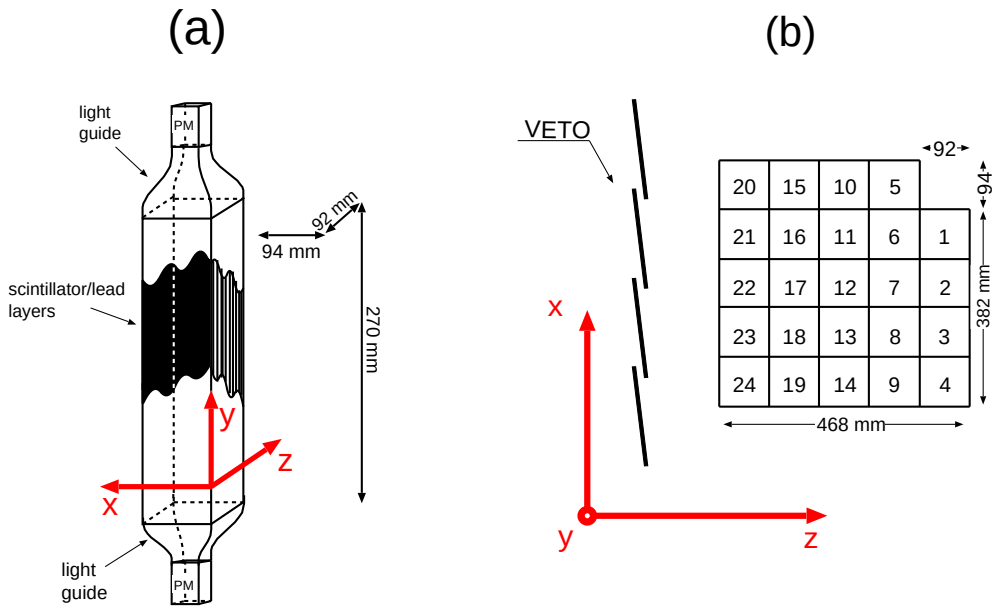

Figure 2.9: In (a) a single module of the neutron detector is depicted. The *passive* e.g. scintillator plates (white) interlayed by *active* lead plates (black) are sketched. In (b) the full COSY–11 neutron detector arrangement with four VETO scintillation modules is shown. Direction of the z axis is the direction of neutrons.

For energy and momentum determination of the neutrons the precise knowledge of the moment of the registration of the light signal in the photomultiplier is crucial. The global timing for the neutron detector is taken as the difference between the time of the reaction and the shortest time in the neutron detector (given by the first module which fired). The distribution of the modules with the first signal, i.e. where the γ or neutron conversion happened is shown in figure 2.10. For γs it occurs mostly in the first row

which is consistent with the expectation from the radiation length of 0.56 cm for γs in lead [2]. For neutrons, the distribution is more homogeneous with a maximum in the central part of the neutron detector. For charged particles (figure 2.10c) the maximum of the distribution appears on the lower left part of the detector because the detector is located on the left side of the beam pipe (compare with figure 2.2).

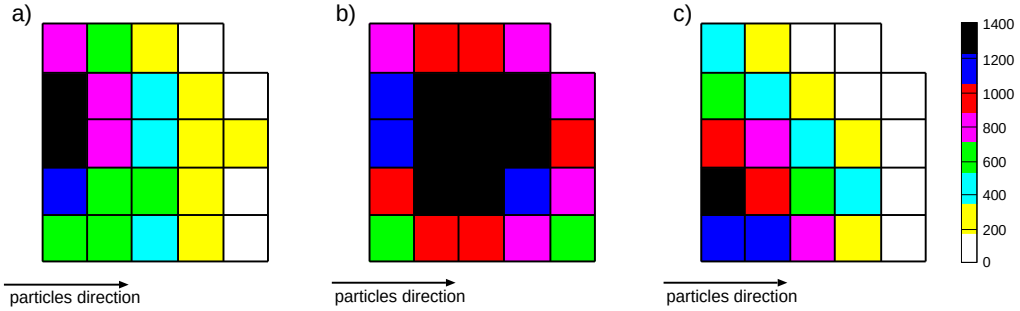

Figure 2.10: Experimental conversion probability distribution in the neutron detector for γs (a), neutrons (b) and charged particles (c). The module where the conversion happens was defined by the first signal.

Besides neutrons, the VETO detector positioned in front of the neutral particle system (see figure 2.9) does not discriminate γs which in a great number fly in the direction of the neutron detector. Although the misidentification of γ as a neutron is mostly removed by the cut on the time of flight (see section 2.4.2), the primary particle in the COSY–11 neutron detector can be a γ and therefore both electromagnetic and hadronic showers can be generated.

The primary neutron kinetic energy from $pp \to nK^+\Sigma^+$ reaction is in the range from $\sim$180 MeV to $\sim$740 MeV for higher energy data set (and from $\sim$260 to $\sim$520 MeV for the lower one). Since the total energy of the neutrons is determined via the time measurement, a good time resolution is needed and the time spectrum of the detector has to be fully understood. The calculated neutron energy resolution depends on the time of flight accuracy and the precision of the neutron distance measurement. The energy E can be determined as follows:

$$E = m_n\sqrt{1+\beta^2\cdot\gamma^2}, \qquad \gamma = \frac{1}{\sqrt{1-\beta^2}} \qquad \text{and} \qquad \beta = \frac{l_n}{T_n}, \tag{2.1}$$

where m_n is the mass of a neutron and l_n is the distance between target and the conversion point of the neutron in the detector material. The neutron time of flight T_n is obtained with respect to the reconstructed time in the target by backtracking positively charged particles to the interaction point through the known magnetic field. Therefore the inaccuracy of T_n stems from: *i*) the neutron detector time resolution (t_N) and *ii*) time determination of the interaction (t_S). The neutron detector time resolution was evaluated to be 0.4 ns [45], (see also the section 2.3.2) which is in the order of the time needed for light to travel in the scintillator a distance of the size of a single module (92 mm). The accuracy of time determination in the target from the kaon track was determined to be about 0.22 ns [46]. The neutron path is defined as the difference between the position of

the interaction point and the center of the first module which gave a signal. The accuracy of this measurement amounts, with good approximation, to the half size of the module which is about 4.5 cm.

In contrast to *energy hermetic* calorimeters where the energy resolution improves with increasing energy [38,41,47], in detectors where the neutron energy is calculated from time of flight the resolution gets worse with the neutron energy increase [37] (see figure 2.11). For example in the LAND (Large Area Neutron Detector) neutron detector which was built at the SIS facility of GSI in Darmstadt, the energy resolution for neutrons with kinetic energies $E \leq 1GeV$ is in the order of 5 % [37]. For the COSY–11 neutron detector the energy resolution for neutrons within this range amounts to be about 8 %. This agreement is very good taking into account the more than twice longer neutron path in LAND ($\sim$15 m) and the much better position determination, since in the LAND calorimeter the modules in two neighboring rows are perpendicular to each other. For the range of interest in studies of the $pp \rightarrow nK^+\Sigma^+$ reaction a resolution of about 2.2 % for lower and about 4.5 % for higher data set is expected (see figure 2.11).

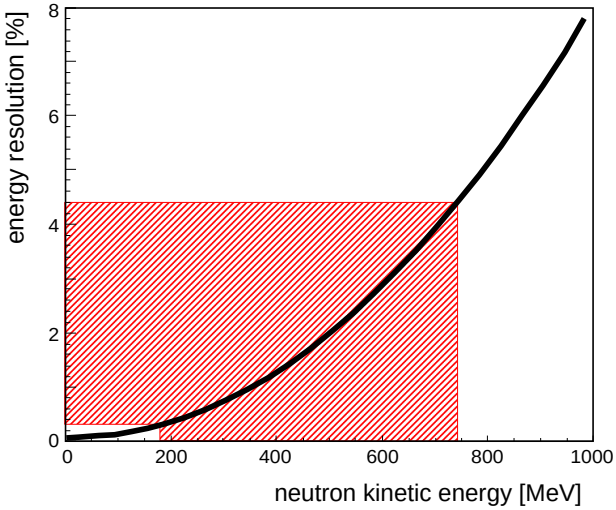

Figure 2.11: The energy resolution for the COSY–11 neutron detector. The kinetic energy range of neutrons from $pp \rightarrow nK^+\Sigma^+$ reaction at the excess energy of Q= 60 MeV as well as the expected energy calculation accuracy is hatched.

The efficiency of the COSY–11 neutron detector was determined from Monte Carlo studies. In the simulation program based on the GEANT 3 code [48] the GEANT-FLUKA subroutine is used for the hadronic interactions [49]. The GEANT-FLUKA enables studies of hadronic as well as electromagnetic cascades induced in matter by particles with a wide range of energy. Hadronic inelastic interactions are simulated by three different event generators depending on the particle energy [49]. The range between 0.02 GeV and 3.5 GeV is described by the pre-equilibrium-cascade model PEANUT (PreEquilibrium Approach to NUclear Thermalization) [50, 51].

For the present case neutrons with a well defined energy were generated in the direction of the detector and their response was analyzed in the usual procedure. The comparison between the known number of generated events and the reconstructed one gave the information about the efficiency of the COSY–11 neutron detector (see figure 2.12). The distribution (a) shows the ideal efficiency of the stand-alone COSY–11 neutron detector. Neutrons were generated in a vacuum up to the direction of the middle part of the detector. Between the generation point and the first row of the detector there were no

medias - including the VETO detector. The distribution (b) in figure 2.12 shows the detection efficiency of neutrons in the realistic COSY–11 detection system. Neutrons were generated in vacuum in the target point and were tracked by the simulation program through the vacuum chamber inside the COSY–11 dipole. They passed through the iron wall of the vacuum chamber and were tracked through the air for the distance of more than 6 m. They passed through the VETO detector and reached the neutron detector. Distances, materials and dimensions of the medias were identical to those of the existing ones. Neutrons from the $pp \to nK^+\Sigma^+$ reaction have kinetic energies from about 270 MeV to 515 MeV (180 MeV to 734 MeV) for the beam momentum $P_{beam} = 2.6$ GeV/c ($P_{beam} = 2.74$ GeV/c). For these cases the efficiency for the COSY–11 neutron detector is in the range of 50 % to 60 %. This is in agreement with the calculated efficiency for the depth of 40 cm "iron loaded" LAND calorimeter [37], and with those obtained for other calorimeters [47, 52, 53].

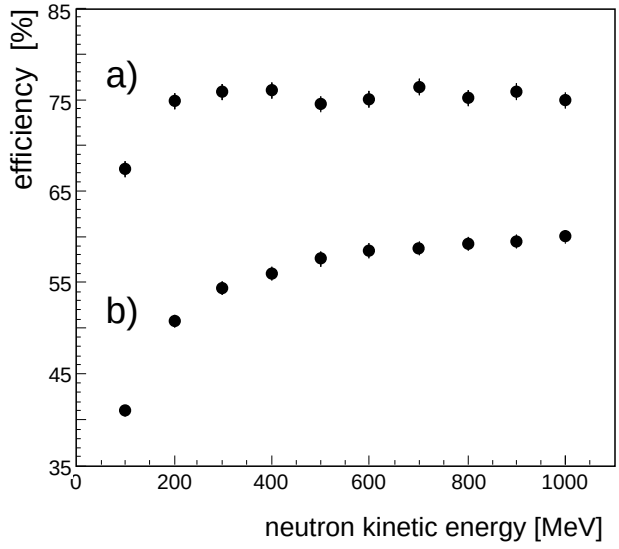

Figure 2.12: The COSY–11 neutron detector efficiency as a function of kinetic energy of simulated neutrons. The curves show the efficiency of the neutron detector itself (a) and the efficiency of neutron detection in the COSY–11 detection system (b). For the detailed description see text.

A direct experimental determination of the neutron detector efficiency is possible via a reaction with a neutron in the exit channel and all remaining other ejectiles being reconstructed. The four-momentum vector of a neutron can be calculated from the missing mass procedure and therefore the number of neutrons which reached the neutron detector as well as their momenta are known. By a comparison of the number of signals observed in the detector to the expected ones the information about the efficiency and their momentum resolution is available. A good candidate for the efficiency investigation could be the $pp \to pn\pi^+$ reaction. In 2001 a short test run was performed and the $pp \to pn\pi^+$ reaction was measured [54] and within a statistical accuracy the cross section was found to be consistent with the literature data.

2.3 Method of the measurement

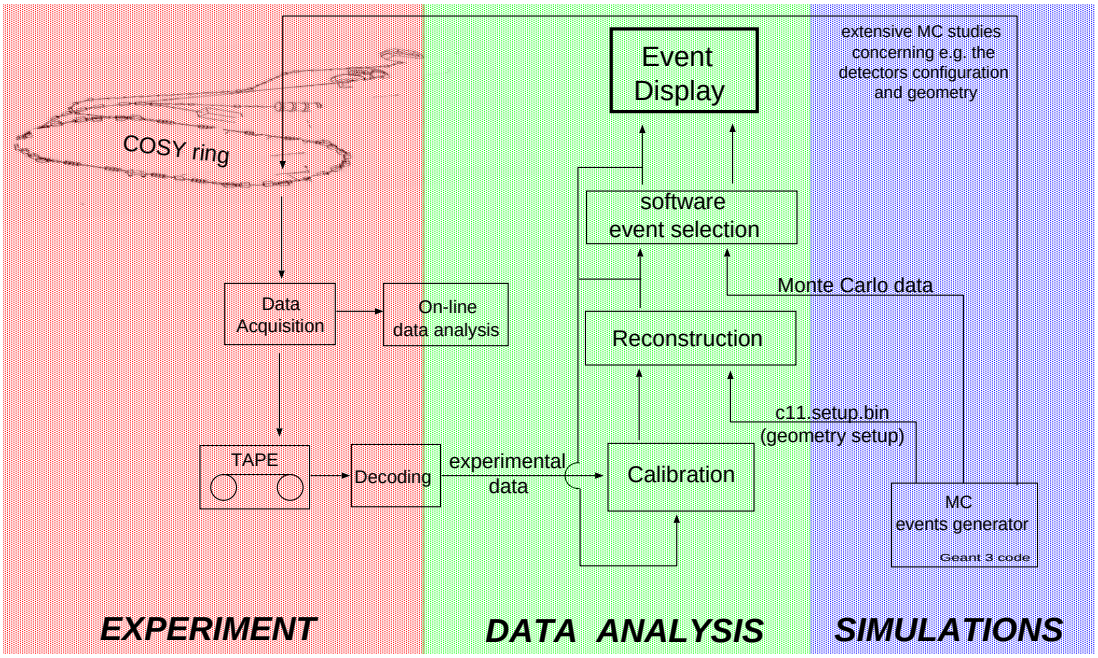

Figure 2.13: Schematic view of the COSY–11 experimental methodology.

In figure 2.13 the whole procedure from the first simulations to the final result of the experiment is shown schematically. Independently of the reaction of interest the experimental methodology stays the same, therefore the description of figure 2.13 and the figure itself is valid for all COSY–11 measurements, thus especially for the channels newly investigated like the $pp \to nK^+\Sigma^+$ reaction hyperon production.

First, extensive MC studies must be done in order to check the detection efficiency for the reaction of interest. The counting rate has to be estimated and the measurement time requirement – depending on the experimental needs – established. Possible background channels and its influence must be checked also in the simulation studies. In order to increase the acceptance of the detection set-up the optimum location of some movable detectors and its geometry has to be determined. At this stage also the trigger conditions are developed.

The $pp \to nK^+\Sigma^+$ reaction, discussed in this thesis, was selected by the identification of a simultaneously produced neutron and K^+ meson in the proton-proton collision. For this measurement the main trigger included a hit in the S1 scintillator detector between the 4th and 16th segment, a hit in the S8 scintillator detector and a hit in the neutron detector (ND) (see figure 2.2), as can be expressed by:

$$T_{\Sigma^+} = S1^{4....16}_{\mu\geq 1} \wedge S8 \wedge ND. \tag{2.2}$$

Only events which fulfill this condition (μ stands for *multiplicity*) within a certain time gate are later taken for further analysis. The S1 region was narrowed down to only 13 modules (from 4th to 16th) in order to decrease the background from elastically scattered protons which in great number give signals in the first modules of the S1 scintillator.

This hardware cut was used since it does not influence the number of registered kaons from the $pp \to nK^+\Sigma^+$ reaction. In the MC studies it was checked that kaons from the reaction of interest don't cross this region of S1 (see figure 2.14).

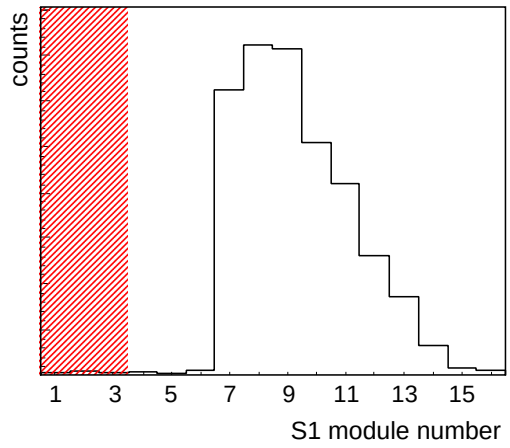

Figure 2.14: The signal distribution in the S1 scintillator detector caused by simulated kaons from the $pp \to nK^+\Sigma^+$ reaction. The hatched area corresponds to the S1 modules region cut out by the hardware trigger. The events sample shown in the figure was generated with the beam momentum $P_{beam} = 2.6$ GeV/c.

Parallel to the T_{Σ^+} trigger, also the elastic trigger was set and events which created a signal in the S4 (see figure 2.4) in coincidence with the S1 scintillator were accepted as elastically scattered protons (see also the subsection 2.4.4).

During the experiment, time signals from the drift chambers, time and signal amplitude information from the scintillator detectors and the silicon pad system are converted from analog signals to digital information by the FASTBUS or CAMAC modules – TDC and ADC [2]. The different subsystems are readout by five PCs of the COSY–11 data acquisition system. The information then is collected by a so-called *event builder* and recorded on tape and parallel send to the Unix work-station which enables the on-line data analysis (see figure 2.13). For more details about COSY–11 data acquisition see [46, 55].

After the measurement period, the data collected on tapes, were decoded, and then the off-line data analysis can be started. As schematically depicted in figure 2.13, first the calibration of the detectors must be done. The calibrations of the neutron detector as well as of the S8 and S1 scintillators are described in sections 2.3.2 and 2.3.1, respectively.

The geometry of the detection system is needed for the reconstruction of particles tracks and the subsequent determination of the momenta of registered particles as well as times of their interaction with the detector. It is not stored in the experimental data file, but rather in the file generated by the MC simulation program, called *c11.setup.bin*. After the reconstruction process, the calibration of some detectors can be improved.

The next step is the *software events selection* described in the section 2.4. The reconstructed particles are identified as protons, pions, kaons or neutrons and to decrease the contribution of the background channels a number of off-line cuts can be developed. For the particular case of the $pp \to nK^+\Sigma^+$ reaction, the invariant masses of all positively charged particles must be calculated to identify kaons. From the realistic MC studies, the width of the kaon peak is extracted, and appropriate cuts must be done in order to select "kaons of interest" for further analysis. If e.g. kaons from the investigated reaction are passing the drift chambers in the specific region (known from MC studies), the calibration

[2] The FASTBUS modules (1881, 1881.M, 1885.F, 1875, 1877 and 1879) were made by LeCroy Corporation, and the CAMAC modules were made at CERN

of this part of the detector with particles identified as kaons can be repeated and thus the accuracy of the kaon momentum determination will increase.

The last step of the analysis procedure, after tracks are reconstructed, particles identified and four momentum vectors extracted is the determination of the required observables. In this thesis the number of Σ^+ hyperons was determined via the missing mass technique for two beam momenta and the total cross sections of the $pp \to nK^+\Sigma^+$ reaction channel was calculated.

2.3.1 S1 and S8 detectors time calibration

To perform the time calibration of the S8 and S1 scintillator detectors (see figure 2.2), the invariant mass method was used. Based on the information from the drift chamber set, the momenta of the particles bent in the magnetic field of the COSY–11 dipole are reconstructed. With the additional information about the velocity of the reconstructed particles their masses can be calculated:

$$M_{inv} = \frac{P}{\beta \cdot \gamma}, \tag{2.3}$$

where M_{inv} is the invariant mass of the particle, P its momentum, β its velocity between S8 and S1 scintillator detector (in units of c) and $\gamma = 1/\sqrt{1-\beta^2}$ is the Lorentz factor. Due to the numerous production of pions and protons in the target region peaks corresponding to those particles are clearly seen in the invariant mass spectrum (see also section 2.4.1). After the drift chamber calibration, with known particles path length between S8 and S1 scintillators, the reconstructed mass of the particle depends only on the time measurement. With the known masses of π^+ meson and proton, the time offset for each of the sixteen modules of S1 and each four modules of S8 detector can be treated as a free parameter. All time offsets were tuned with respect to the first module of S1 detector (the one which is positioned in the closest distance from the accelerator pipe).

As a cross check the time difference between the neighboring modules of S1 was plotted. One track events which gave a signal in two modules were selected as the one which passed the small overlap region of S1 modules. The time difference distribution within the time resolution of S1 must have a mean value in zero (see figure 2.15).

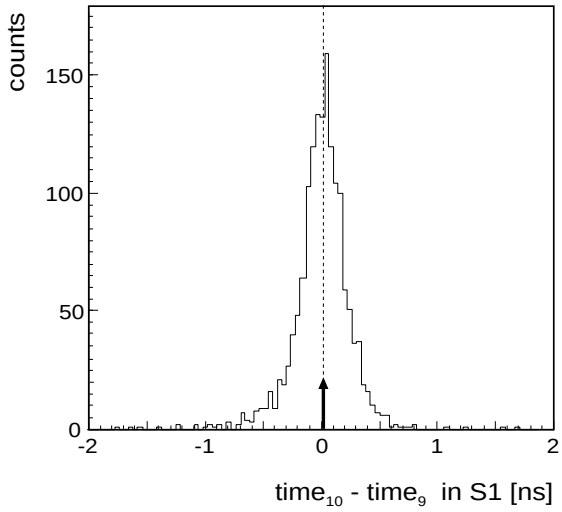

Figure 2.15: The time difference between signals in the 9th and 10th module of S1 scintillator caused by single particle passing through the small overlap region of S1 modules after calibration.

2.3.2 Neutron detector calibration

The precision of the time measurement of the neutron detector is the crucial factor for the neutron momentum determination and thereby the resolution of the Σ^+ mass distribution.

The timing of the neutron detector modules is nearly independent of the hit position within a module since it is taken from the average of the upper and lower photomultiplier signals. In order to relate the time measurement of individual modules it is necessary to know the relative time offsets which are derived by comparing the signals of different modules. From the experimental data the distributions of time differences between neighboring segments were generated and compared to the corresponding spectra from Monte Carlo simulations. The maximum of the fitted distribution of the time differences between neighboring modules along the x axis (see figure 2.9) in MC simulations is positioned at zero. This is not the case for the maximum of the distribution of the time differences between neighboring modules along the z axis. The explanation of this fact is schematically shown in figure 2.16.

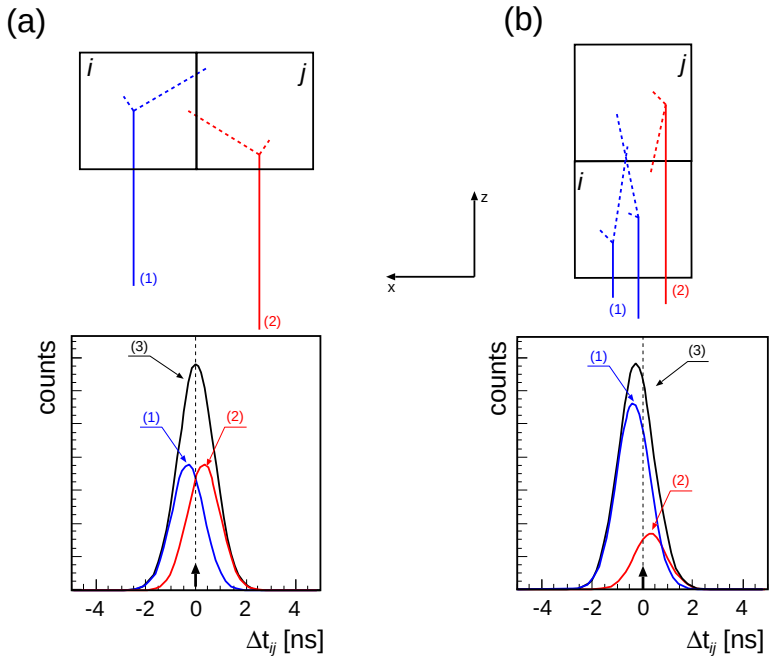

Figure 2.16: Schematic explanation of the time difference distribution between neutron detector modules. The solid lines correspond to neutrons and the doted ones to charged particles tracks. For details see text.

Charged particles produced by neutrons in the ith module of the neutron detector can be a source of the scintillation light not only in the module where the conversion neutron–charged particle has happened, but also in the neighboring modules, e.g. jth module (as it is depicted by the tracks marked (1) in figure 2.16). In this case the time in the ith module is in most cases shorter than the time in jth one. Therefore the time difference distribution Δt_{ij} will have a negative mean value (see curve (1) in the lower part of figure 2.16a). If the conversion *neutron-charged particle* happens in jth module and, as a result of it, the light will be produced also in the ith one, the time difference

distribution Δt_{ij} will have a positive mean value. For two neighboring modules along the x axis (see figure 2.16a), a production of scintillation light in the jth module although the charged particle comes from the ith one and vice versa, has the same probability. Therefore plotting the Δt_{ij} one can expect its mean value at zero (curve (3) in the lower part of figure 2.16a). This is not the case if one neutron cause scintillation light in two neighboring modules along the z axis (see figure 2.16b). Since the hadronic shower is concentrated in the direction of neutron momentum, more often the timing signal in ith module is faster than in jth one, and therefore the Δt_{ij} distribution will have a negative mean value (curve (3) in the lower part of figure 2.16b).

The mean of the experimental distribution (i.e. the differences between the time offsets) and its width reflects: *i*) the time resolution of the involved modules, *ii*) the smearing of velocities of secondary particles and *iii*) the distribution of the positions at which they were created. The time difference measured between the ith and the jth module can be expressed as:

$$\Delta t_{ij} = t^i_{TDC} - t^j_{TDC} = t^i_{real} - t^j_{real} + t^i_{off} - t^j_{off}, \tag{2.4}$$

where t^i_{TDC} and t^j_{TDC} denote the time registered by a TDC in the ith and jth module of the neutron detector, respectively, t_{real} stands for the real time at which the secondary charged particle produced a light signal inside a scintillator and t_{off} is a sum of all delays between the module and TDC values written to tape. As it was already mentioned (depending on the relative position of two neighboring modules) in the experiment the difference $t^i_{off} - t^j_{off}$ was adjusted to zero (case (a) on figure 2.16) or to a certain value given by MC calculations (case (b) on figure 2.16). By the comparison of the experimental Δt_{ij} to the simulated Δt_{ij} of all possible combinations of neighboring modules the relative time offsets for each segment were established. The time resolution of the detector was determined to be 0.4 ns [45]. This number was established by comparison of the width of the simulated distributions with the experimental ones. The example presented in figure 2.17 shows that the shape and the position of the experimental distribution agree very well with the simulated data. The long tails of the distributions may be caused by events where secondary neutral particles with a significantly different velocity induce nuclear reactions in the neighboring segments.

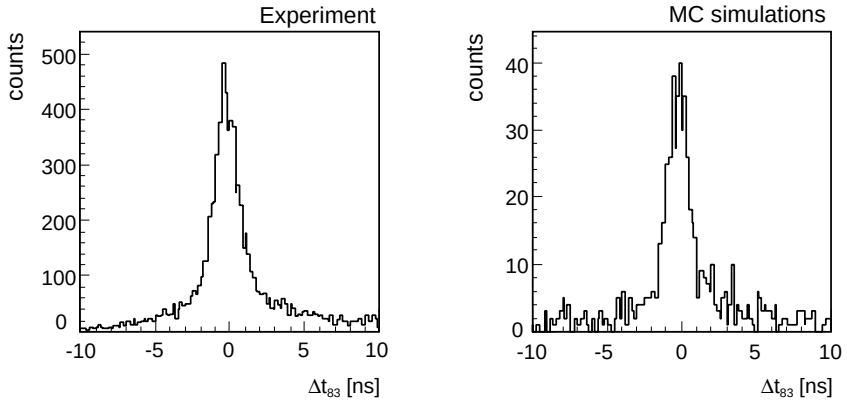

Figure 2.17: Experimental and simulated distributions of the time differences between 8th and 3rd module of the neutron detector.

In addition, the general time offset between the neutron production and the hit time in the neutron detector has to be determined. The global offset was extracted using the $pp \rightarrow pp\pi^0$ reaction. Two-track events with a signal in the neutron detector were selected from the set of data for the beam momentum $P_{beam} = 2.6$ GeV/c. The four-momenta of both protons were determined by backtracking through the known magnetic field to the target point. The π^0 meson was identified via the missing mass technique. The square of the missing mass distribution for two-track events with a signal in the neutron detector is shown in figure 2.18b. Due to the small acceptance, the statistics of the $pp \rightarrow pp\pi^0$ reaction is very low but the π^0 peak in the missing mass distribution is clearly seen.

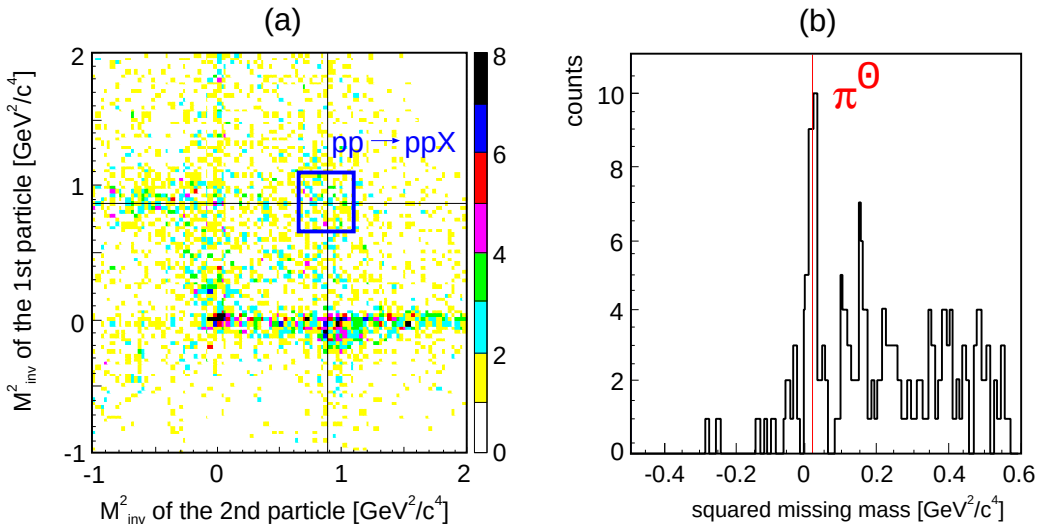

Figure 2.18: Selection of the two-track events for the global time calibration of the neutron detector. In (a) the invariant mass squared of the first particle vs. the second particle is shown. The region around the maximum corresponding to the $pp \rightarrow ppX$ reaction is marked. In (b) the square of the missing mass distribution of events from the marked region is shown. Red line points to the nominal squared mass of the π^0 meson.

Since for the π^0 meson $c\tau = 25$ nm [2] it decays immediately in the target and the γs from the decay will reach the neutron detector without delay with the speed of light. From the distance between the target and the first module which gave the signal in the neutron detector and the speed of light in air, one can adjust the general time offset for the neutron detector with high precision. In figure 2.19 the time distribution for the neutron detector for the selected π^0 events is shown. The total event number as well as the width of the discussed peak corresponds to the expectation from Monte Carlo studies.

The global time calibration for the neutron detector was also done via the $pd \rightarrow ppn_{spec}$ reaction [56]. Protons from the deuteron nucleus are scattered by the proton from the beam, and the remaining neutron (so-called *spectator* neutron) hits the neutron detector. Data have been taken at a proton beam momentum of $P_{beam} = 3.204$ GeV/c and the $pd \rightarrow ppn_{spec}$ events were selected and reconstructed. To determine the global time offset, the n_{spec} time spectra from the experimental data and the simulations were compared. For more details about the global time calibration via the $pd \rightarrow ppn_{spec}$ reaction see Ref. [56].

An energy calibration of the neutron detector using cosmic rays was also done [43].

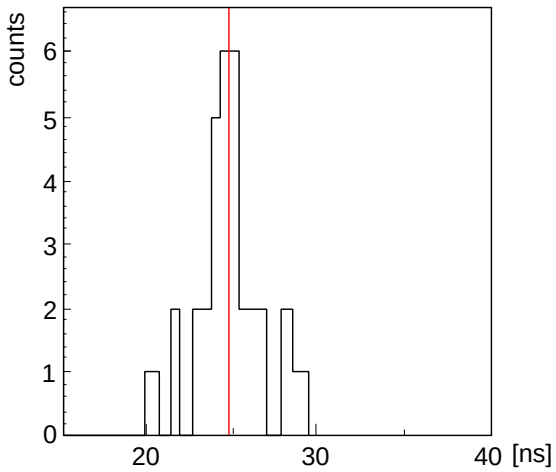

Figure 2.19: Distribution of the time signals in the neutron detector corresponding to the π^0 events. The red line corresponds to the time for light transversing distance target-neutron detector of 7.36 m.

2.3.3 Detection efficiency determination

For the total cross section determination, the knowledge of the detection efficiency is essential. It can be defined as the ratio of number of events which were detected, reconstructed and accepted as events of the studied channel (N_{acc}) to those generated in the target (N_{gen}). The detection efficiency can be then calculated by $E_{eff} = N_{acc}/N_{gen}$. With known cross sections the detection efficiency can be deduced from the experiment. However, this information can not be used for other reaction channels or even for the same one with a different beam momentum. Therefore the efficiency of the COSY–11 detection set-up for the $pp \to nK^+\Sigma^+$ reaction was determined for both beam momenta by Monte Carlo simulation studies. For each event all three particles in the exit channel were tracked in the magnetic field, air and the detectors volumes. The information from the detectors caused by the interaction of simulated particles with the detector volumes was stored and then analyzed in the same way as the experimental data, namely the reconstruction procedure and number of cuts for the simulated and experimental data must be the same. Since the number of simulated events N_{gen} is known, for the efficiency determination, the number of accepted ones N_{acc} must be determined.

The total detection efficiency is a result of the geometrical acceptance of the detection system and the ability of the correct event reconstruction. In reality not all protons in the beam have the same momentum. The beam momentum spread differs from one run to the other, but on the average it is about 1 – 2 MeV/c [31, 46, 57, 58]. From the beam momentum spread and the beam optics one can deduce the beam dimensions. In [31] the horizontal beam dimension was calculated to be 4.1 mm and the vertical one to be 4.5 mm. However, for the efficiency discussion the knowledge of the beam-target overlap region is more crucial. During the experiment, by changing the magnetic field in the steerer magnets [3], the position of the beam relative to the target center is shifted and by maximizing the counting rate of e.g elastically scattered protons, the largest overlap is found. In figure 2.20 the reconstructed vertical position of the reaction point for the

[3] Steerers are small dipole magnets installed around the beam pipe before the COSY–11 dipole in the COSY ring.

elastically scattered protons from present experiment is shown. The standard deviation of this distribution ($\sigma = 4.7$ mm) and calculated vertical beam dimension ($\sigma_y = 4.5$ mm) given in [31] are in good agreement. For the details about the method of the beam momentum spread and beam size determination see Ref. [31].

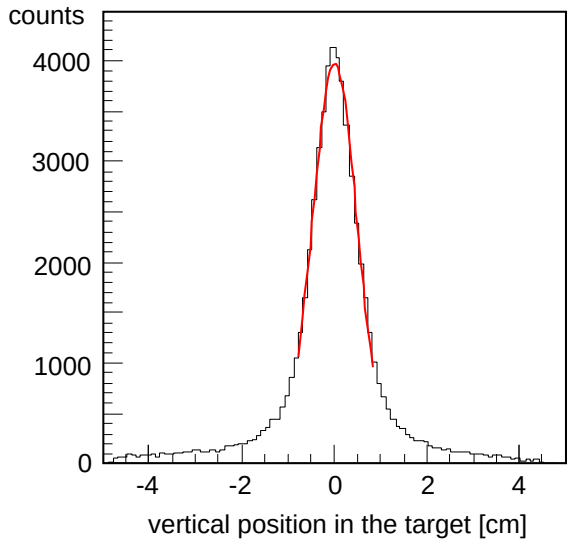

Figure 2.20: The reconstructed vertical position of interaction point for the elastically scattered protons (data for the beam momenta $P_{beam} = 2.74$ GeV/c). The solid curve shows the fitted Gaussian distribution with a standard deviation $\sigma = 4.7$ mm.

The total detection efficiency depends on the efficiencies and resolutions of all detectors used in the experiment. To get the efficiency of the detection system, not only its geometrical acceptance, the beam momentum spread, the size of the beam, detectors efficiencies, its real resolution (time and space one) but also the particle decays were included into the simulation program. These parameters were partly described in section 2.2 and partly were taken from [27].

In studies of the production mechanism close to the reaction threshold higher partial wave contributions are not expected. However, if the excess energy Q for the studied channel go beyond a few MeV range, higher partial waves can contribute to the production mechanism. Since this contribution in case of the Σ^+ hyperon production is essentially unknown, higher partial wave contribution is assumed on the basis of the $pp \to pK^+\Lambda$ channel studied at TOF experiment at COSY [4] in order to get a rough estimate of its influence. For seven different beam momenta in the range from 2.5 GeV/c to 2.85 GeV/c the $pp \to pK^+\Lambda$ reaction was measured and the cross section angular distributions were fitted by Legendre polynomials. Out of these fits the contribution of higher partial waves and the expected angular distribution were determined [59, 60] as a function of excess energy. Then each generated MC event of the $pp \to nK^+\Sigma^+$ reaction was weighted according to the differential cross section. Assuming that in the Σ^+ hyperon production higher partial waves contribute in the same order like in the Λ hyperon production, their influence on the detection efficiency E_{eff} was calculated. The result is shown in figure 2.21b as a function of excess energy Q.

Even though the detection efficiency was determined in MC studies and only the discussed reaction channel was simulated not all events which generate a trigger signal indicate the presence of a neutron and kaon in the exit channel. This is depicted in figures 2.21a and 2.21b, where the detection efficiencies for the same excess energy differ

from the trigger efficiency – depending on the beam momentum – by a factor from 2 to 16 in the excess energy range from 0 to 70 MeV. The Σ^+ hyperon decays into proton and π^0 or neutron and π^+ with about equal branching ratios of 50 % [2]. The π^0 meson decays into two γs which can give a signal in the neutron detector. Also π^+ mesons can produce a trigger signal in the S8 and S1 scintillator detectors as well as in the drift chambers. Moreover, a π^+ can also result from the decay of the generated kaons. The method of kaon and neutron identification, as well as applied cuts which allows to decrease the number of misidentified $pp \to nK^+\Sigma^+$ events are described in section 2.4.

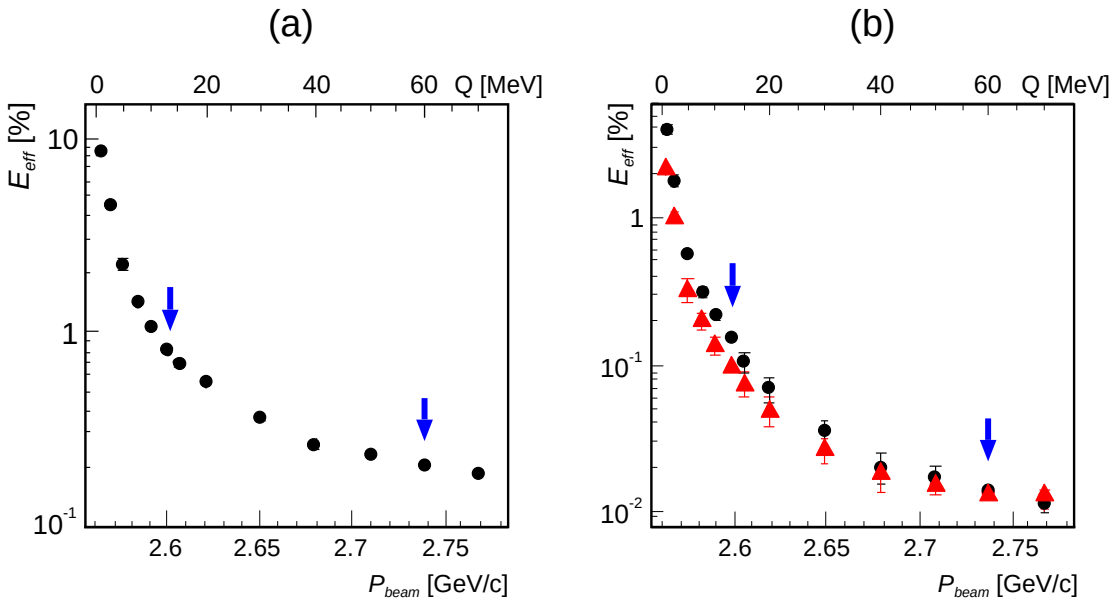

Figure 2.21: The detection efficiency of the COSY–11 detection system for the $pp \to nK^+\Sigma^+$ reaction as a function of the beam momentum P_{beam}. The corresponding excess energy Q is given on separate scale. Arrows show points corresponding to the beam momenta $P_{beam} = 2.6$ GeV/c and $P_{beam} = 2.74$ GeV/c. In (a) the efficiency extracted from the MC events which generated a trigger signal defined by the conditions described in the section 2.3 is shown. In (b) the efficiency distribution showing the events which were first selected by the trigger and then identified in the data analysis as being a kaon and a neutron. The full circles represent calculations under the assumption that only S-wave contributes, full triangles show result of calculations taking into account also higher partial waves.

In table 2.1 the detection efficiencies of the COSY–11 installation for the $pp \to nK^+\Sigma^+$ reaction for the two beam momenta are given. For the cross section calculation (discussed in details in section 2.4.3) the detection efficiency with the assumption that no higher waves than S contribute to the reaction mechanism was taken. The last column of table 2.1 gives the detection efficiency if higher partial waves have a comparable contribution to the Σ^+ hyperon production as in the Λ hyperon production. The inclusion of the higher partial waves gives a rough idea about its influence on the efficiency determination, but was not included in the total systematical error given in table 3.3. Higher partial waves in a strength given in [59, 60] would result in a decrease of the detection efficiency by 30 % for the lower and by 7.7 % for the higher energy data set.

Table 2.1: Detection efficiency of the COSY–11 detection set-up for $pp \to nK^+\Sigma^+$ reaction.

Beam momentum P_{beam} [GeV/c]	Excess energy Q [MeV]	Detection efficiency	
		E_{eff} [%] (only S-wave)	E'_{eff} [%] (S + higher partial waves)
2.60	13.	$(17.20 \pm 0.55 \pm 1.30) \cdot 10^{-2}$	$(12.00 \pm 0.39) \cdot 10^{-2}$
2.74	60.	$(1.43 \pm 0.06 \pm 0.04) \cdot 10^{-2}$	$(1.32 \pm 0.06) \cdot 10^{-2}$

One source of the systematical error undoubtedly is the inaccuracy of the effective detector position of about 2 mm, which leads to an error of the detection efficiency of about 1% [31]. Next, the 0.1 % inaccuracy in the beam momentum determination [42] (which corresponds to the 0.8 MeV and 1 MeV inaccuracy in the excess energy Q for lower and higher energy data set, respectively) can be a source of 7.5 % of error in the detection efficiency determination for lower energy data set, and 2.5 % for higher one. Therefore the systematical error for the efficiencies of the COSY–11 detection system for the $pp \to nK^+\Sigma^+$ reaction sum up quadratically to **7.57 %** for lower and **2.69 %** for higher energy data set.

2.4 Data analysis

In this part the missing mass technique will be introduced (see section 2.4.3) and the four-momenta determination of the remaining reaction products – namely neutron and kaon – will be described (see sections 2.4.1 and 2.4.2, respectively). Finally the luminosity studies will be presented (see section 2.4.4).

2.4.1 K^+ four-momenta determination

Positively charged kaons are identified in the COSY–11 detection system by their invariant masses. For each event the time difference between the S8 (t_{S8}) and the S1 (t_{S1}) scintillator detectors was measured ($\Delta t = t_{S1} - t_{S8}$) and with the known effective distance between these detectors [4] the velocities of the particles passing the detectors were calculated.

The momentum vector of the K^+ meson is established by tracking its trajectory reconstructed from signals registered in the drift chambers (DC1 and DC2) through the magnetic field B back to the target point. The idea is depicted schematically in figure 2.22

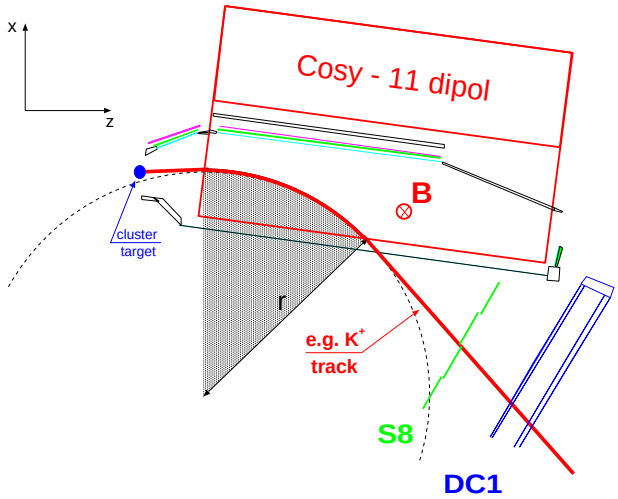

Figure 2.22: Sketch of the momentum reconstruction procedure. The left part shows the target region. For more details see text and section 2.2.3.

For the accurate momentum reconstruction, the knowledge of the magnetic field along the particle track inside the gap and in the fringe field region is crucial. Therefore a precise three dimensional map of the magnetic field was measured [61] for different beam momenta (different electric currents in the magnet) and it is used in the tracks reconstruction procedure. The three components of the momentum vector are calculated with the assumption, that the tracked particle was produced in the target point.

[4] The scintillators S8 and S1 are oriented parallel to each other and the distance between them is about 188 cm. If, however, the angle of the particle path relative to the detector plain was different from 90^o the path length is longer than the distance S8 – S1. Therefore the path length X was calculated regarding the angle (known from the drift chamber reconstruction) between particle path direction and the detector plain : $X = d \cdot \sqrt{1 + tg\alpha_{xy}^2 + tg\alpha_{xz}^2}$, where d denotes the fixed S8 – S1 distance, whereas α_{xy} and α_{xz} are the angles of the particle path relative to the detectors in the xy and xz planes respectively (see figure 2.35).

Thus, the combination of the velocity β of the particle and its total momentum P allows to determine for each event the invariant mass from equation 2.3 given in section 2.3.1.

Figure 2.23 shows the squared invariant mass of the positively charged particles which fulfilled the trigger conditions and were measured at 2.74 GeV/c beam momentum. The pion and proton peaks are clearly seen and the mean values of the Gaussian function fitted to these peaks (not shown in figure 2.23) are in a very good agreement with the squared nominal masses of the π^+ meson and the proton. The kaon peak – although clearly seen – lies on the significant background, the ratio of peak to background is 1.4 to 1.

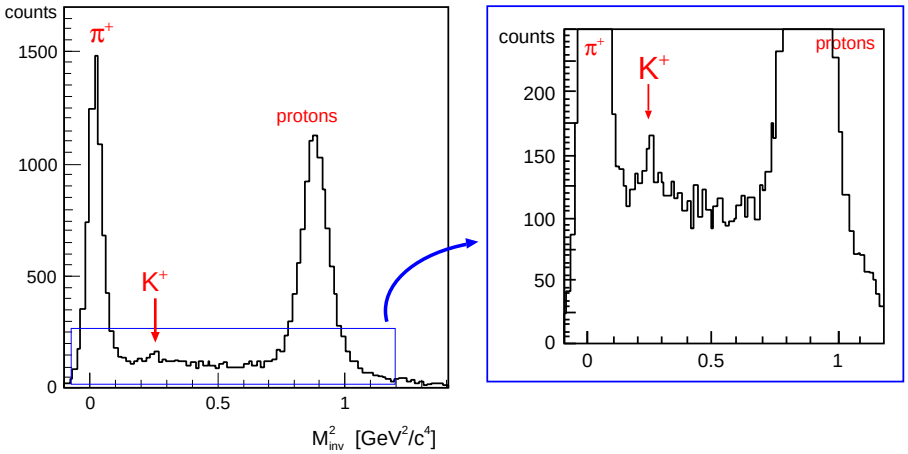

Figure 2.23: The invariant mass squared distribution for the positively charged particles bended in the dipole gap for $P_{beam} = 2.74$ GeV/c. The arrows show the squared mass for the K^+ meson.

For the lower energy data at $P_{beam} = 2.6$ GeV/c the K^+ peak does not show up prominantly in the invariant mass distribution, therefore it is assumed that its position (μ_{exp}) and width (σ_{exp}) is in agreement with the produced MC data as it is the case for the $P_{beam} = 2.74$ GeV/c. This assumption about the peak position is justified since in this invariant mass spectrum the π^+ as well as the proton peak are at the correct positions. It is worth to mention, that the information about width and position of the kaon peak in the experimental invariant mass distribution is fundamental. Cuts around the kaon mass which are applied in order to determine the correct number of $pp \to nK^+\Sigma^+$ events registered during the measurement are described in sections 2.4.3 and 3.1.

The origin of the background around the kaon mass, which is observed in the invariant mass distribution, has several reasons. Mainly pions, but also protons which contribute to it: *i*) come from different than $pp \to nK^+\Sigma^+$ reactions, *ii*) are decay products and/or *iii*) are due to secondary interactions produced in a great number in collisions of primary reaction products with e.g. scintillators, vacuum chamber walls, air etc.

In the analysis described in this thesis the velocity of positively charged particles (kaons) was determined from the time information from the S8 and S1 detectors. The relatively small distance between them and the vicinity to the dipole gap cause a much larger contribution of scattered particles to the background of the $pp \to nK^+\Sigma^+$ reaction, than in reactions with at least one proton in the exit channel. For instance in the experiments

where two protons from the exit channel are reconstructed (like $pp \to pp\eta$), the time of flight is measured between S1 and S3 scintillators with a distance of about 9.4 meters (see figure 2.6). In fact the long flight path between the target point and the S3 hodoscope drastically reduces the detection of the particles scattered e.g. inside the dipole. In case of the reactions with proton and kaon in the exit channel (like $pp \to pK^+\Lambda$), the time information for proton is taken again from S1 and S3 hodoscopes, and the velocity of K^+ is measured between the target point [5] and S1 scintillator. This explains why the K^+ peak is better seen in $pp \to pK^+\Lambda$ /Σ^0 data [57] than in $pp \to nK^+\Sigma^+$ described here.

In order to understand the background distribution, 22 reaction channels [6] (for each of the two beam momenta) were simulated and their contributions to the missing mass distribution were checked. In addition to the $pp \to pK^+\Lambda$, $pp \to pK^+\Lambda\gamma$ or $pp \to pK^+\Sigma^0$ reactions, mostly multi-pion reactions were studied. Each simulated channel was analyzed in the same way as the experimental data. Then, with known detection efficiencies and cross sections for the different channels, the expected number of events contributing to the invariant mass distribution for each reaction was determined. The contributions of different channels to the missing mass spectrum are discussed in detail in section 2.4.3.

As a cross check for the momentum reconstruction procedure, the momenta of particles were determined via their velocity (time of flight) measurement ($p_{TOF} = m{\cdot}\beta{\cdot}\gamma$). Here the "space" information from the drift chambers is not used, and therefore the Time-Of-Flight momentum determination (p_{TOF}) and reconstructed momentum determination (p_{recon}) are two independent methods and can be compared with each other. For this procedure, however, the mass m of the particle must be known. In figure 2.24 the difference between the p_{TOF} and p_{recon} for the events selected from the invariant mass distribution as protons is shown. The mean value of this distribution is at zero, what means that these two methods are consistent.

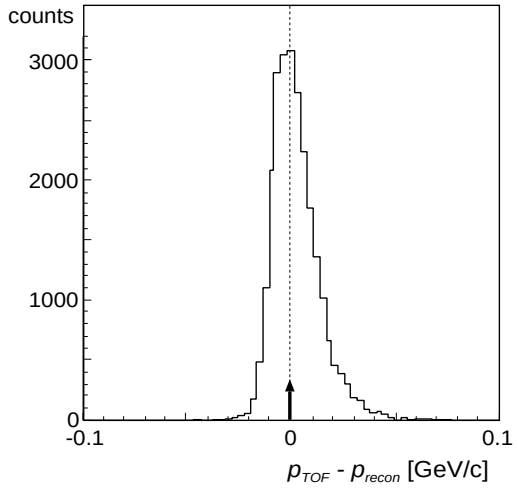

Figure 2.24: Difference between the p_{TOF} (momentum determined via the time measurement between S8 and S1) and p_{recon} (momentum determined via the track reconstruction in the magnetic field) under the assumption that selected from the invariant mass distribution particles are protons.

A second independent check of the invariant mass determination for positively charged particles was an energy loss investigation in the scintillator detectors. When charged particles pass through material they lose energy. The energy loss for particles with the same charge, depends on the velocity β and path length in the scintillator. Therefore,

[5] Time of the reaction in the target is known from the proton backtracking.

[6] The full list of simulated reactions is available in the table 2.2 in section 2.4.3.

after a correction regarding the path length in the detector [7], an independent particle velocity measurement is possible via the energy loss information from the scintillators. The energy loss due to ionization, which is the main contribution for the charged particles in those studies, is given by the Bethe-Bloch formula [2]. In the figure 2.25 the squared invariant mass distribution M^2_{inv} versus ADC channel in the S8 scintillator detector for the lower energy data sample is shown. The distribution looks very reasonable. With the mean energy loss for pions and protons a continous energy loss curve can be determined (see dashed line in figure 2.25). The enhancement due to kaons should be located at the crossing of this line with the invariant mass, however an improved selection of kaons is not achived with this additional information.

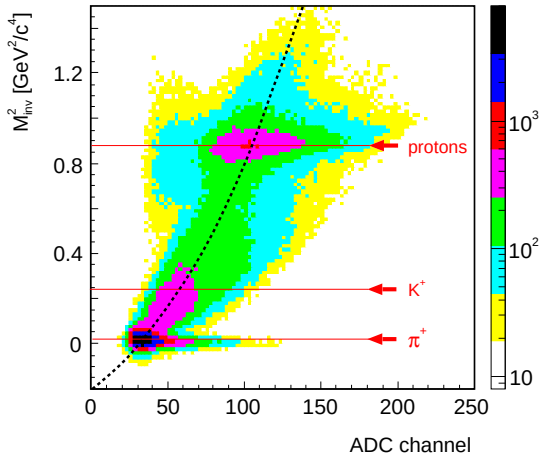

Figure 2.25: The distribution of squared invariant mass M^2_{inv} as a function of the ADC channel in S8 detector for the lower energy data sample.

2.4.2 Neutron four-momenta determination

The neutron total momentum is given by its known mass m_n and the measured velocity β_n:

$$p_n = m_n \cdot \beta_n \cdot \gamma_n. \tag{2.5}$$

The neutron velocity β_n is calculated from the distance between the target point and the central part of the first module which fired and the time difference ($\Delta t_n = t_{det} - t_{tar}$) between the conversion point in the neutron detector (t_{det}) and the reaction time in the target (t_{tar}). The time in the target is known from the backtracking of the positively charged particle to the interaction point. The correct Δt_n value results from the global time calibration of the neutron detector (see section 2.3.2).

The components along the x and z axes are given by the first hit module of the detector. The momentum component along the y axis is assumed to be zero, since it can not be reconstructed due to the fact that the COSY–11 neutron detector is not sensitive in the up-down direction. A sketch of the neutron momentum reconstruction procedure is shown in figure 2.26.

[7] The path length of the particle in S8 or S1 scintillator depends on the angle between particle path and the detector plain. This angle is given by the drift chambers and with known thickness of the scintillation material, the length of the particle path can be calculated.

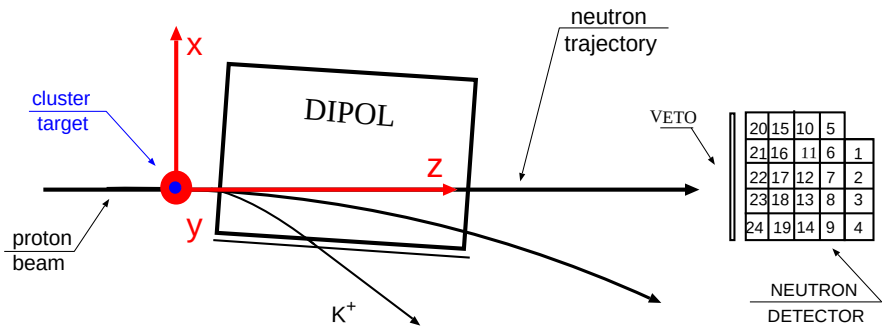

Figure 2.26: Sketch of the momentum reconstruction procedure for neutron. For more details see text.

The signals coming from charged particles is discriminated by VETO scintillators. They do not, however, discriminate γs which are flying in the direction of the neutron detector. A discrimination of the ADC signals (given by either a neutron or a γ) was done by introducing a time cut for the neutron detector. From the reaction kinematics, the highest possible momentum in the laboratory system for neutrons produced in the $pp \to nK^+\Sigma^+$ reaction is 1113.0 MeV/c and 1385.0 MeV/c for the lower and higher beam momenta, respectively. With the relation:

$$\beta_n = \frac{p_n}{\sqrt{p_n^2 + m_n^2}}, \tag{2.6}$$

where the β_n, p_n and m_n are the velocity, total momentum and mass of neutron, respectively, the shortest time for the neutrons from the $pp \to nK^+\Sigma^+$ reaction can be calculated to be 34,1 and 31,7 ns for lower and higher beam momentum, respectively. This allows to take only events for which the time registered in the neutron detector was higher than *29 ns* (for both beam momenta). This we called *neutron time-cut*.

In figure 2.27a the MC distributions of time of flight are shown for neutrons from the $pp \to nK^+\Sigma^+$ reaction. The black dashed curve corresponds to data simulated with the higher beam momentum, and the green solid one to the lower energy data. The black (1) and green (2) arrows show the time for the fastest neutrons for the two beam momenta. A small bump on the left hand side of the *neutron time-cut* is caused by the γs resulting from the Σ^+ hyperon decay [2].

In order to understand the experimental time of flight distribution in the neutron detector, data samples of simulated reactions (listed in table 2.2) were analyzed for each of the two beam momenta separately and their contributions to the distribution were investigated. All studied reactions can be, in principle, divided into three groups: *i*) with γ (or particles decaying into γ) in the exit channel, *ii*) with γ and neutron (also as a decay product) in the exit channel and *iii*) only with neutron (or particles decaying into it) as one of the ejectiles. Each simulated reaction was analyzed in the same way as the experimental data. As an example, the experimental distribution for the beam momentum $P_{beam} = 2.6$ GeV/c (together with some simulated spectra) is depicted in figure 2.27b. The blue arrow (1) in figure 2.27b shows the time for light traversing the distance target

- neutron detector and thereby the time of flight for γs reaching the detector. Their large number is a result of: *i*) particle decay (like the decay of π^0 meson into two γs with a branching ratio of about 99 % [2]), *ii*) direct γ production in the target point (for example in the $pp \to pK^+\Lambda\gamma$ reaction) or/and *iii*) the scattering e.g. on the iron dipole walls. During the MC studies of different reaction channels it was observed that the *neutron time-cut* removes nearly all γs from the data set, γs resulting from the particles decay and those directly produced in the target. The cut on time of flight excludes all background reactions from which a signal in the neutron detector is given by γs only e.g. $pp \to pp\pi^0$ (π^0s) or $pp \to pp\eta$ [8]. The time of flight distribution in the neutron detector caused by the γs in principle has the same shape independently on the channel and the beam momentum. In figure 2.27b) an example of such a simulation for the $pp \to pp\pi^0$ and $pp \to pp2\pi^0$ reactions is shown (red and green areas, respectively). Both distributions peak at 24,56 ns which is the time for light for a distance of 736 cm. Since for γs the probability of the conversion to the charged particles is highest in the first row of the neutron detector (see figure 2.10 in section 2.2.5), most of the events give there a scintillation signal. However, it is also possible that a γ converts in the other modules. That is why the γ time of flight distribution is not symmetrical, but has a longer tail towards higher time values.

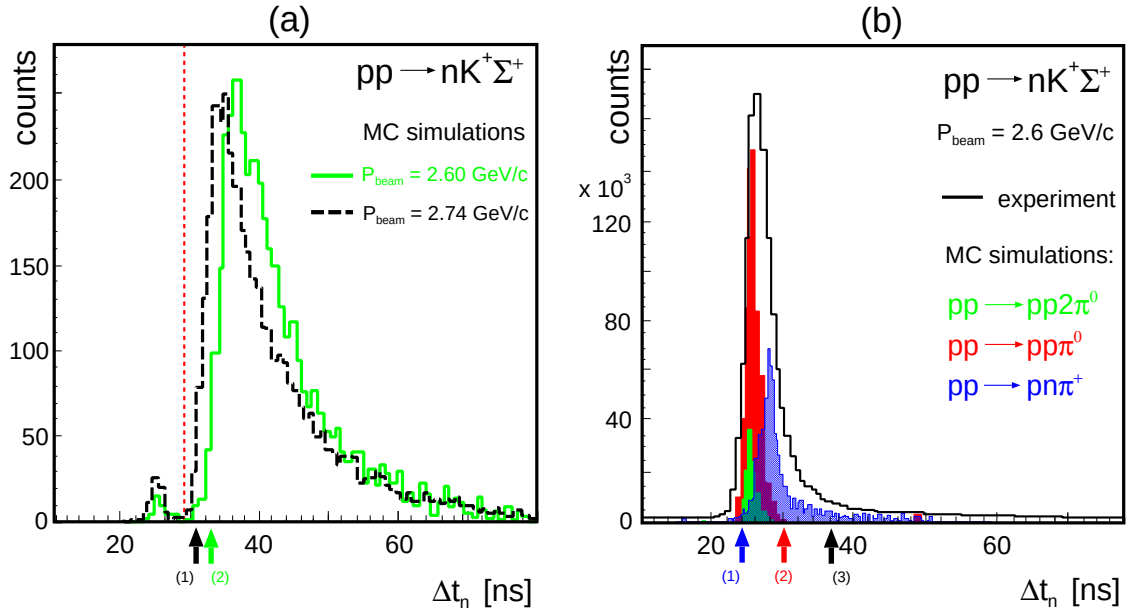

Figure 2.27: (a) Simulated time of flight distributions for neutrons reaching the neutron detector. Arrows (1) and (2) indicate the times of fastest neutrons for the two beam momenta, the dotted line shows the neutron time-cut. (b) Comparison of some simulated background contributions with the experimental neutron time of flight spectrum for the beam momentum $P_{beam} = 2.6$ GeV/c. The black arrow (3) indicates the most probable time of flight for neutrons from the $pp \to nK^+\Sigma^+$ reaction. The red arrow (2) shows where the *neutron time-cut* was applied. The blue arrow (1) points to the time of flight of gammas.

[8] η meson decays inter alia into γs and π^0 [2].

For reactions where in the exit channel neutrons and γs (or particles which decay into γs) are present, due to the *neutron time-cut* their contribution to the background is reduced, but not excluded. The reduction depends on the reaction channel and the excess energy. For example for the $pp \to pn\pi^+\pi^0$ reaction at $P_{beam} = 2.6$ GeV/c the *neutron time-cut* reduces the contribution of this channel to the background by a factor of four and for the $pp \to pn\pi^+2\pi^0$ reaction by a factor of two. For the simulations with the higher beam momentum this reduction is slightly larger and amounts to a factor of 5 and 2.5 for the $pp \to pn\pi^+\pi^0$ and $pp \to pn\pi^+2\pi^0$ channels, respectively.

For reactions with neutrons but without γs in the exit channel, the reduction of number of background events can be small, and depends on the excess energy. The *neutron time-cut* do not exclude the misidentification of neutrons from different reaction channels. The fastest neutrons are generated in the $pp \to pn\pi^+$ reaction [9]. For the lower beam momentum their maximum momentum in the laboratory system is 2440 MeV/c, corresponding to a velocity of about 94 % of the speed of light and the time of flight is about 28 ns. In figure 2.27b the possible $pp \to pn\pi^+$ contribution to the experimental time of flight distribution is shown. For this reaction channel, simulated for $P_{beam} = 2.6$ GeV/c, about 65 % of the events will not be excluded from the data set by the *neutron time-cut*. For the other analyzed background reactions with neutron in the exit channel, the excess energy is smaller than for the $pp \to pn\pi^+$ production. Therefore, the maximal energy of the neutrons is expected to be smaller and the corresponding time of flight longer. For example for the $pp \to pn2\pi^+\pi^-$ reaction the excess energy for $P_{beam} = 2.6$ GeV/c is 339 MeV ($Q = 618$ MeV for the $pp \to pn\pi^+$ channel), and the background events reduction due to the *neutron time-cut* in the experimental data is expected to be on a level of 50 %. In general, for the background reactions with neutron in the exit channel, a very restrictive *neutron time-cut* for γs will be less efficient the smaller excess energy is available.

The decrease of the detection efficiency for the $pp \to nK^+\Sigma^+$ reaction caused by the application of the *neutron time-cut* is far less than 1%, and it is taken into account in the detection efficiency calculations. On the other hand this cut decreases the number of background events in the experimental data set by more than 70 %.

2.4.3 Missing mass investigation

Knowing the four-momentum vector of *n-1* particles for the reaction with n particles in the exit channel and the momentum and energy of the beam particle as well as the target one, the calculation of the four-vector $\mathbb{P}_x$ and the mass m_x (missing mass) of the not detected particle is possible. Let us define

$$\mathbb{P}_x = (\vec{P}_x, E_x) \qquad \text{and} \qquad m_x^2 = E_x^2 - \vec{P}_x^2, \tag{2.7}$$

where the energy E_x of the missing particle is given by:

$$E_x = E_{beam} + E_{target} - E_1 - E_2 - ... - E_{n-2} - E_{n-1} \tag{2.8}$$

and the momentum $\vec{P}_x$ of the missing particle is given by:

[9] The energy of the particles in the exit channel depends on the available energy in the system – namely on the excess energy Q. The higher Q, the higher energy particles can be produced in the target point.

$$\vec{P}_x = \vec{P}_{beam} + \vec{P}_{target} - \vec{P}_1 - \vec{P}_2 - ... - \vec{P}_{n-2} - \vec{P}_{n-1}. \tag{2.9}$$

For the fixed-target experiment like COSY–11[10] and particularly for the $pp \to nK^+\Sigma^+$ reaction, the missing mass squared of Σ^+ reads:

$$m_x^2 \equiv m_{\Sigma^+}^2 = (E_{beam} + E_{target} - E_n - E_{K^+})^2 - (\vec{P}_{beam} - \vec{P}_n - \vec{P}_{K^+})^2. \tag{2.10}$$

The methods of determining of energies and momenta of neutron and kaon were described in previous sections.

In figure 2.28 the experimental distributions of the squared missing mass (m_x^2) of the $pp \to nK^+X$ system for two beam momenta are shown. Neutrons were selected as described in section 2.4.2, and kaons by the invariant mass determination. For the histograms shown in figure 2.28 only the $\pm$ 0.5 σ region around the K^+ mass (kaon invariant mass distribution can be fitted by Gaussian) were taken. For both missing mass spectra a relatively slow increase of the counting rate towards higher masses ends up with a pronounced maximum and is followed by a strong decrease which ends at the kinematical limit [11]. For the higher beam momentum, an enhancement around the squared Σ^+ mass is clearly seen on a significant background (figure 2.28b), but for the lower beam momentum a Σ^+ peak is not directly visible.

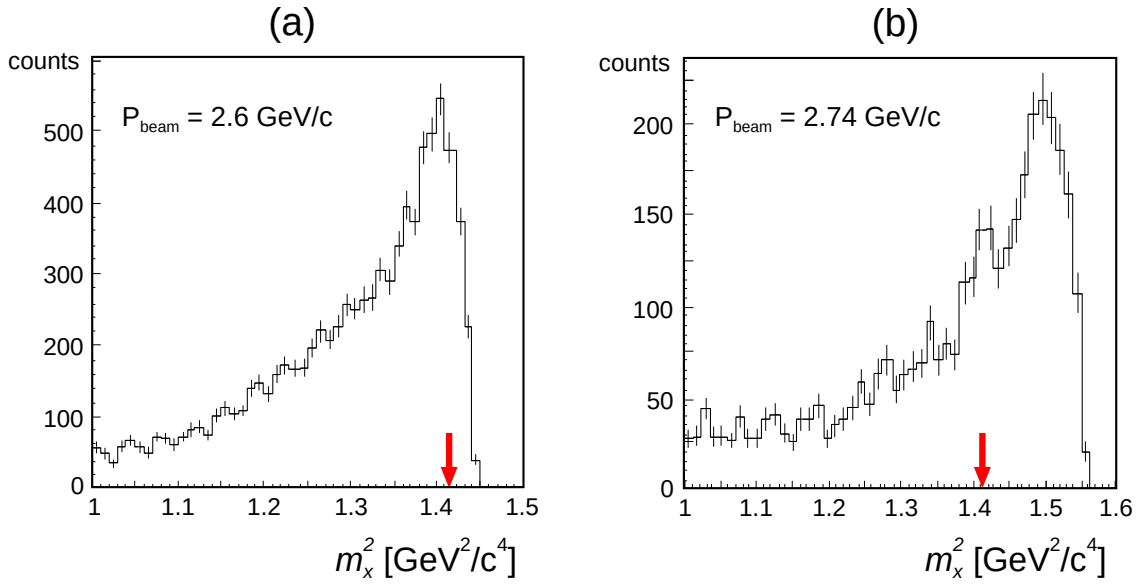

Figure 2.28: The experimental squared missing mass of the $pp \to nK^+X$ system for two investigated beam momenta. The arrows point to the nominal squared mass of the Σ^+ hyperon. The statistical errors of the counting rates are shown.

[10] In the laboratory system, the target proton is assumed to be in rest, therefore its momentum is zero.

[11] The kinematical limit is defined as a sum of the mass of the missing particle and the excess energy. In case of $pp \to nK^+\Sigma^+$ reaction this limit is 1.445 GeV^2/c^4 and 1.561 GeV^2/c^4 for lower and higher beam momenta, respectively.

To extract the number of Σ^+ events from the higher energy data set the shape of the background must be known. For that purpose extended Monte Carlo studies were done in which 22 different reaction channels were analyzed in the identical way like the experimental data. The full list of analyzed reactions is presented in table 2.2.

Table 2.2: List of the threshold momenta and excess energies for the various reactions involved in the background investigation studies.

Reaction channel $pp \rightarrow$	Threshold momentum P_{thres} [MeV/c]	Excess energy Q [MeV]	
		P_{beam} = 2.6 GeV/c	P_{beam} = 2.74 GeV/c
$nK^+\Sigma^+$	2560.5	13.24	59.84
$pK^+\Lambda$	2339.3	88.2	134.8
$pK^+\Lambda\gamma$	2339.3	88.2	134.8
$pK^+\Lambda\gamma\gamma$	2339.3	88.2	134.8
$pK^+\Sigma^0$	2566.1	11.35	57.95
$pp\pi^0$	776.5	624.0	671.0
$pp\eta$	1982.0	211.0	258.0
$pp2\pi^0$	1192.0	489.0	536.0
$pp\eta\pi^0$	2372.5	76.9	123.0
$pp\pi^+\pi^-$	1218.7	480.0	526.0
$pp3\pi^0$	1577.6	354.0	401.0
$pp\pi^0\pi^+\pi^-$	1603.6	345.0	392.0
$pp4\pi^0$	1960.5	219.0	266.0
$pp2\pi^0\pi^+\pi^-$	1986.7	210.0	257.0
$pp2\pi^+2\pi^-$	2013.0	201.0	247.0
$pp5\pi^0$	2350.4	84.0	131.0
$pp3\pi^0\pi^+\pi^-$	2377.3	75.0	121.0
$pp\pi^0 2\pi^+ 2\pi^-$	2404.3	66.0	113.0
$pn\pi^+$	796.2	618.0	665.0
$pn\pi^+\pi^0$	1209.2	489.0	590.0
$pn\pi^+ 2\pi^0$	1594.2	348.0	395.0
$pn2\pi^+\pi^-$	1620.2	339.0	386.0

For all simulated reactions only events giving a signal in the neutron detector and simultaneously in the S8 and S1 scintillator detectors were taken into account for further analysis. Next the *neutron time-cut*, as well as the cut on the invariant mass distribution around the kaon mass, were done and the missing mass of the nK^+ system determined. Energies of neutrons and kaons needed for the missing mass calculation were calculated from the equation:

$$E_{n/K^+} = \sqrt{m^2_{n/K^+} + \vec{P}^2_{n/K^+}}, \tag{2.11}$$

where m_{n/K^+} is the nominal mass of neutron or kaon, despite that not only kaons (but also a large number of pions and protons) from the kaon mass range fulfill the invariant mass cut. $\vec{P}_{n/K^+}$ is the momentum of neutron or kaon. Although none of the analyzed background reactions has a neutron and kaon in the exit channel, for some of them the decay products were giving a required signal in the detectors, as for the $pp \rightarrow pK^+\Lambda$ reaction where neutrons come from the Λ decay. From the same decay channel the $\pi^0 \rightarrow 2\gamma$

decay [2] could give a signal in the neutron detector, but those events were removed by the *neutron time-cut*. In general, from all the reactions listed in table 2.2 only the first four (besides the reaction under investigation) contributed to the background of the missing mass distribution.

For the background investigation, the cross sections for the reactions taken into account are needed. Together with the detection efficiency, the expected number of events under the missing mass spectrum can then be calculated. For the $pp \to pK^+\Lambda$ and $pp \to pK^+\Sigma^0$ channels the cross sections are known [57, 62–64] and the number of events in the background were calculated. For the $pp \to pK^+\Lambda\gamma$ and $pp \to pK^+\Lambda\gamma\gamma$ reactions the cross sections are unknown and therefore the amplitudes of these two channels and additionally the $pp \to nK^+\Sigma^+$ channel amplitude, were used as free parameters in the least squares fit to the experimental missing mass distribution. As an output of the fitting procedure the scaling factors for each of these channels with unknown contribution in the background of the missing mass distribution were obtained. Figure 2.29 shows the result of these background investigation for the beam momentum $P_{beam} = 2.74$ GeV/c. Part (a) of this figure gives a comparison of the experimental spectrum with the channels contributing to the background. Due to the small cross section, the contribution of the $pp \to pK^+\Sigma^0$ reaction is negligible. In part (b) again the experimental distribution is compared with the sum of all background components showing a good description of the observed background.

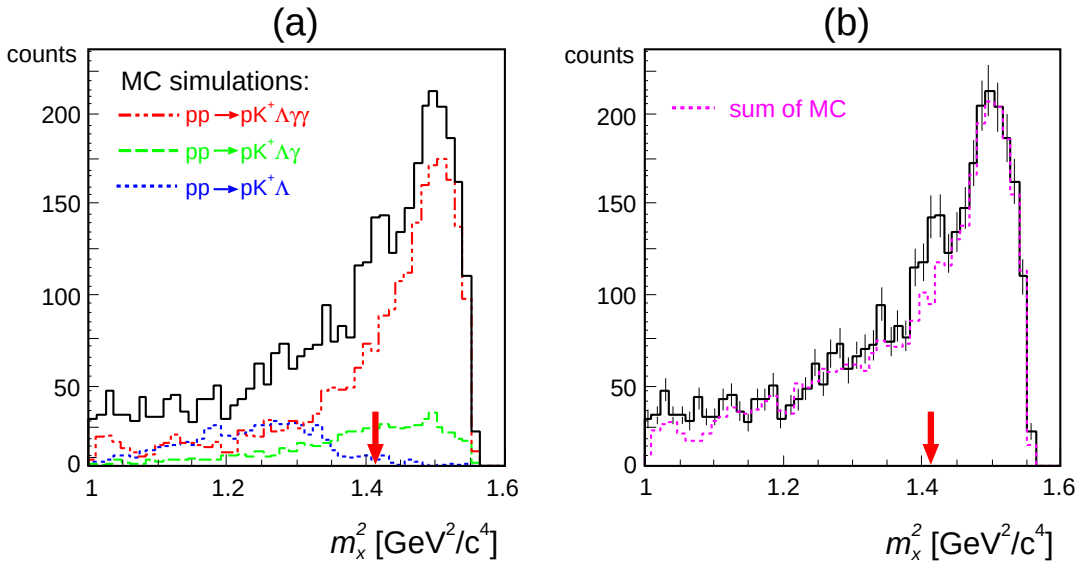

Figure 2.29: Comparison of the experimental squared missing mass (m_x^2) spectrum of the $pp \to nK^+X$ system for the beam momentum $P_{beam} = 2.74$ GeV/c (full black curve) with: (a) fitted background contributions (see text for details) and (b) summed background (error bars indicate the statistical errors). Arrows show the nominal squared mass of the Σ^+ hyperon.

From figure 2.29 one could draw the conclusion, that the background of the missing mass distribution is understood and the number of Σ^+ hyperon events can be deducted. Since between the lower and the higher energy data there opens no new channel, the background components in the missing mass distribution for both data sets is expected to be the same. Additionally from the number of events under the missing mass distri-

bution for higher energy data and with known detection efficiency, the cross sections for $pp \to pK^+\Lambda\gamma$ and $pp \to pK^+\Lambda\gamma\gamma$ can be calculated. If the cross sections of these reactions scale with the phase space, the cross section for the lower energy can be assumed, and together with the known detection efficiency the expected number of events corresponding to $pp \to pK^+\Lambda\gamma$ and $pp \to pK^+\Lambda\gamma\gamma$ channels under the Σ^+ peak can be deducted. For that, however, the exact contribution of the background channels must be known and that is not the case, since there is a very strong correlation between the scaling factors for the $pp \to pK^+\Lambda\gamma$ and $pp \to pK^+\Lambda\gamma\gamma$ reactions. Decreasing the contribution in the missing mass background of the $pp \to pK^+\Lambda\gamma\gamma$, the shape of the sum of all simulated channels can be preserved by increasing the contribution of $pp \to pK^+\Lambda\gamma$. Although the shape of the experimental missing mass distribution seems to be well described, it is not feasible to judge the exact contribution of the particular reactions. Besides, the description of the missing mass distribution must be consistent with the description of others experimental parameters. The reactions and their contributions given by the missing mass background investigations can describe e.g. the invariant mass distribution or the time of flight spectrum for neutrons qualitatively but not quantitatively.

Additionally, the cross sections of the background channels which result from the fit parameters are rather unexpected. The missing mass background investigations would result in a cross section for the $pp \to pK^+\Lambda\gamma\gamma$ channel about 8 times higher than the cross section for the $pp \to pK^+\Lambda\gamma$ reaction. One would naively expect the contrary behavior. The $pp \to pK^+\Lambda\gamma\gamma$ cross section due to the additional γ in the exit channel – assuming that it comes from a direct production mechanism driven by the electromagnetic interaction – should be about a factor of the fine-structure constant [12] smaller than the cross section of the $pp \to pK^+\Lambda\gamma$ channel. If the intermediate production of resonances is involved which subsequently decay into channels including γs, the cross section can be of course very different.

Summarizing, the missing mass background description by the reactions given in the table 2.2 is rather questionable. The basic doubts like the unexpected high cross section of the $pp \to pK^+\Lambda\gamma\gamma$ reaction, or the strong correlations of fit parameters, lead to the conclusion, that the background under the missing mass spectrum is not completely understood. Other background sources like secondary interactions seems to be present. In principle studies of such background sources are possible with the COSY–11 Monte Carlo program, because all hardware components are included. But in practice it is impossible due to time consuming simulations which then must be done.

Since the background components are partly unknown, a two parameter fit of a polynomial function superposed by the expected missing mass distribution of the nK^+ system for the $pp \to nK^+\Sigma^+$ reaction given from the simulation studies has been done – assuming the background shape is smooth. This assumption is justified by the smooth distribution resulting from the fit with known background channels. A kind of peak structure is not expected from the other possible background channels since all reasonable reactions have more than one neutral particle in the exit channel.

In figure 2.30a the experimental missing mass spectrum of the $pp \to nK^+X$ system is compared with fitted polynomial function and the missing mass distribution expected from the Monte Carlo studies. The χ^2 per degree of freedom of the fit is 1.47 which indicates a reasonable description of the data. Figure 2.30b shows the result of the subtraction of

[12] Fine-structure constant $\alpha = 7,297 \cdot 10^{-3} = 1/137{,}036$ [2]

the fitted polynomial from the experimental missing mass distribution together with the MC missing mass distribution. In figure 2.30b only statistical errors are shown [13].

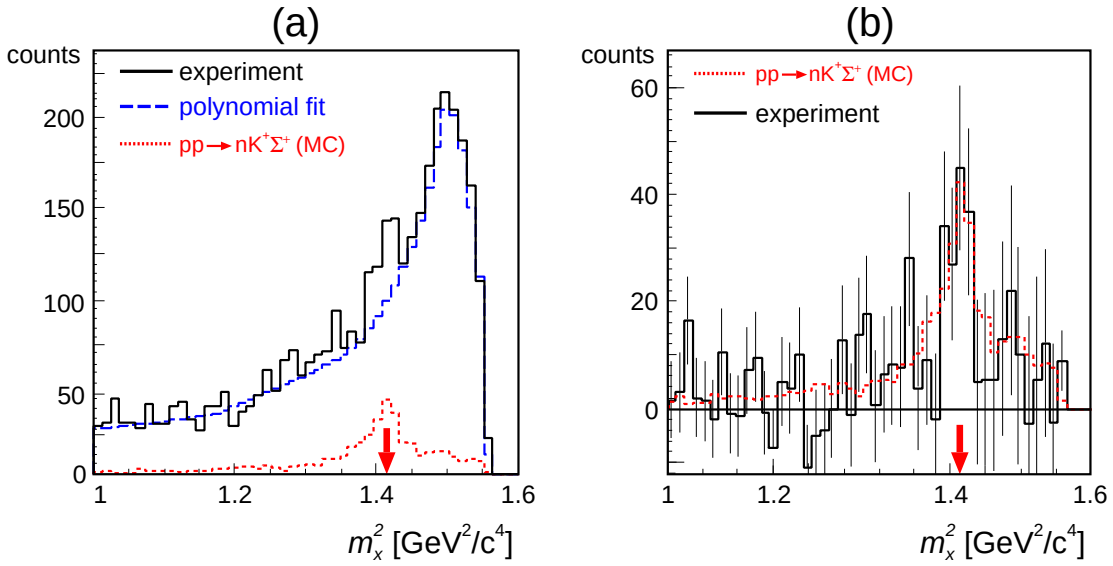

Figure 2.30: Background investigation for the $pp \to nK^+\Sigma^+$ reaction at $P_{beam} = 2.74$ GeV/c. (a) the experimental squared missing mass spectra of the $pp \to nK^+X$ system compared to a polynomial fit and simulated $pp \to nK^+\Sigma^+$ spectrum. (b) result of the subtraction of the fitted background from the experimental distribution compared with the simulated spectrum. The arrows show the nominal squared mass of the Σ^+ hyperon.

This fitting procedure, can not be used to extract the number of Σ^+ events in the lower energy data set. Here a Σ^+ peak is not seen on the missing mass distribution. It is expected in the region of a strong decrease of the counting rate, very close to the kinematical limit (see figure 2.28). In order to extract the number of Σ^+ events it was assumed that the background shape is the same as in the higher energy case. This assumption is based on the fact, that the form of the simulated missing mass distributions expected in the background (first five channels listed in table 2.2) does not change (within the error bars) for both beam momenta. Therefore from the experimental missing mass distribution for the higher energy data set, by subtracting the expected MC missing mass spectrum for the $pp \to nK^+\Sigma^+$ reaction, the background shape (i.e. without the Σ^+ hyperon events) was determined. Next it was shifted such, that the kinematical limits for both spectra, were the same. Afterwards, together with the missing mass distribution of the $pp \to nK^+\Sigma^+$ reaction extracted by MC studies, the background determined from the 2.74 GeV/c data was fitted to the experimental missing mass spectrum for the lower energy. In figure 2.31a the result of this procedure is shown. In figure 2.31b the result of the subtraction of the assumed background shape from the experimental missing mass distribution is depicted together with the simulated missing mass. Only events from the $\pm$ 0.5 σ region around the K^+ mass on the invariant mass distribution are shown.

[13] Error for the bin i in the experimental missing mass spectrum (ΔN_i^{EXP}) and the assumed background distribution (ΔN_i^{FIT}) was taken as a square root of the bin content. After the subtraction the errors are calculated such, that $\Delta N_i = \Delta(N_i^{EXP} - N_i^{FIT}) = \sqrt{(\Delta N_i^{EXP})^2 + (\Delta N_i^{FIT})^2} = \sqrt{N_i^{EXP} + N_i^{FIT}}$.

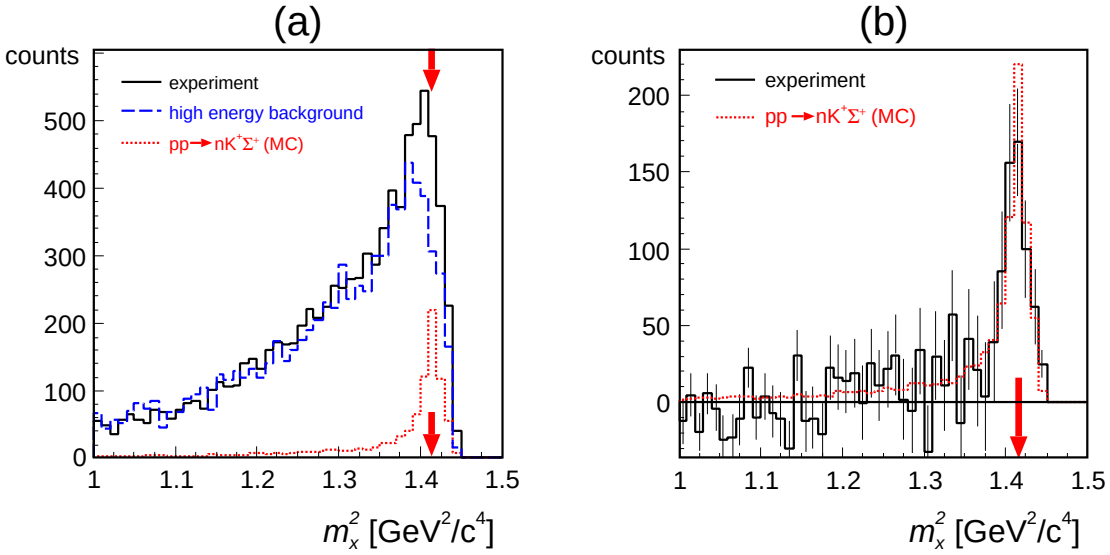

Figure 2.31: Background investigation for the $pp \to nK^+\Sigma^+$ reaction at $P_{beam} = 2.6$ GeV/c. (a) the experimental squared missing mass spectrum of the $pp \to nK^+X$ system compared to the assumed background and the simulated $pp \to nK^+\Sigma^+$ distribution. (b) result of the subtraction of the fitted background from the experimental distribution compared to the simulated spectrum. Arrows show the nominal squared mass of the Σ^+ hyperon. Errors were calculated in the same way as for the higher energy case.

As a cross check, other reaction channels of the type $pp \to ppX$ have been selected from the experimental data. In the first step events with at least two separated tracks reconstructed from the drift chamber signals (called *two-track events*) were selected and the distribution of the invariant mass of the first particle versus the invariant mass of the second one was plotted (see figure 2.32). Particles of different kind, i.e. protons, kaons and pions are well separated and can be clearly identified.

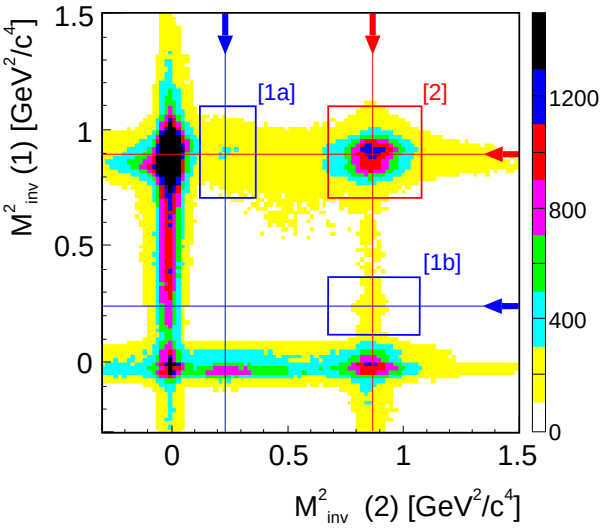

Figure 2.32: Distribution of the squared invariant mass of the first reconstructed particle (M^2_{inv} (1)) versus the second one (M^2_{inv} (2)) from a two-track events data sample at $P_{beam} = 2.6$ GeV/c. The arrows point to the nominal squared mass of proton and kaon.

Next, events with two protons in the exit channel were selected (region [2] in figure 2.32) and the squared missing mass spectrum m_x^2 of the $pp \rightarrow ppX$ system was generated (figure 2.33a). The presence of π^0 and η is clearly visible and their peak positions correspond to the known masses of these mesons. Furthermore events of the type $pp \rightarrow pK^+X$ were selected. Here events from the regions [1a] and [1b] in figure 2.32 were taken. In the [1a] region the first reconstructed track is considered as being a proton and the second track as being a kaon and in [1b] it is vice versa. The corresponding missing mass distribution is shown in figure 2.33b.

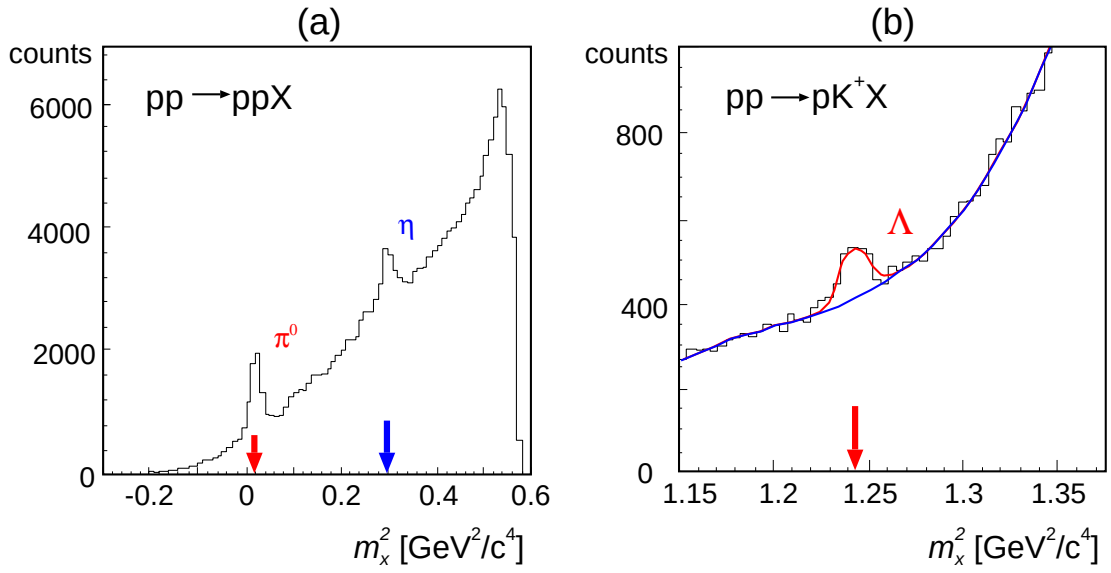

Figure 2.33: The squared missing mass distribution for: (a) the $pp \rightarrow ppX$ system and (b) the $pp \rightarrow pK^+X$ system. The two-tracks events from the lower energy data set are selected. Arrows show nominal masses of η and π^0 mesons and Λ hyperon.

In figure 2.33b a Λ peak resulting from the $pp \rightarrow pK^+X$ reaction is visible and also here the peak position is consistent with the nominal Λ hyperon mass. The number of Λ hyperon events was determined under the assumption, that the background shape under the Λ peak is smooth and the cross section for $pp \rightarrow pK^+\Lambda$ channel was calculated. The data sample presented in figure 2.33b corresponds to the excess energy $Q = 88.2$ MeV. The cross section for this channel is known for $Q = 59.3$ MeV [9] and $Q = 150$ MeV [65]. The interpolation to 88.2 MeV excess energy as a check of the luminosity calculations was done. The cross section for the $pp \rightarrow pK^+\Lambda$ channel was extracted to be about 8.5 ± 2.0 μb and fits very well into the systematic of the measured excitation function, see section 3.1, figure 3.3.

Remarks about detecting the decay of Σ^+

The $pp \to nK^+\Sigma^+$ reaction could be identified also via the decay products of the Σ^+ hyperon. It decays with $c\tau = 2.4$ cm [2], i.e. before entering the dipole gap. In figure 2.34 a sketch of the detection in the COSY–11 set-up is shown for the two main decay channels of the Σ^+ produced via the $pp \to nK^+\Sigma^+$ reaction. The Σ^+ hyperon decays into $p\pi^0$ and $n\pi^+$ with the branching ratios of 51.57 % and 48.31 %, respectively [2].

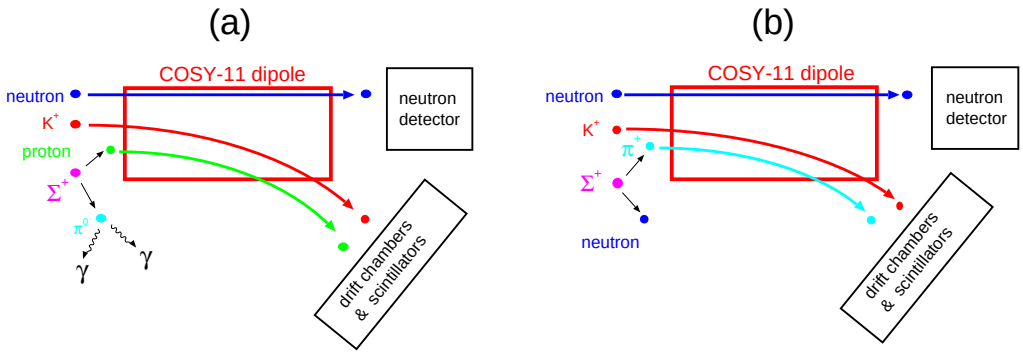

Figure 2.34: The principal sketch of the identification of the $pp \to nK^+\Sigma^+$ channel via the decay products of the Σ^+ hyperon in the COSY–11 detection system. Only two, the most probable decay channels are depicted [2], namely the case when the Σ^+ decays into proton and π^0 meson (a) and when it decays into neutron and π^+ (b).

In the first case the studied reaction can be identify through the signal given by the neutron in the neutron detector and both primary kaon and decay proton in the scintillators and drift chambers set. The π^0 meson decays immediately (with $c\tau = 25$ nm) into two γs and their efficient detection in the COSY–11 detection set-up is not foreseen. Therefore in the experimental missing mass distribution of neutron, kaon and proton, an enhancement around the mass of the π^0 meson is expected. Number of events under this peak, and detection efficiency determined for this channel would allow to calculate the cross section of the $pp \to nK^+\Sigma^+$ reaction.

In the decay into $n\pi^+$, in principle, all reaction particles, i.e. the primary (kaon and neutron) and the secondary (neutron and π^+) can be detected, and the $pp \to nK^+\Sigma^+$ channel can be reconstructed completely. However, the detection and separation of two neutrons in the COSY–11 neutron detector is not a reasonable approach. It would be more favorable to identify the second neutron via the missing mass analysis. Then the number of registered events combined with the detection efficiency make the cross section calculation possible.

On the basis of MC studies, the $pp \to nK^+\Sigma^+$ reaction identification via the Σ^+ hyperon decay products is extremely time consuming, since the detection efficiency for this *identification scenario* is about three orders of magnitude smaller than for the detection of only the primary neutron and kaon. From the MC studies it is expected to register only a few Σ^+ events within the data taking time period of the measurement as the one described in this thesis. However, for a detector with much larger acceptance in the full solid angle range, the possibility to register the decay products of the Σ^+ provides the unique opportunity to have almost background free identification of the studied reaction.

2.4.4 Luminosity determination

Precise knowledge of the luminosity is essential for the determination of the absolute total and differential cross sections of the studied reactions. The luminosity $\mathcal{L}$ is defined as the number of particles in the beam, hitting the target per second multiplied by the number of target particles per cm^2. The number of reactions per time unit (dN/dt) is given by the luminosity $\mathcal{L}$ multiplied by the corresponding cross section σ. The number of registered events per reaction channel (N) in the entire measurement period (T) can be determined by the combination of the integrated luminosity $\mathcal{L}_{int} = \int_0^T \mathcal{L}$, and the cross section σ. Therefore the integrated luminosity can be obtained from the following equation:

$$\mathcal{L}_{int} = \frac{N}{\sigma \cdot E_{eff}}, \tag{2.12}$$

where E_{eff} is the efficiency of the detection system.

In the COSY–11 experimental p-p studies, the luminosity is determined via the proton-proton elastic scattering [31, 46]. This channel has several advantages: *i*) the number of elastically scattered protons is relatively high, *ii*) the event selection is easy due to the two body kinematics and *iii*) the cross section of proton-proton elastic scattering is well known [66].

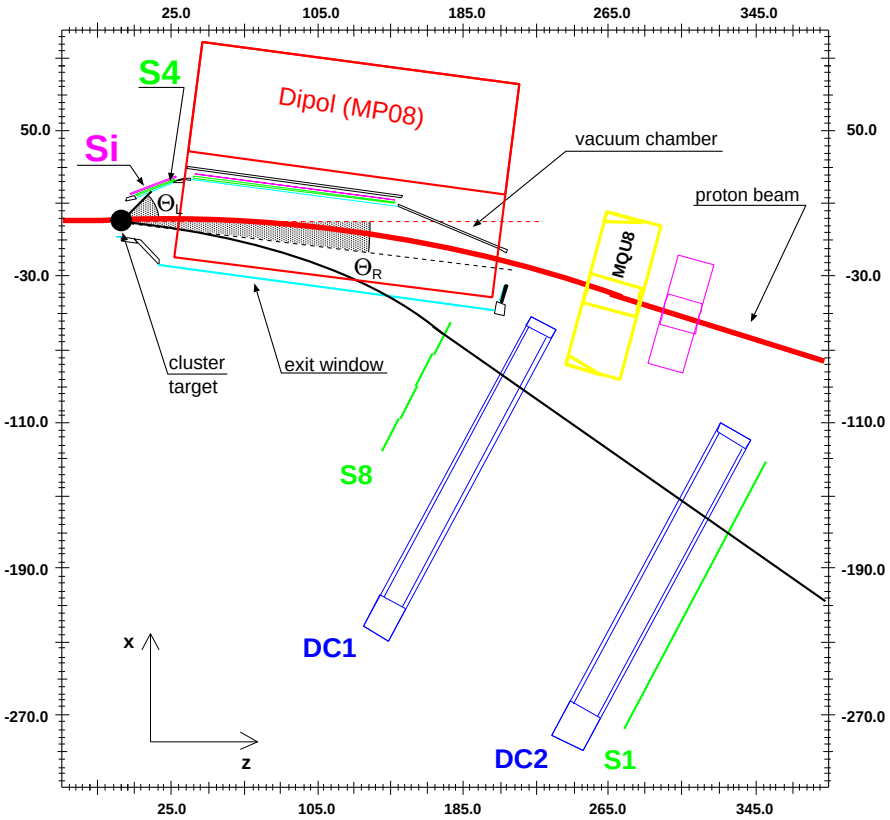

Figure 2.35: Sketch of the COSY–11 detection system with a superimposed example of the elastically scattered protons. The S1 scintillator as well as S4 and silicon monitor detector are depicted in detail in figures 2.38 and 2.39.

The proton-proton elastic scattering was measured simultaneously with the Σ^+ production reaction at both beam momenta . On the hardware trigger level an event was recognized as a candidate for being an elastically scattered proton when it gave a signal in the S4 and in one of the S1 scintillators (see figure 2.35).

One out of the two protons in the elastic channel with the scattering angle Θ_R (see figure 2.35) is bent by the magnetic field of the dipole towards the inner part of the COSY ring. In what follows this particle will be called *right*. Its momentum is determined by tracking the trajectory reconstructed from signals registered in the drift chambers DC1 and DC2 through the magnetic field back to the target point. The second particle (scattered by the angle Θ_L, and called $left$) is registered in the S4 scintillator (which contributes to the trigger signal) and in a position sensitive silicon pad detector.

Off-line analysis is needed for a clean separation of background channels from the registered signals. The first step of the analysis is the identification of the *right* proton by the invariant mass determination. The known momenta of the protons in the beam and in the target as well as of the *right* proton in the exit channel enable to determine the missing mass of the $left$ particle. In figure 2.36 the invariant mass and the missing mass distributions of events selected by the elastic hardware trigger at a beam momentum of $P_{beam} = 2.74$ GeV/c are given. The background in these distributions is caused mainly by the $pp \rightarrow pn\pi^+$ reaction. The events from the hatched regions in figure 2.36 were assumed to be protons, and were taken into further analysis.

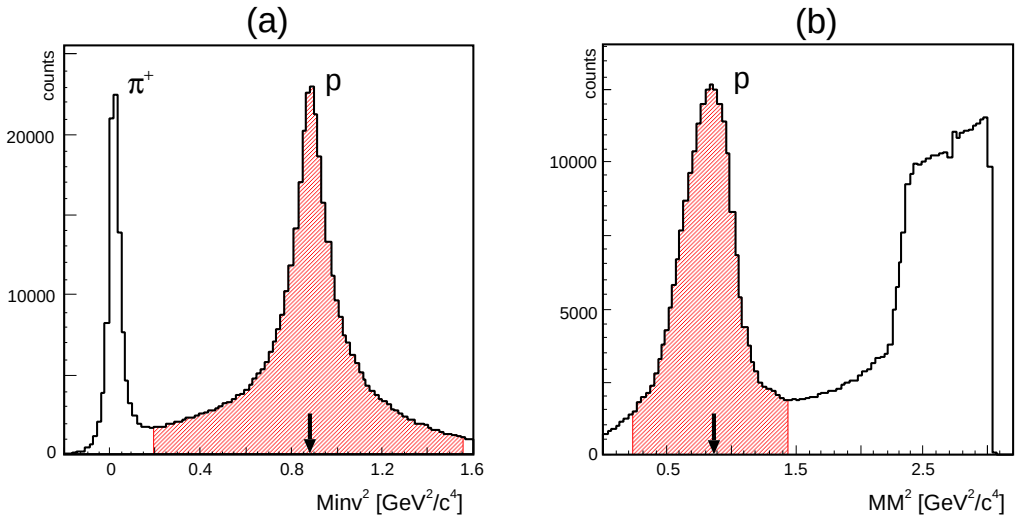

Figure 2.36: In (a) the squared invariant mass distribution of the *right* – bended in the dipole – particle is shown. In (b) the missing mass distribution of the $left$ particle is given. Arrows show the nominal squared mass of proton.

In two body kinematics the total momentum of the ejectiles is fixed in the center of mass system (CMS) and the events are located on a circle in a P_L^* (momentum in beam direction) vs. P_T^* (momentum perpendicular to the beam direction) distribution. The transformation into the laboratory system results in an ellipse in the P_L vs. P_T plane [67,68] given by: $P_T = P_T^* \quad$ and $\quad P_L = P_L^* \cdot \gamma - E \cdot \beta \cdot \gamma$, which can be used for the background suppression. In figure 2.37 the correlation of the reconstructed momentum

components are shown together with the kinematical circle for the measurement at higher beam momentum.

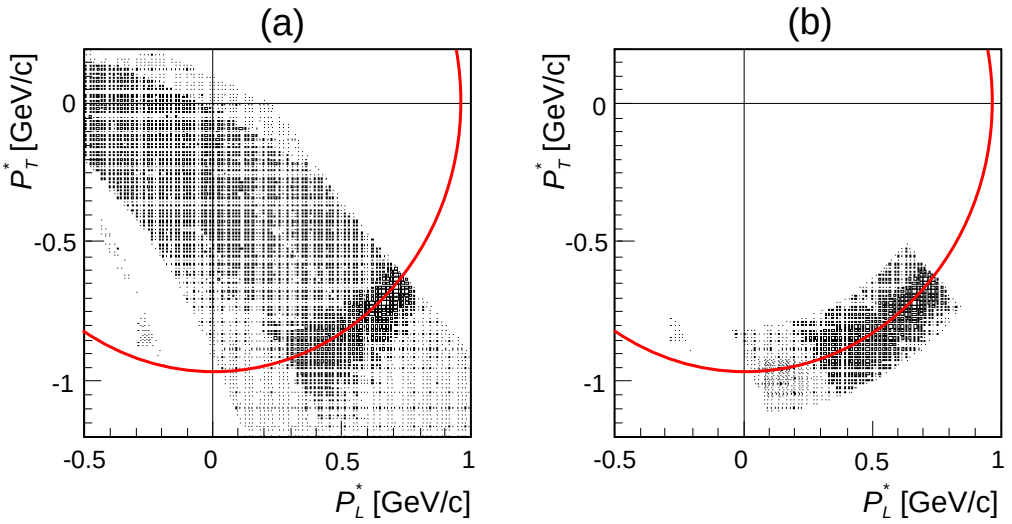

Figure 2.37: The correlation between the perpendicular P_T^* and parallel P_L^* to the beam direction components of the total momentum in the center of mass frame. (a) all events selected by the elastic hardware trigger are shown. (b) the events left over after the cuts on the invariant mass (for particle $right$) and missing mass (for particle $left$) are shown (see text for details). The event sample measured at the beam momentum of $P_{beam} = 2.74$ GeV/c is presented.

In order to reduce the non-elastic background a cut on the kinematical circle was done and events within a $\pm 3\sigma$ region (the distribution can be fitted by a Gauss function) around the momentum sphere expected from kinematics were taken into further analysis.

In two body kinematics the laboratory scattering angles Θ_R and Θ_L are related by:

$$tg\Theta_R \cdot tg\Theta_L = \frac{1}{\gamma_{cm}^2}, \tag{2.13}$$

where γ_{cm} is the Lorentz factor for the center of mass system [14]. Therefore an angular correlation between positions in silicon pad detector (Si) and S1 scintillator for the elastically scattered protons is expected.

Since the S1 scintillator is not position sensitive within the individual S1 modules, the crossing point of the scattered particle track (determined by using the drift chambers) and the S1 plain is taken to check the correlation (see figure 2.39). The position at the silicon pad detector is given by the pad number. As described in the section 2.2.2 the Si detector consists of 12 elements by 4 pads each with a width of 4.5 mm (see figure 2.38).

[14] The most general definition of the Lorentz factor for the center of mass system is $\gamma_{cm} = |\vec{P}_{beam} + \vec{P}_{target}|/(E_{beam} + E_{target})$, where P and E denote the total momenta and energies, respectively. In case of a fixed target experiment and equal masses of the beam and target particles the Lorentz factor definition is simplified: $\gamma_{cm} = P_{beam}/(E_{beam} + m)$, where m is the proton mass.

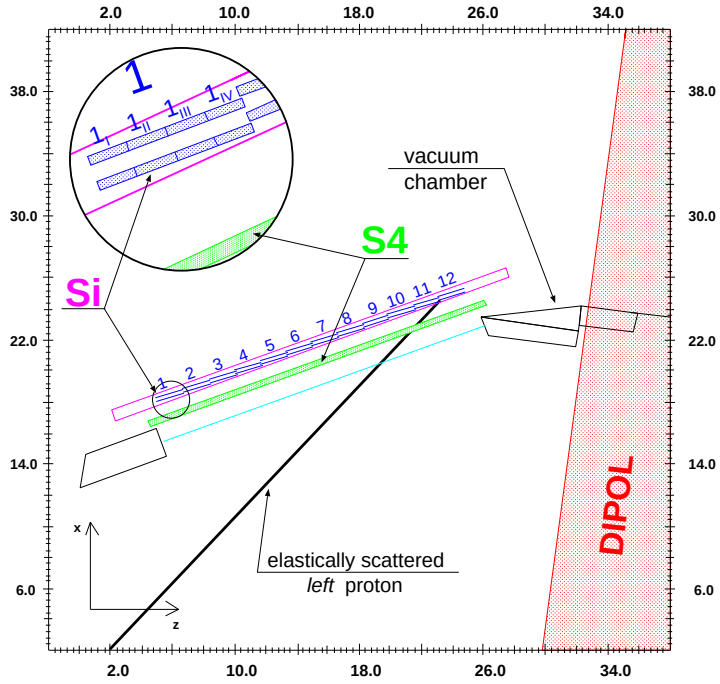

Figure 2.38: Detailed drawing of the Si detector and S4 scintillator region with a track of a scattered $left$ proton. The position of the scattered particle is taken as the center of the hit pad. The S4 scintillator located in front of the Si detector provides the fast trigger signal.

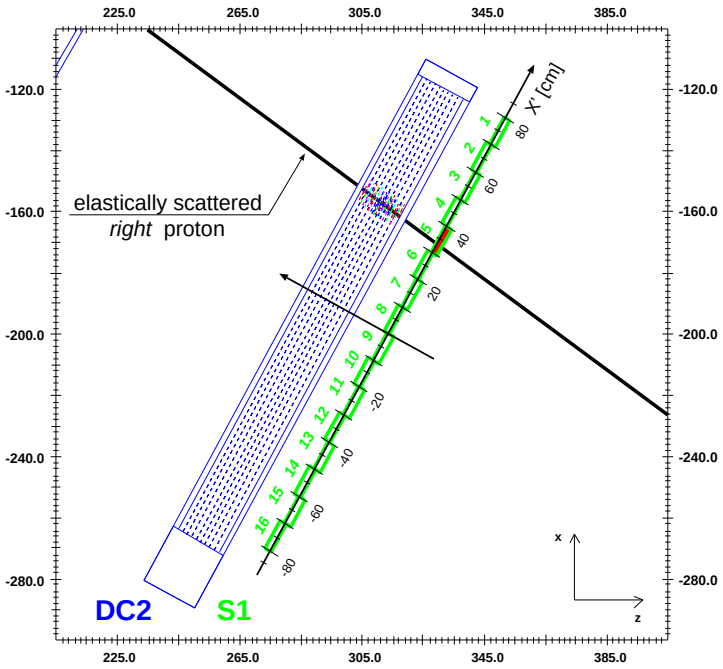

Figure 2.39: Detailed drawing of the S1 detector region with a typical track of a scattered $right$ proton. The two drift chambers DC1 and DC2 give the particle track from which the position of the scattered proton at the S1 scintillator is determined.

In figure 2.40 the correlation between the position measured in the S1 scintillator and the position in the Si detector (pad number) is shown. To select elastic events the deviation from the correlation curve given by a straight line fit is determined for each event. Events from a $\pm 3\sigma$ region (the area between two black lines in figure 2.40) were taken for further analysis.

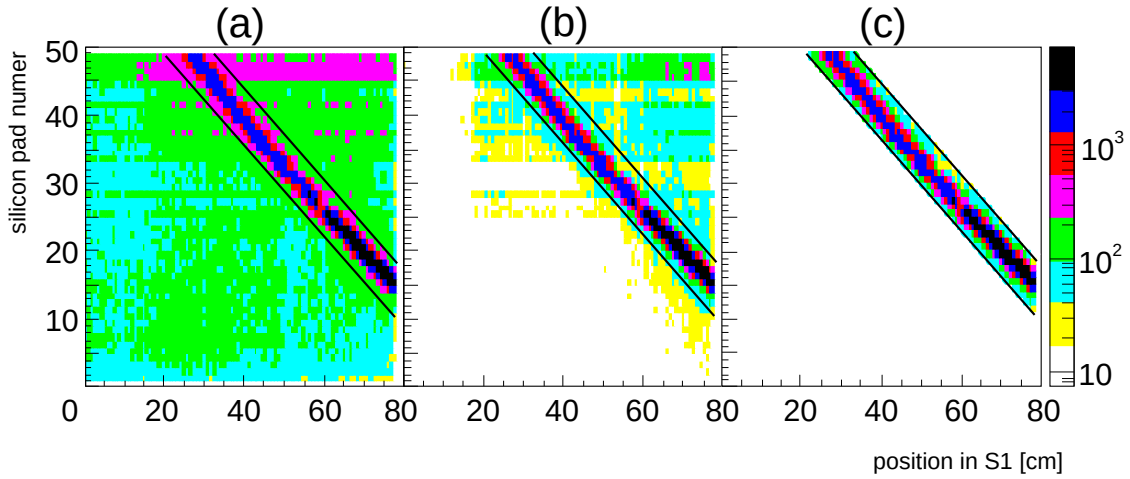

Figure 2.40: Position of the *right* particle in S1 scintillator against the position (pad number) of the *left* one in Si pad detector. (a) events selected only by hardware elastic trigger, (b) events which are left over after applying the cuts on the invariant and missing mass spectra, (c) events within a $\pm 3\sigma$ width of the Gaussian describing the distribution of distances from the correlation line (cuts described in figures 2.36 and 2.37 are applied). The data sample shown on these plots was measured at the beam momentum of $P_{beam} = 2.74$ GeV/c. Note the logarithmic scale of the intensity distribution.

To determine the luminosity, the experimentally known differential cross section for elastically scattered protons [66] $\frac{d\sigma}{d\Omega^*}$ (where the CMS solid angle $d\Omega^*$ is given as $d\Omega^* = sin\Theta^* d\Theta^* d\varphi^*$) is compared to the number of scattered protons N from the experimental data. In figure 2.41 the angles Θ^* and φ^* are defined, where Θ^* is the scattering angle in the projection onto the xz plain and the z axis. The angle φ^* is the angle between the projection on the xy plain and the x axis. For the unpolarized beam the cross section is only dependent on Θ^*. Therefore the elastic events are sorted in values of Θ^*. Due to geometrical constraints in the COSY–11 detection set-up the elastically scattered protons reach the S1 scintillator from about 25 cm to 80 cm in the DC2 reference frame. It corresponds to a Θ^*_R [15] angular range from about 42° to 69°. This range was divided into 13 bins with a width of 2° each.

[15] The Θ^*_R corresponds to the Θ_R in laboratory system from figure 2.35.

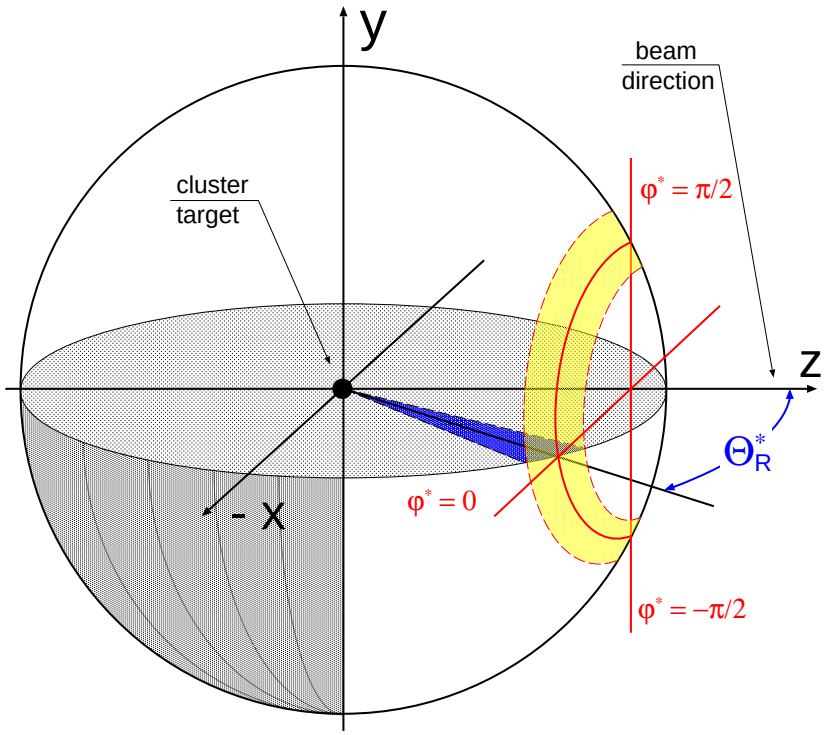

Figure 2.41: Geometrical relations between the angles Θ^*_R and φ^*. The coordinate system on the picture is identical with the COSY–11 target frame. The description of the particular regions (marked in different colors) can be found in the text.

In order to determine the effective solid angle for each $\Delta\Theta^*$ bin, elastic events are generated with an isotropic distribution in the COSY–11 Monte Carlo program. The same $\Delta\Theta^*$ bins used for the experimental data are filled and the ratio of accepted events in a certain $\Delta\Theta^*$ bin to the generated events number gives the effective solid angle $\Delta\Omega_{eff}$. The luminosity $\mathcal{L}_{int}$ in a certain angle bin $\Delta\Theta^*$ can be calculated from the formula:

$$\mathcal{L}_{int} = \frac{N(\Omega^*)}{\frac{d\sigma}{d\Omega^*} \cdot \frac{\Delta\Omega_{eff}}{2}}, \tag{2.14}$$

where the factor 2 is due to the scattering of two identical particles.

In figure 2.42 the projection of the distribution of the distances to the straight line fitted to the spectrum shown in figure 2.40 is depicted. The number of events under this peak (after background subtraction) gives the number of elastically scattered protons registered by the COSY–11 detection set-up in the range of $42^\circ \leq \Theta^*_R \leq 44^\circ$. The not well determined background shape under this peak introduced a significant contribution to the systematical error. After applying all cuts described in this section, the ratio of *non elastic background events* to *elastic events* was smaller than one to hundred. As it was shown in previous studies, this contribution ranges from values as low as 0.2 % [31] to 0.3 % [57] of the number of elastic events. In this work the systematical error due to the background subtraction is assumed to be **0.25 %** for both beam momenta.

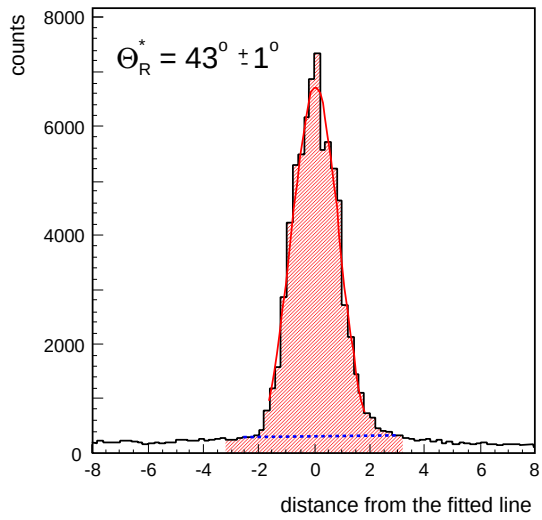

Figure 2.42: The distribution of the distances from the correlation line for the events from figure 2.40(b) for $\Theta^*_R = 43° \pm 1°$. Red solid line shows the fitted Gaussian distribution, blue dotted line depicts the estimated background and the hatched area corresponds to the region of $\pm 3\sigma$.

For each of the 13 bins of the Θ^*_R distribution, the projection of the distance from the correlation line (position in S1 scintillator versus Si silicon pad number) was extracted, the background was subtracted and the number of events was obtained. The elastically scattered protons in the MC simulations are generated with a homogeneous phase space coverage. Comparing the number of generated events in a certain angular range $\Delta\Theta^*$ to the number of registered events, one can determine (for each bin in Θ^*_R) the effective solid angle for the elastic scattered protons just by MC calculations.

In figure 2.43 the luminosities for each of the 13 Θ^*_R bins are presented. Within the error bars (only the statistical errors are shown) all calculated values are consistently constant. The statistical errors for the higher momentum measurement are slightly larger, because of the shorter beam time.

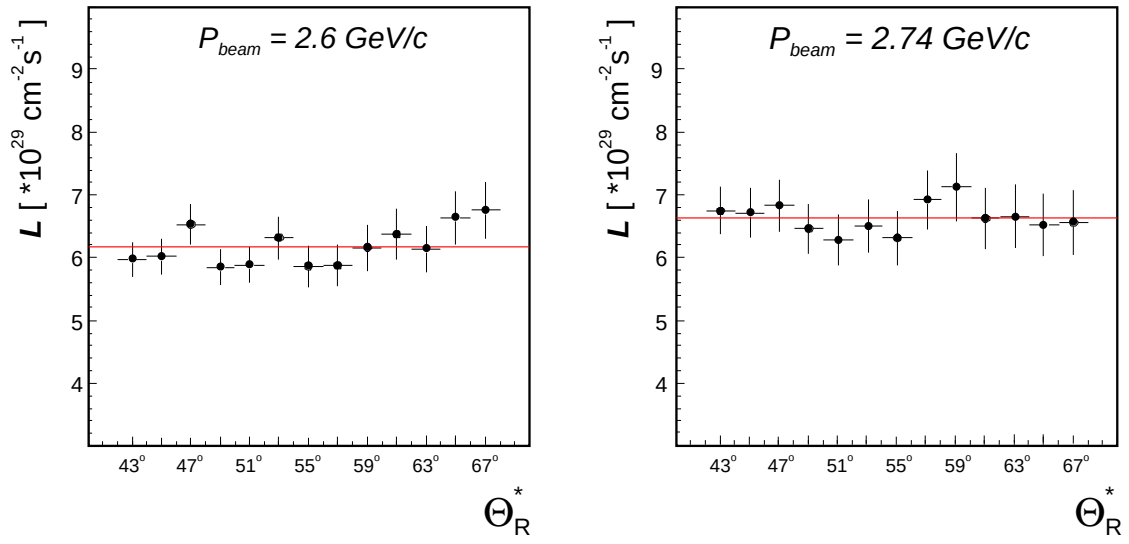

Figure 2.43: The luminosity as a function of Θ^*_R for $P_{beam} = 2.6$ GeV/c and $P_{beam} = 2.74$ GeV/c. The red straight line shows the average value for the whole measurement period.

The proton–proton elastic scattering cross sections as given by [66] have a systematical uncertainty in the order of 1 % due to the normalization procedure and a systematical error of the $\Delta\Omega^*$ solid angle determination of about 2 % [31].

The total systematical error of the luminosity determination (including the error due to the background subtraction) sum up quadratically to a value of **2.25 %** for both beam momenta.

Table 2.3 summaries the calculated average luminosities over the whole Θ^*_R region (as shown in figure 2.43 by the red line) as well as statistical and systematical errors for both beam momenta.

Table 2.3: Average luminosities for two beam momenta.

Beam momentum P_{beam} $[GeV/c]$	Average luminosity $\mathcal{L}$ $[10^{29} cm^{-2} s^{-1}]$
2.6	$6.14 \pm 0.10 \pm 0.14$
2.74	$6.63 \pm 0.13 \pm 0.15$

Chapter 3

Results and conclusions

3.1 Total cross section

In sections 2.4.1 and 2.4.2 the determination of the kaon and neutron four-momenta was presented and also the cuts applied in the off-line analysis were discussed and justified. In section 2.4.3 the missing mass method was introduced and the extensive background studies were described. As a result the method to determine the number of Σ^+ events for both beam momenta was given. In this section the statistical studies are presented and the cross section values for both beam momenta calculated.

Higher energy case

For the higher momentum a kaon peak on the invariant mass distribution is clearly visible (see figure 2.23) and can be fitted by a Gaussian function. The mean value μ_{exp} of this fit and the peak width σ_{exp} was determined to be 0.2463 GeV^2/c^4 and 0.055 GeV^2/c^4, respectively. In the MC distribution the width of the kaon peak (σ_{mc}) is 0.053 GeV^2/c^4, and the mean value of a Gaussian fit corresponds to the nominal squared kaon mass, namely $\mu_{mc} = 0.2437$ GeV^2/c^4. In a systematical study three different cuts on the experimental invariant mass distribution were applied. Events from these regions, namely: $\mu_{exp} \pm 0.25\sigma_{exp}$, $\mu_{exp} \pm 0.5\sigma_{exp}$ and $\mu_{exp} \pm 1.0\sigma_{exp}$ were taken and the corresponding missing mass distributions were generated. Next the number of Σ^+ events for each of these distributions was determined. The results are listed in the middle column of table 3.1 and in the last column the number of the Σ^+ events corresponding to the full Gaussian distribution by scaling with the factor C [1] is given.

The number of Σ^+ events was determined from a fit of the MC Σ^+ distribution added to a background to the experimental distribution. The errors in table 3.1 are given by the statistics as described in section 2.4.3. In order to check the errors of the Σ^+ event numbers a χ^2 analysis was performed. The errors resulting from the χ^2 distribution of the fit were about 20 % in agreement with the errors calculated from the statistics. For

[1] The scaling factor C is defined as

$$C = \frac{\int_{-\infty}^{\infty} f(x)dx}{\int_{-\Delta x\sigma_{exp}}^{\Delta x\sigma_{exp}} f(x)dx},$$

where $f(x)$ is a Gauss function ans $\Delta x = 0.25$, 0.5 and 1.0.

further investigations the average number of events resulting from the scaled Σ^+ event numbers was taken.

Table 3.1: The number of Σ^+ events for the higher energy case. Only statistical errors are given.

Invariant mass cut μ_{exp}	Number of events identified as Σ^+	Number of events identified as Σ^+ and scaled by the factor C
$\pm$ 0.25 σ_{exp}	187 $\pm$ 51.0	944.4 $\pm$ 257.6
$\pm$ 0.5 σ_{exp}	367 $\pm$ 83.2	960.7 $\pm$ 217.8
$\pm$ 1.0 σ_{exp}	661 $\pm$ 134.5	969.2 $\pm$ 197.2
	average	**958.1 $\pm$ 224.2**

Lower energy case

For the lower energy data set the assumption has to be made that here the background shape in the missing mass distribution is the same as for the higher beam momentum case. After applying all cuts, there was no enhancement around the kaon mass in the invariant mass distribution, and therefore the additional assumption was made, that the kaon peak in the experimental distribution has the same position (μ_{mc}) and width (σ_{mc}) as in the simulated distribution. In order to extract the number of Σ^+ hyperons observed, events from a $\pm 0.5\sigma_{mc}$ region around the kaon mass in the invariant mass distribution were taken. The total number of events in the lower energy case is given in table 3.2.

Table 3.2: The number of Σ^+ events for the lower energy case. Only statistical errors are given.

Invariant mass cut μ_{mc}	Number of events identified as Σ^+	number of events identified as Σ^+ and scaled by the factor C
$\pm 0.5\sigma_{mc}$	811 $\pm$ 165.	2124. $\pm$ 432.

As a cross check, event samples with a cut on different regions but still within the kaon range in the experimental invariant mass distribution were taken and the missing mass was determined. The assumed background shape was subtracted from the experimental distribution and the enhancement around the mass of the Σ^+ was interpreted as a signal from the Σ^+ hyperon (see figure 2.31). This procedure was repeated for five different invariant mass regions and the number of events under the remaining peak was determined. The results are shown in figure 3.1. The vertical error bars correspond to the statistical error of the number of events. The horizontal error bars show the widths of the appropriate invariant mass cuts which have been chosen as half of the standard deviation of the kaon peak for the data sample of $pp \to nK^+\Sigma^+$ channel simulated with lower beam momentum.

The $\pm 0.5\sigma_{mc}$ cut around the squared kaon mass on the invariant mass distribution yields 811 $\pm$ 165 of Σ^+ events from the missing mass distribution. It means that within the same region 811 $\pm$ 165 kaons from $pp \to nK^+\Sigma^+$ reaction are expected. Therefore the distribution of the number of Σ^+ events as a function of invariant mass cut can be interpreted as a distribution of number of kaons from the studied channel. In figure 3.1 curve (1) shows the expected invariant mass distribution of kaons from MC calculations with a mean value μ_{mc} and a width σ_{mc}. Curve (2) is a Gauss fit to the experimentally determined number of Σ^+ events in the different invariant mass regions. This can be

interpreted as an experimental distribution of kaons. The assumed experimental kaon invariant mass distribution is in line with the distribution expected from MC studies. The mean value and the width of the Gauss function fitted to the distribution of Σ^+ events is $\mu_{exp} = 0.247$ GeV^2/c^4 and $\sigma_{exp} = 0.0415$ GeV^2/c^4, respectively. This can be compared to the mean $\mu_{mc} = 0.2437$ GeV^2/c^4 and width $\sigma_{mc} = 0.0375$ GeV^2/c^4 obtained from MC studies.

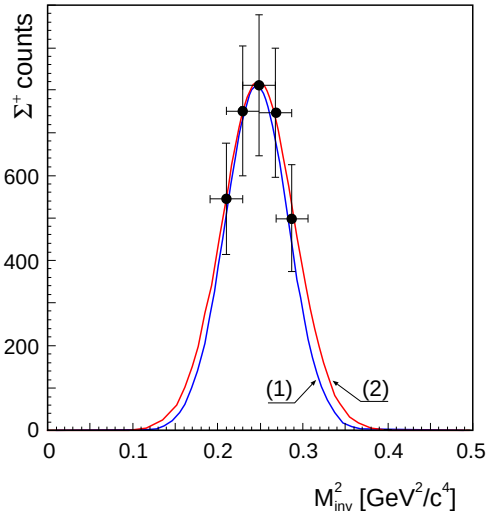

Figure 3.1: The number of Σ^+ events obtained for different regions of the invariant mass cut. Curve (1) – expected from the MC studies distribution of the K^+ events. Curve (2) – Gaussian fit to the points on the figure given by the number of Σ^+ events. See text for details.

Cross sections calculations

In order to calculate the cross section for the $pp \to nK^+\Sigma^+$ reaction the average number of Σ^+ hyperon events N given for the two excess energies in tables 3.1 and 3.2 are taken. Next, the information about the detection efficiency E_{eff} of the COSY–11 apparatus was determined (table 2.1). The luminosity $\mathcal{L}$ from table 2.3 was integrated over the time of the experiment and the integrated luminosity $\mathcal{L}_{int}$ was calculated. Having all these variables the total cross section σ can be calculated:

$$\sigma(Q) = \frac{N}{\mathcal{L}_{int} \cdot E_{eff}} \tag{3.1}$$

In table 3.3 the total cross sections for both beam momenta are given together with the statistical and systematical errors. There are several sources of systematical errors i.e.

- error of the detection efficiency determination which is 7.57 % for the lower and 2.69 % for the higher energy data set (see section 2.3.3),
- error of the luminosity calculation which is 2.25 % for both data sets (see section 2.4.4).

The quadratic sum of systematical errors is **7.9 %** for the lower and **3.5 %** for the higher energy data. These values do not include the possible error in the detection efficiency resulting from the inclusion of higher partial waves, what was described in detail in section 2.3.3.

Table 3.3: Values of the total cross section for the $pp \to nK^+\Sigma^+$ reaction obtained in the present work. Both, statistical and systematical errors are given.

Beam momentum P_{beam} $[GeV]$	Excess energy Q $[MeV]$	Total cross section σ $[nb]$
2.6	13	$4559.7 \pm 940.9 \pm 359.8$
2.74	60	$44812.0 \pm 10687.9 \pm 1573$

As a check of the luminosity calculation, the cross section of the $pp \to pK^+\Lambda$ reaction channel was extracted from the data at an excess energy of $Q = 88.2$ MeV. The number of Λ hyperon events was determined from the missing mass spectrum of the $pp \to pK^+X$ system (see section 2.4.3). In [57] the detection efficiency E_{eff} as a function of excess energy Q up to 60 MeV is given for this channel and by an extrapolation to the excess energy of $Q = 88.2$ MeV the efficiency of the COSY–11 apparatus was determined, ($E_{eff} = 2.84 \cdot 10^{-2}$ %). With the luminosity given in table 2.3, the total cross section for the $pp \to pK^+\Lambda$ reaction was calculated from equation 3.1. The obtained value is $\sigma = 8492 \pm 1974$ nb, which is in a very good agreement with the lower and higher energy data for this channel (see figure 3.3).

3.2 Comparison with model predictions

Among the models described in the *Introduction* only two give predictions for the reaction channel investigated in this thesis, namely the *Jülich meson exchange model* [18, 19] and the *resonance model* [15, 17].

Jülich meson exchange model predictions

Within the *Jülich meson exchange model* the large cross section ratio $\sigma(\Lambda)/\sigma(\Sigma^0)$ at threshold is reproduced by a destructive interference of π and K exchange amplitudes (see figure 1.4). Calculations of the Σ^+ production in this model predict a factor of three higher cross section compared to the Σ^0 channel for a destructive and a factor of three lower for a constructive interference. This means that for the $pp \to nK^+\Sigma^+$ reaction channel measured at $Q = 13$ MeV the total cross section is supposed to be $\sigma_{Q=13} = 229$ and 86 nb for destructive and constructive interference, respectively. For excess energies above 20 MeV this model is not valid any more why the predictions are only available for the lower data point of investigated reaction. The cross section ratio $\sigma(pp \to nK^+\Sigma^+)/\sigma(pp \to pK^+\Sigma^0)$ is expected to be about 0.34 for the constructive and about 3.1 for the destructive pion/kaon interference [18]. In figure 3.2 the predictions of *Jülich meson exchange model* for the $pp \to nK^+\Sigma^+$ and $pp \to pK^+\Sigma^0$ channels are shown together with data points close to threshold.

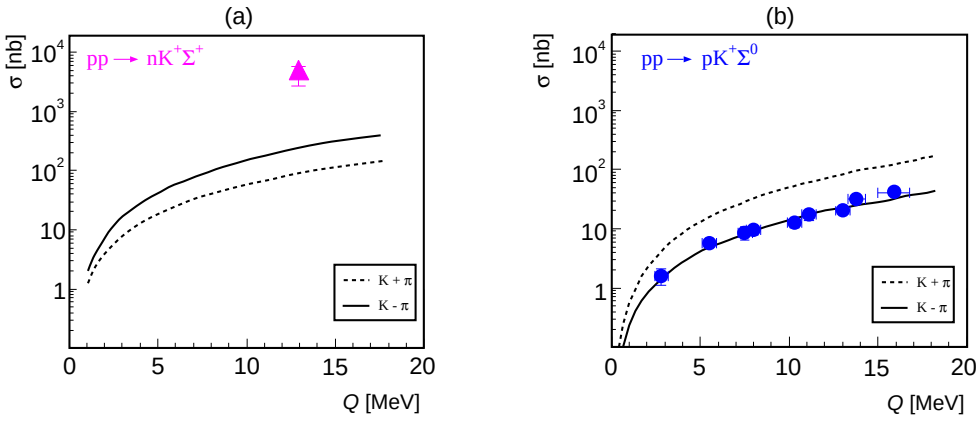

Figure 3.2: Comparison of the experimental total cross section for : (a) the $pp \to nK^+\Sigma^+$ reaction (data point at $Q = 13$ MeV obtained in this thesis), (b) the $pp \to pK^+\Sigma^0$ reaction [7, 8] with predictions of the *Jülich meson exchange model* [18]. Calculations represent destructive (K$-\pi$) and constructive (K$+\pi$) interference between the π and K exchange contributions.

As it was mentioned in the *Introduction*, for the agreement with the data points, the model calculations for $pp \to pK^+\Sigma^0$ and $pp \to pK^+\Lambda$ channels had to be normalized by a factor of 0.3 and 0.25, respectively [18]. This is in agreement with the fact that the neglect of ISI in the $pp \to pp\eta$ channel results in an overestimation of the cross section by a comparable factor [21]. The prediction for the $pp \to nK^+\Sigma^+$ channel was normalized by the same factor as the $pp \to pK^+\Sigma^0$ channel. For the Σ^+ hyperon production the model prediction underestimate the total cross section by about a factor of 20 for the destructive and a factor of 53 for constructive interference. The ISI for the studied reaction is expected to be in the same order as for Λ and Σ^0 hyperon production.

Apart from the experimental data obtained in this thesis, table 3.4 comprises also the corresponding cross sections for the $pp \to pK^+\Lambda$ (Σ^0) channels and data for all three hyperon channels measured at high excess energy. These data have been used for the calculations of the experimental cross section ratios, which are given in table 3.5. From the comparison of the $pp \to nK^+\Sigma^+$ data point at low excess energy and the *Jülich meson exchange model* predictions (see figure 3.2), the conclusion can be drawn that the production mechanisms of π- and K-exchanges are not sufficient to explain the observed high cross section in this channel. This huge discrepancy does not allow to draw any conclusions about the general validity of this model [69].

Table 3.4: Values of the cross sections for the $pp \to pK^+\Lambda$ (Σ^0) [8, 9] and $pp \to nK^+\Sigma^+$ (this work) reactions for excess energies $Q = 13$ MeV and $Q = 60$ MeV together with the averaged high energy data [12, 65].

Excess energy Q $[MeV]$	Cross section σ $[nb]$		
	$pp \to pK^+\Lambda$	$pp \to pK^+\Sigma^0$	$pp \to nK^+\Sigma^+$
13	505 ± 33	20.1 ± 3.0	4559.7 ± 1300.7
60	3838 ± 624	482 ± 144	44812.0 ± 12260.9
$\geq$ 300	45000 ± 16248	18143 ± 12669	65800 ± 20131

Table 3.5: Values of the calculated cross section ratios for hyperon channels studied in COSY–11. The experimental cross sections are listed in table 3.4.

Excess energy Q $[MeV]$	Cross section ratio		
	$\frac{pp \to nK^+\Sigma^+}{pp \to pK^+\Lambda}$	$\frac{pp \to nK^+\Sigma^+}{pp \to pK^+\Sigma^0}$	$\frac{pp \to pK^+\Lambda}{pp \to pK^+\Sigma^0}$
13	9.0 ± 2.6	227 ± 73	25 ± 4
60	11.7 ± 3.7	93 ± 37.7	8 ± 2.0
≥ 300	1.5 ± 0.7	3.6 ± 2.8	2.4 ± 3.7

Resonance model predictions

For the *resonance model* calculations [15, 17], the predictions for the $pp \to nK^+\Sigma^+$ channel for the close to threshold region deviates even more from the data. Compared to the *Jülich meson exchange model* it is one order of magnitude lower. In figure 3.3 the model predictions and the available data for the $pp \to nK^+\Sigma^+$ (a), $pp \to pK^+\Sigma^0$ (b) and $pp \to pK^+\Lambda$ (c) channels are shown.

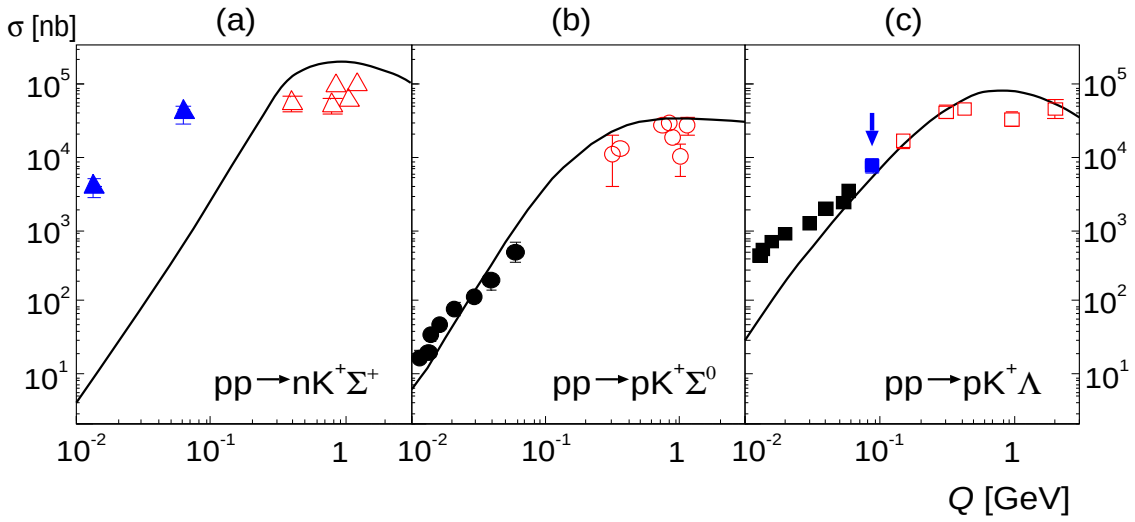

Figure 3.3: Comparison of the experimental total cross section with the *resonance model* [15, 17] predictions for various $pp \to NK^+Y$ reactions. Full triangles in (a) are data obtained in this thesis. Data in the close to threshold region (presented as full symbols in (b) and (c)) are taken from Refs. [7–9] and data from the high excess energy region (open symbols) from Refs. [12, 65]. In (c) the data point indicated by arrow was determined as a cross check of the luminosity calculations (see sections 2.4.3 and 3.1).

For the data point at $Q = 13$ MeV the underestimation of the calculated total cross section for the $pp \to nK^+\Sigma^+$ channel (see figure 3.3a) is about a factor of 500 and for $Q = 60$ MeV it is about 50. For the $pp \to pK^+\Sigma^0$ channel, the model calculation more or less describes the existing data set (see figure 3.3b). For the $pp \to pK^+\Lambda$ reaction channel (see figure 3.3c) the underestimation of the cross section given by the discussed model in the close to threshold region is about a factor of 30 smaller than for the $pp \to nK^+\Sigma^+$ reaction channel and amounts to about 16. But for excess energies above 50 MeV the Λ data are within error bars in agreement with the model predictions. However, in case of the $pp \to nK^+\Sigma^+$ channel the high energy data points are by a factor of 3–4 below the calculations.

Previous COSY–11 hyperon production studies conclude, that Final State Interaction (FSI) plays an important role in close to threshold Λ production [7–9]. In the *resonance model* the FSI is not included [15, 17] and therefore the deviation of the data points from the model calculations in close-to-threshold region is expected if a strong FSI is present. This effect is clearly seen for the $pp \to pK^+\Lambda$ (figure 3.3c) and barely observed for the $pp \to pK^+\Sigma^0$ reaction channel (figure 3.3b). For the Σ^+ hyperon production it is too early to draw reliable conclusion about the FSI due to the lack of data. The strong deviation of the two data points extracted within this thesis (figure 3.3a) from the model calculations can most likely not be interpreted as a pure effect of FSI since this discrepancy seems to be too large [69]. The observed disagreement would be even stronger if the model calculations for the $pp \to nK^+\Sigma^+$ reaction would be adjusted to the high energy data for this channel, however, this would also change the overall normalization in the other channels because all channels are related in the *resonance model* [70].

In a Dalitz plot analysis of the $pp \to pK^+\Lambda$ channel performed by the TOF collaboration [4] at excess energies $Q > 50$ MeV, a dominant contribution of resonance excitation was observed [5]. In the *resonance model* the intermediate baryonic resonances $N(1710)$, $N(1720)$, $N(1650)$ and $\Delta(1920)$ are taken into account for the explanation of the reaction mechanism, but the model shows strong deviations from the data. The *resonance model* predict that the cross section of the $pp \to nK^+\Sigma^+$ channel in the excess energy region up to about 100 MeV is about half of the cross section for the $pp \to pK^+\Sigma^0$ channel. In figure 3.4 the calculated and experimental cross section ratio $\sigma(pp \to nK^+\Sigma^+)/\sigma(pp \to pK^+\Sigma^0)$ are given. For $Q = 13$ MeV and 60 MeV the $pp \to nK^+\Sigma^+$ cross section is more than 200 and about 100 times higher than for the cross section of the $pp \to pK^+\Sigma^0$ channel, respectively. However, when summing up contributions of different resonances the phase in the coherent addition is unknown which can result in destructive or constructive interferences which may change the resulting cross section drastically.

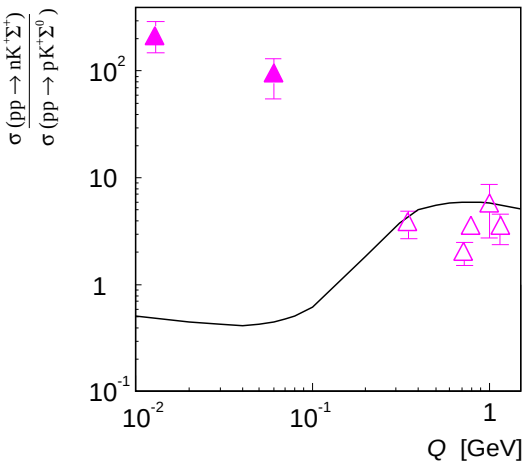

Figure 3.4: Experimental ratio of the total cross section for the $pp \to nK^+\Sigma^+$ and $pp \to pK^+\Sigma^0$ reaction as a function of the excess energy. The solid line represents the calculation within the *resonance model* [15, 17]. Full triangles – ratios calculated for data from Ref. [8, 9] and from this work. Open triangles – ratio obtained for data from Ref. [12].

Fäldt-Wilkin parametrisation

In previous COSY–11 studies of the hyperon production channels it was observed [7–9] that a pure 3-body Phase Space (PS) dependent cross section expressed as [67]:

$$\sigma = K \cdot Q^2, \tag{3.2}$$

where K is a normalization factor and Q the excess energy, can not describe the $pp \to pK^+\Lambda$ data, hence a modification taking the *proton-hyperon* FSI into account is needed. Therefore the parametrisation of the excitation function including the FSI proposed by Fäldt-Wilkin [11] was used. In this parametrisation the Coulomb interaction, which makes only a small effect in the considered kinematic region, is not included. Thus the *proton-hyperon* FSI is described in the same way as a *neutron-hyperon* interaction in the exit channel. The Fäldt-Wilkin parametrisation is expressed by:

$$\sigma = C \cdot \frac{Q^2}{(1+\sqrt{1+Q/\varepsilon})^2}, \tag{3.3}$$

where Q is the excess energy and C and ε are parameters related to the FSI strength.

In figure 3.5 the existing close to threshold data of Λ, Σ^0 and Σ^+ hyperon production are given and the curves corresponding to pure PS and PS modified by the (pY FSI), are shown. For the $pp \to nK^+\Sigma^+$ channel the pure PS (when fitted to the higher energy point) underestimate the cross section for the lower data point by about a factor of 2. For the $pp \to pK^+\Lambda$ channel the underestimation in the close to threshold region is comparable when equivalently normalized. In order to compare the Σ^+ production within this framework the same analysis (fitting equation 3.3 to the data) were done for the two available data points. This attempt should not be understood as an extraction of the scattering length for the $N\Sigma^+$ system, but it should give some idea how this channel is related to the other NY systems.

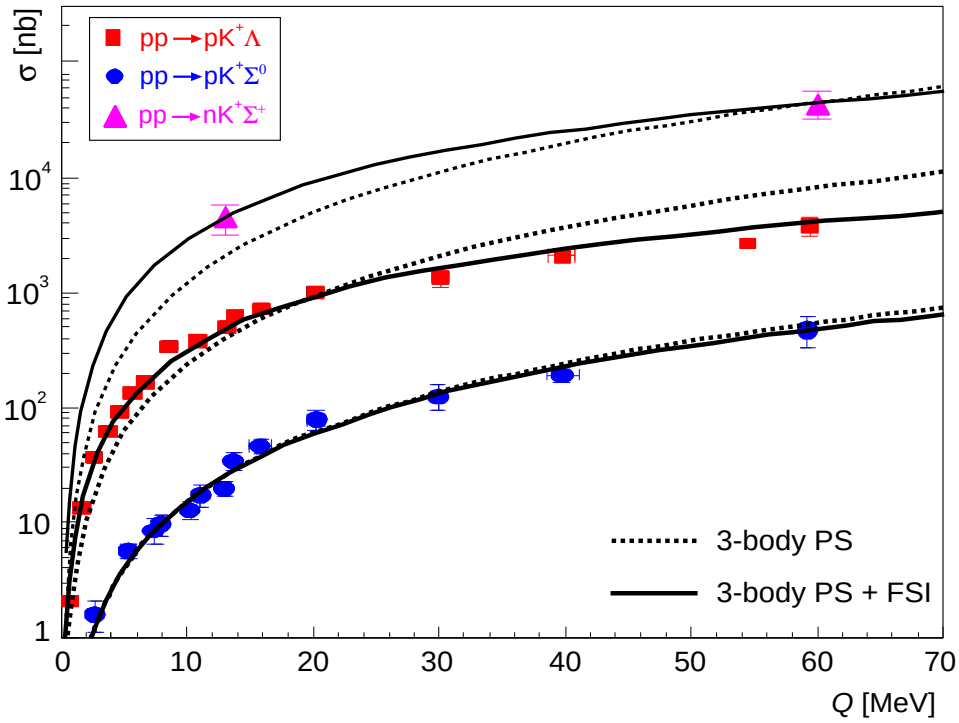

Figure 3.5: The $pp \to nK^+\Sigma^+$, $pp \to pK^+\Lambda$ and $pp \to pK^+\Sigma^0$ cross sections as a function of the excess energy Q. Experimental data were taken from Refs. [7–10] and this work. The lines show the calculations corresponding to 3-body phase space with (solid line) and without (dashed line) final state interaction.

In table 3.6 the normalization factor C and the ε parameter for three discussed hyperon production reactions are presented. For the $pp \to pK^+\Lambda$ and $pp \to pK^+\Sigma^0$ reactions these parameters are taken from ref. [9], and for the $pp \to nK^+\Sigma^+$ channel were calculated within this thesis. For the $pp \to nK^+\Sigma^+$ reaction the values of ε (C) are comparable to these of the reaction $pp \to pK^+\Lambda$, but much smaller (higher) than for $pp \to pK^+\Sigma^0$ channel. Besides questions of the general validity of this approach for such an analysis more than only two data points should be used. The discussed factors are related to the scattering parameters â and r̂ [11]. It seems that in case of the Σ^+ production via the $pp \to nK^+\Sigma^+$ reaction a rather strong $n\Sigma^+$ FSI is present, however, first the reaction mechanisms (especially the role of nuclear resonances) should be understood better.

Table 3.6: The C and ε parameters from the equation 3.3 for different hyperon production reactions obtained from the fits to the experimental data points.

Reaction channel $pp \to$	C [nb/MeV^2]	ε [MeV]	Ref.
$nK^+\Sigma^+$	178 ± 151	9 ± 14	this work
$pK^+\Lambda$	98.2 ± 3.7	$5.51^{+0.58}_{-0.52}$	[9]
$pK^+\Sigma^0$	2.97 ± 0.27	133^{+108}_{-44}	[9]

The unexpected high cross section for the Σ^+ production in comparison to the Σ^0 production can not be explained by any available model. The large ratio between Σ^+ and Σ^0 close to threshold compared to the low value at higher energies indicates that certain reaction processes may induce large cross section changes. If e.g. the Δ resonance excitation is considered (where the ρ meson exchange excites the Δ^+ resonance in the $pp \to pK^+\Sigma^0$ reaction channel, and the ρ^+ excites the Δ^{++} resonance in the $pp \to nK^+\Sigma^+$ reaction channel), then, from isospin relations the cross section for Σ^+ is expected to be about 5 times higher than for the Σ^0 production. This is already one order of magnitude higher than the *resonance model* prediction. A full understanding of various possible scenarios has to wait for further theoretical work.

3.3 Conclusions and perspectives

To determine the total cross section of the $pp \to nK^+\Sigma^+$ channel, the neutron and kaon were detected and the Σ^+ hyperon was identified via the missing mass technique.

Compared to the $pp \to pK^+Y$ studies at COSY–11 , the background level in the invariant mass distribution determined from the reconstructed momentum and the time of flight was rather high. Monte Carlo studies combined with the clearly visible pion and proton peaks allow to determine the kaon range. Nevertheless extensive checks of the kaon range in the invariant mass distribution to be selected for further analysis have been performed. The momentum reconstructed from the tracks in the drift chambers by backtracking to the target was compared with the momentum calculated from the time of flight, assuming the particle mass, resulted in a perfect agreement. As a second cross check energy loss studies in the scintillation detectors were done which were consistent with the reconstructed momentum. The momentum determination procedure for positively charged particles was also checked by a missing mass analysis of the reaction channels: $pp \to pp\pi^0$, $pp \to pp\eta$ and $pp \to pK^+\Lambda$. In these studies π^0, η and Λ peaks are clearly identified and their positions in the mass spectrum correspond to their nominal masses [2].

The momentum calculation of the neutron was based on the assumption that only neutrons give a signal in the neutron detector and all other charged particles are very efficiently discriminated by the VETO detector. Most of the γs as well as a large fraction of fast neutrons from background channels were discriminated by the *neutron time-cut*.

Having the four-momentum of the neutron, the respond of the COSY–11 neutron detector could be compared with the signal expected from MC studies. The ideal candidate for such studies is the $pp \to pn\pi^+$ channel. The neutron detector efficiency determined in MC studies is in the order of 50 % to 60 %, depending on the neutron energy range. This is in agreement with the previously measured $pp \to pn\pi^+$ channel at $P_{beam} = 802.8$ MeV/c [54].

In order to extract the number of Σ^+ events, extensive background studies were performed. Although the dominant background components were determined, the selective contribution of the single channels is uncertain. The background was determined in two different ways by a summation of the background channels from MC studies and by the structure in the missing mass distribution for the other excess energy data which should be comparable. In both methods within the error bars consistent Σ^+ event number was extracted.

The missing mass analysis shows clearly that the selection of events from the $pp \to nK^+\Sigma^+$ reaction is possible, however the Σ^+ signal is always located on top of a significant unavoidable physical background using the present COSY–11 detection system for an unambiguous identification of these events. As long as the excess energy is sufficiently high, the Σ^+ peak is located on the decrease of a smooth background distribution like in the case of $P_{beam} = 2.74$ GeV/c. Here, increasing statistics would help to improve the Σ^+ event selection. For measurements close to threshold, however, an improved selection of kaons is needful. For example a background-free identification of the $pp \to nK^+\Sigma^+$ reaction would be possible via the Σ^+ decay products. But for a reasonable measurement time a higher detection efficiency would help. This could be provided by the WASA (Wide Angle Shower Apparatus) large-acceptance detector, which is going to be installed in the COSY ring in 2006 [71].

For the total cross section calculations, the luminosity and efficiency determination is essential. In the efficiency studies realistic Monte Carlo simulations were used. The influence of higher partial waves was investigated, but for the calculations, the efficiency of the COSY–11 detection system with the assumption that only S-wave contributes to the reaction process was taken. The detection efficiency for the $pp \to nK^+\Sigma^+$ channel determined in this thesis is about a factor from 4 to 5 lower compared to the efficiency for the $pp \to pK^+\Lambda$ channel [57]. This is expected due to the fact that the COSY–11 neutron detector covers a relatively small solid angle compared to the other components of the system. The luminosity determined within this thesis and used for the total cross section calculations is very similar for both beam momenta. This was expected and verified from the on-line luminosity system running during the experiment. As a cross check of the luminosity calculations the cross section of the $pp \to pK^+\Lambda$ channel at $Q = 88.2$ MeV was determined. The resulting total cross section is in agreement with the existing data points for this channel.

The unexpectedly high cross section for the Σ^+ production via the $pp \to nK^+\Sigma^+$ reaction can not be described presently by any of two available models. In the *Jülich meson exchange model* [18, 19] on the basis of $pp \to pK^+\Lambda$ and $pp \to pK^+\Sigma^0$ data, the destructive interference between pion and kaon was considered as a mechanism leading to the large cross section ratio in the hyperon production. However, the cross section of the $pp \to nK^+\Sigma^+$ channel (obtained within this thesis) is more than one order of magnitude higher than in the discussed model predictions. Within the framework of this model such a high cross section for the Σ^+ production can not be achieved. Additional mechanisms like resonance excitations seem to play an important role. This is supported by the observed dominant resonance contribution in the $pp \to pK^+\Lambda$ experimental data obtained by the TOF collaboration [4]. In the second available model, the *resonance model* [15, 17], predictions underestimate the experimental cross section by a factor of 500 (50) for lower (higher) energy data. This model, in general, much better describes the experimental data without the neutron in the entrance or exit channel [17]. Since this model takes into account four different resonance excitations added incoherently, a coherent addition of the contributing amplitudes with suitable strengths might result in much higher cross sections.

In hyperon studies performed at the COSY–11 installation, the strong influence of FSI in the Λ production close to threshold was observed. The studies of the $pp \to nK^+\Sigma^+$

reaction channel – from which for the first time [2] two close to threshold data points are available – suggest that also in the $pp \to nK^+\Sigma^+$ channel the FSI plays a very important role. Further studies of the Σ^+ production are necessary to clarify the picture. On the experimental side additional data points with better events selectivity should be added. This could be achieved by using a 4π neutral and charged particle detection systems. On the theoretical side an improved model has to be developed which would reproduce the hyperon production cross section data close to threshold.

[2] The $pp \to nK^+\Sigma^+$ channel was investigated by TOF collaboration at excess energies Q = 96 MeV and 128.7 MeV, but their data were not yet published.

Bibliography

[1] M. Gell-Mann, Phys. Lett. **8** (1964) 214.

[2] K. Hagiwara et al., *Review of Particle Physics*, Phys. Rev. **D66** (2002) 010001.

[3] G. Rochester et al., *Nature* **160** (1947) 855.

[4] http://www.fz-juelich.de/ikp/COSY-TOF/index_e.html.

[5] W. K. Eyrich et al., Prog. Part. Nucl. Phys. **50** (2003) 547.

[6] http://ikpe1101.ikp.kfa-juelich.de/cosy-11/.

[7] J. T. Balewski et al., Phys. Lett. **B420** (1998) 211.

[8] S. Sewerin et al., Phys. Rev. Lett. **83** (1999) 682.

[9] P. Kowina et al., Eur. Phys. J. **A22** (2004) 293.

[10] R. Bilger et al., Phys. Lett. **B420** (1998) 217.

[11] G. Fäldt and C. Wilkin, Z. Phys. **A357** (1997) 241, nucl-th/9612019.

[12] A. Baldini et al., *Total Cross-Section for Reactions of High-Energy Particles*, Springer, Berlin, 1988.

[13] R. Shyam et al., Phys. Rev. **C63** (2001) 022202.

[14] R. Shyam, hep-ph/0406297 (2004).

[15] A. Sibirtsev et al. Nucl. Phys. **A646** (1999) 427.

[16] A. Sibirtsev et al. nucl-th/0004022 **v2** (2000).

[17] N. Tsushima et al., Phys. Rev. **C59** (1999) 369.

[18] A. Gasparian et al., Phys. Lett. **B480** (2000) 273.

[19] A. Gasparian et al., Nucl. Phys. **A684** (2001) 397.

[20] B. Holzenkamp et al., Nucl. Phys. **A500** (1989) 485.

[21] M. Batinić et al., Phys. Scripta **56** (1991) 24.

[22] A. Gasparyan et al., Proceedings of the *Symposium On Threshold Meson Production In pp And pd Interaction*, Kraków (2001) 205.

[23] R. Maier, Nucl. Instr. & Meth. **A390** (1997) 1.

[24] http://www.fz-juelich.de/ikp/en/.

[25] http://www.fz-juelich.de/.

[26] T. Rożek et al., COSY Proposal no. **117** (2002).

[27] S. Brauksiepe et al., Nucl. Instr. & Meth. **A376** (1996) 397.

[28] H. Dombrowski et al., Nucl. Instr. & Meth. **A386** (1997) 228.

[29] H. H. Adam, Ann. Rep. 1998, IKP FZ-Jülich, **Jül-3640**.

[30] P. Moskal hep-ph/0408162 (2004), Jagellonian University Press (2004) ISBN 83-233-1889-1.

[31] P. Moskal, *η' meson production in the $pp \to pp\eta'$ reaction near threshold*, PhD. thesis, Jagellonian University, Kraków 1998, IKP FZ-Jülich, **Jül-3685**.

[32] T. Sefzick, Ann. Rep. 2002, IKP FZ-Jülich, **Jül-4052**.

[33] M. Sokołowski et al., Proceeding on the *Mezon Production, Interaction and Decay Workshop*, Kraków, Poland, 1991.

[34] G. F. Knoll, *Radiation detection and measurement*, 3rd edition New York: John Wiley & Sons, Inc., 1999.

[35] Bicron/Saint-Gobain NICC, 3760 Soest, The Netherlands.

[36] M. Wolke, *Ein grossflächiger Szintillationsdetektor mit Matrix-Auslese für Experimente an COSY*, Diploma Thesis, Universität Münster, Germany, December 1993.

[37] T. Blaich et al., Nucl. Instr. & Meth. **A314** (1992) 136.

[38] R. Wigmans, Nucl. Instr. & Meth. **A259** (1987) 389.

[39] C. W. Fabjan, Nucl. Instr. & Meth. **A141** (1977) 61.

[40] T. Akesson, Nucl. Instr. & Meth. **A241** (1985) 17.

[41] E. Bernardi, Nucl. Instr. & Meth. **A262** (1987) 229.

[42] P. Moskal, Ann. Rep. 1996, IKP FZ-Jülich, **Jül-3365**.

[43] M. Janusz et al., Ann. Rep. 2003, IKP FZ-Jülich, **Jül-4107**.

[44] R. Czyżykiewicz, *η and η' meson production in the quasi–free proton–neutron collisions at the COSY–11 facility*, Diploma Thesis, Kraków, Poland, June 2002.

[45] T. Rożek and P. Moskal, Ann. Rep. 2002, IKP FZ-Jülich, **Jül-4052**.

[46] M. Wolke, *Schwellennahe assoziierte Strangeness-Erzeugung in der Reaktion* $pp \to ppK^+K^-$ *am Experiment COSY–11* , PhD. thesis, IKP FZ-Jülich, **Jül-3532**.

[47] E. Amarian, Nucl. Instr. & Meth. **A460** (2001) 239.

[48] http://wwwasdoc.web.cern.ch/wwwasdoc/geant_html3/geantall.html.

[49] P. A. Aarnio et al., *Fluka user's guide*, Technical Raport TIS-RP-190, CERN, 1987.

[50] A. Ferrari et al., Proceeding on the *MC93 International Conference on MC Simulation in High Energy and Nuclear Physics*, Tallahassee, Florida, 1993.

[51] N. L. Singh et al., J. Phys. G: Nucl. Part. Phys. **18** (1992) 927.

[52] P. A. Berardo et al., Phys. Rev. **D6** (1972) 756.

[53] A. S. L. Parsons et al., Nucl. Instr. & Meth. **79** (1970) 43.

[54] P. Moskal, Ann. Rep. 2001 IKP FZ-Jülich, **Jül-3978**.

[55] P. Wüstner, *Die Produktion des eta-Mesons am Jülicher Beschleuniger COSY und Entwicklung eines optimierten Datenaufnahmesystems*, PhD. thesis, Universität Bochum, 1998.

[56] J. Przerwa, *Bremsstrahlung radiation in the deutron–proton collision* ; M.Sc thesis, Jagellonian University, hep-ex/0408016.

[57] P. Kowina, *Production of the neutral* Λ *and* Σ *hyperons in proton–proton interactions at COSY-11*, PhD. thesis, University of Silesia, Katowice, Poland, 2002.

[58] P. Winter, *Schwellennahe Kaonenproduktion im Proton–Proton Stoss am Experiment COSY–11* , PhD. thesis, Universität Bonn, 2005.

[59] D. Hesselbath, *Experimentelle Untersuchungen zur Hyperon-Produktion im Proton–Proton-Stoss*, PhD. thesis, Universität Bonn, 2000.

[60] M. Fritsch, *Assoziierte Strangenessproduktion in den Reaktionen* $pp \to pK^+\Lambda$ *und* $pp \to pK^+\Sigma^0$ *am COSY Flugzeitspektrometer*, PhD. thesis, Universität Erlangen, 2002.

[61] Cosy–11 collaboration, Ann. Rep. 1997, IKP FZ-Jülich, **Jül-3365**.

[62] M. Wolke, Proceeding of the Conference *Hadrons in Dense Matter*, GSI Darmstadt (2000) 27.

[63] R.Bilger et al., Phys. Lett. **B420** (1998) 217.

[64] D. Grzonka and K. Kilian, Nucl. Phys. **A626** (1997) 41.

[65] V. Flamino et al., *Compilation of Cross Sections*, CERN-HERA 84-01 1984.

[66] D. Albers et al., Phys. Rev. Lett. **78** (1997) 1652.

[67] E. Byckling, *Particle Kinematics*, John Wiley & Sons Ltd., London 1973.

[68] E. Segrè, *Nuclei and Particles: An Introduction to Nuclear and Subnuclear Physics*, 2nd edition, New York 1977.

[69] J. Haidenbauer, IKP, FZ–Jülich, Germany, private communication (2005).

[70] A. Sibirtsev, IKP, FZ–Jülich, Germany, private communication (2005).

[71] *WASA at COSY* (COSY-PAC 29), nucl-ex/0411038.

List of Figures

List of Tables

Acknowledgements

At the end of this thesis I would like to thank many people, I had a great pleasure to work with.

First of all I would like to thank Prof. Dr. Walter Oelert, Prof. Dr. hab. Wiktor Zipper and Prof. Dr. hab. Marek Siemaszko for giving me the possibility to work in the COSY–11 collaboration at the Research Center in Jülich.

I wish to thank Prof. Dr. Walter Oelert, Dr. Dieter Grzonka, Dr. hab. Paweł Moskal, Dr. Peter Winter, Dr. Thomas Sefzick, Dr. Piotr Kowina and Dr. Magnus Wolke who were very helpful with their continuous interest, many suggestions and readiness for patiently answering all my questions. I am sure, this would be much more difficult without the introduction to the COSY–11 facility given by Prof. Dr. hab. Wiktor Zipper and Prof. Dr. hab. Marek Siemaszko. Thank you very much for that.

I want to thank Dr. Dieter Grzonka for time he spent on reading the first drafts of my dissertation as well as my supervisor Prof. Dr. hab. Marek Siemaszko, Prof. Dr. Walter Oelert and Dr. hab. Paweł Moskal for the fruitful suggestions and corrections of my thesis. I know how time consuming it is, and therefore I am grateful for that.

I owe a great appreciation for numerous friends from Katowice, Kraków, Jülich and Münster. Working with you was a pleasure for me. Especially I want to thank Rafał Czyżykiewicz, Borys Piskor–Ignatowicz and Ola Wrońska for the discussions not only about physics.

I especially owe a great debt to Dr. Peter Winter, my former neighbor with whom I had a pleasure to share the same office and with whom I played the violin in the same symphonic orchestra, but above all, an outspoken friend and a challenging partner in discussions. His inestimable help on many different plains made the daily live of my family in this foreign country so easy.

I owe profound gratitude to my family, and specifically to my parents, for giving me the opportunity of education and for teaching me perseverance and curiosity of the world around me.

And last but not least, I want to express my appreciation to my wife, Ania. Without your love, patience and the warm home that you created in our tiny apartment this thesis would have never come to be.

Tomek Rożek

Forschungszentrum Jülich
in der Helmholtz-Gemeinschaft

Jül-4184
Oktober 2005
ISSN 0944-2952